ISSN 1063-7796, Physics of Particles and Nuclei, 2015, Vol. 46, No. 4, pp. 678–728. © Pleiades Publishing, Ltd., 2015.
Original Russian Text © Yu.N. Kharzheev, 2015, published in Fizika Elementarnykh Chastits i Atomnogo Yadra, 2015, Vol. 46, No. 4.

Scintillation Counters in Modern High-Energy Physics Experiments (Review)

Yu. N. Kharzheev

Joint Institute for Nuclear Research, Dubna, Russia

e-mail: kharzheev@mail.ru

Abstract—Scintillation counters (SCs) based on organic plastic scintillators (OPSs) are widely used in modern high-energy physics (HEP) experiments. A comprehensive review is given to technologies for production of OPS strips and tiles (extrusion, injection molding, etc.), optical and physical characteristics of OPSs, and methods of light collection based on the use of wavelength-shifting (WLS) fibers coupled to multipixel vacuum and silicon PMs. Examples are given of the use of SCs in modern experiments involved in the search for quarks and new particles, including the Higgs boson (D0, CDF, ATLAS, CMS), new states of matter (ALICE), CP violation (LHCb, KLOE), neutrino oscillations (MINOS, OPERA), and cosmic particles in a wide mass and energy interval (AMS-02). Scintillation counters hold great promise for future HEP experiments (at the ILC, NICA, FAIR) due to properties of a high segmentation, WLS fiber light collection, and multipixel silicon PMT readout.

DOI: 10.1134/S1063779615040048

CONTENTS

INTRODUCTION

Plastic scintillation counters are basic detectors of particles. It is difficult to imagine an elementary particle or nuclear physics experiment without the use of scintillation counters. New accelerators with their increasing energy and luminosity require detectors with better resolution in energy, space, and time, and which are more reliable, easy to use, compact, inexpensive, easy to manufacture, while allowing high segmentation and featuring long-term stability of characteristics and radiation hardness.

Scintillation counters meet these requirements to a great extent. A well-developed modern technology allows most needed long scintillator strips and tiles of different shape to be produced in large amounts and at relatively low cost. Strips are produced by extrusion, and tiles are predominantly produced by injection molding. During extrusion, a reflective TiO_2 coating is applied to a strip and a co-extruded hole in strip or a groove on one of its wide side are made. In tiles the groove is made when they are finished.

Signals from strips and tiles are read out by a photodetector (PD) through wavelength-shifting (WLS) fibers inserted into the grooves or holes and connected to the PD directly or through an optically clear fiber. This fiber readout system is compact and efficient because it collects more light than a system with traditional fish tail light guides. It also allows multianode vacuum PMTs or multipixel silicon PMTs to be used as PDs. With the latter PMTs, signals from each strip (tile) can be fed through fibers to individual pixels, which considerably decreases the number, size, and eventually cost of PDs. In addition, if necessary, the fiber system easily allows the PDs to be placed beyond the magnetic field.

Operation of a scintillation counter is based on emission of light as an ionizing particle passes through the luminescent material of the counter, which is then collected, converted, and guided to the PD. The most important characteristics of a scintillation counter are light yield, light collection, time resolution, attenuation length, stability of characteristics, radiation hardness, ability to adapt the emitted light to the spectral sensitivity of the PD, and transmission of light to the PD.

Scintillation counters are reliable and efficient instruments used in many experiments [1, 2], making them deserving of their status among detectors. They are simple to operate, can be easily calibrated and monitored using LEDs and radioactive sources, take little space in modern spectrometric facilities, and meet to a large extent the requirements on stability of characteristics and radiation hardness. They are multifunctional. Calorimeters, triggers, tracking, time-of-flight, and veto systems are only few of their fields of application.

In the first section, various uses of scintillation counters are comprehensively considered, the main properties of inorganic and organic scintillators are given, technology for production of organic plastic scintillators (OPSs) by a number of the best known manufacturers (ISMA, Kharkov, Ukraine; IHEP, Protvino, Russia; FNAL/NIICAD, Chicago, United States) is described, and the most important OPS characteristics are considered. Much attention is given to light collection using WLS fibers and fiber-coupled PDs (multianode vacuum PMTs and semiconductor silicon PMTs).

The second section deals with examples of using scintillation counters in large modern detectors intended for investigations in various fields of elementary particle physics like the search for quarks and new particles, including the Higgs boson (D0, CDF, ATLAS, CMS), superdense states of matter (ALICE), CP violation (LHCb, KOPIO, KLOE), neutrino oscillations (MINOS, OPERA), and cosmic particles in a wide mass and energy interval, including antimatter particles (AMS-02).

Prospects for the use of particle detectors in current and future high-energy physics (HEP) experiments are closely related to development of PDs. Some of the trends in the development of the particle identification methods and the role of PDs were examined in [3]. Scintillation counters are best coupled with PDs of multipixel structure like multianode vacuum PNTs, semiconductor silicon avalanche photodiodes (APDs), and limited Geiger mode avalanche photodiodes (G-APDs), whose status and prospects for the development and use are considered in the third section.

The following abbreviations are most often used in the text.

PS and PVT: polystyrene ($(C_8H_8)_n$) and polyvinyl toluene ($(C_9H_{19})_n$), the most commonly used base materials.

FD: fluorescent dopant, PPO (2,5-diphenyloxazole, $C_{15}H_{11}NO$), PTP (para-terphenyl, $C_{18}H_{14}$), and POPOP (1,4-di-(5-phenyl-2-oxazolyl)-benzene, $C_{24}H_{16}N_2O$).

HF (hydroxyflavone), Y11, Y(8), K27: wavelength shifters.

WLS fiber: wavelength-shifting fiber.

S type/non-S type WLS fibers: fibers with oriented/uniformly distributed molecules.

APD: avalanche photodiode.

HAPD: hybrid avalanche photodiode.

G-APD: limited Geiger mode avalanche photodiode.

SCINTILLATORS AND THEIR PROPERTIES

Main Properties of Scintillators

There is a great variety of organic and inorganic scintillators with their own advantages and disadvantages. The choice is dictated first of all by the goals set to be achieved in the experiment and by the properties of the scintillator. Scintillators mainly differ by the light yield and decay time. Inorganic scintillators feature high light yield and long decay time, and organic scintillators feature low light yield and short time. The main properties and uses of scintillators are reviewed in many publications [1, 2].

Inorganic scintillators. The most commonly used inorganic scintillators are NaI(Ti), CsI(Tl), BaF_2, BGO, $PbWO_4$, and LSO:Ce.

Sodium iodide NaI(Tl) has the highest light yield (40000 photons per 1 MeV of energy loss), but it is very hygroscopic (an air-tight enclosure is needed) and requires careful handling. The spectral composition of its light with a maximum at 415 nm well agrees with the spectral sensitivity of bialkaline PMTs.

Cesium iodide CsI(Tl) has high light yield, is easy to process, and is not hygroscopic. Its radiation spectrum with a maximum at 550 nm well agrees with the spectral sensitivity of silicon photodiodes.

Barium fluoride BaF_2 is the fastest among inorganic scintillators and has two time components, one with a decay time of 0.9 ns and the other with a decay time of about 630 ns. The fast time component is excited by gamma rays and the slow one by alpha particles, which generally allows identification of these particles by the decay time of the PD signal. The BaF_2 radiation spectrum is characterized by two maxima, one in the ultraviolet region at about 200 nm and the other at about 320 nm.

Bismuth germanate BGO has high density and accordingly a small radiation length $X_0 = 1.12$ cm; it is not hygroscopic and is easy to process. Its radiation spectrum with a maximum at 480 nm corresponds to the sensitivity spectrum of photodiodes. It is highly transparent: the attenuation length is as large as 3.5 to

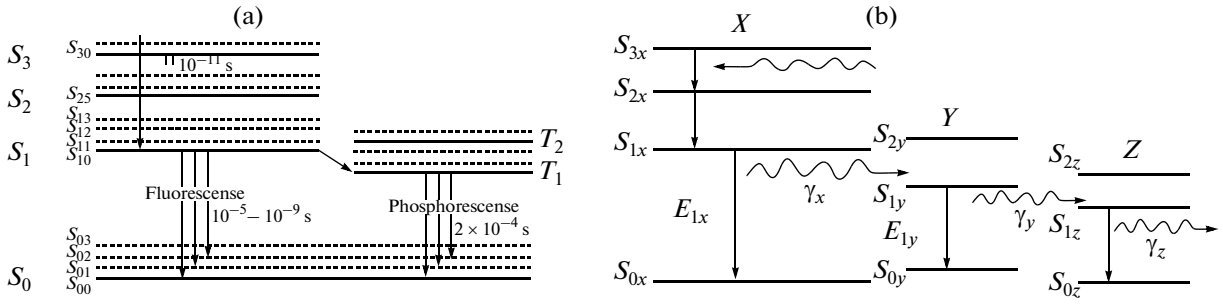

Fig. 1. Schematic view of the photon emission mechanism in a one-component (a) and a three-component (b) OS [4].

4 m. The decay time is 300 ns, but it strongly depends on temperature.

Lead tungstate $PbWO_4$ has the highest density, a very short radiation length $X_0 = 0.89$ cm, and very short decay time of 5 to 15 ns.

Lutetium silicate LCO:Ce has high density, high light yield, and short decay time.

High light yield is a feature of NaI(Tl), CsI(Tl), and LSO:Ce, the shortest decay time is typical of BaF_2 and $PbWO_4$, and high density and accordingly a small radiation length are characteristic of $PbWO_4$, LSO:Ce, and BGO. Light yield of a majority of inorganic scintillators strongly depends on temperature.

Organic scintillators (OSs). The OSs widely used in particle physics and nuclear physics experiments are mostly plastic and to a lesser extent liquid and crystalline.

Organic plastic scintillators (OPSs) have a relatively high light yield and short decay time (2 to 4 ns) and are easy to manufacture and reliable, but their obvious advantage is that they can come in almost any shape. The most common OPS bases are aromatic hydrocarbon compounds, such as polystyrene and polyvinyl toluene. However, these bases themselves have insignificant light yield and low transparency to their own radiation. To obtain a scintillation detector on their basis, it is necessary to absorb the primary radiation, which is in the ultraviolet region, and re-emit it into the region of wavelengths compatible with the spectral sensitivity region of the PD. Organic scintillators are usually two-component or three-component mixtures of a base (polystyrene, polyvinyl toluene), an FD (p-terphenyl, PPO), and a wavelength shifter (POPOP).

Apart from aromatic hydrocarbons, another commonly used base material is polymethyl methacrylate (PMMA), which has higher transparency for ultraviolet and visible light as compared with other bases.

Passing through the base, an ionizing particle loses some energy to ionization and excitation of the base molecules. This excitation is transferred rapidly to the FD molecules by nonradiative Forster dipole–dipole interactions. Molecules of the base return to the ground state, and excited molecules of the FD emit photons in the wavelength region of about 370 nm, which falls within the absorption spectrum of the wavelength shifters (fluorescence). The latter re-emit photons into the region corresponding to the photodetector sensitivity with a maximum at about 470 nm.

Excitation of molecules is sometimes accompanied by production of a metastable state with a lifetime much longer than that of an ordinary excited state. Transition from the metastable to the ground state can proceed stepwise via a transition to the allowed excited state due to the additionally acquired energy, followed by a transition to the ground state accompanied by emission of light with a time delay as long as a few milliseconds (phosphorescence).

Figures 1a and 1b show schemes of photon production due to excitation of molecules in a one-component and a three-component OS [4].

Crystalline organic scintillators. Some of the organic scintillators (anthracene, stilbene, naphthalene) are pure crystals. Among all organic scintillators, anthracene features the highest light yield with about 40000 photons per 1 MeV of energy lost by a minimum ionizing particle. However, crystalline organic scintillators are not commonly used because of difficulties in processing and producing large-sized samples. Anthracene is most often used as a reference: the light yield of any other crystal is given in percent of the anthracene light yield.

Liquid organic scintillators (LOSs). The most often used components of LOSs are solvents toluene, xylene, and benzene, FDs p-terphenyl ($C_{18}H_{14}$), PBD ($C_{20}H_{14}N_2O$), butyl PBD ($C_{24}H_{22}N_2O$), and PPO ($C_{15}H_{11}NO$), and the wavelength shifter POPOP ($C_{24}H_{16}N_2O$).

Liquid organic scintillators have a short decay time (1 to 10 ns) and theoretically allow detectors of any volume to be made. It is easy to introduce wavelength shifters in a LOS, and addition of ^{10}B increases thermal neutron detection efficiency. During operation, LOSs require protection against O_2 (air).

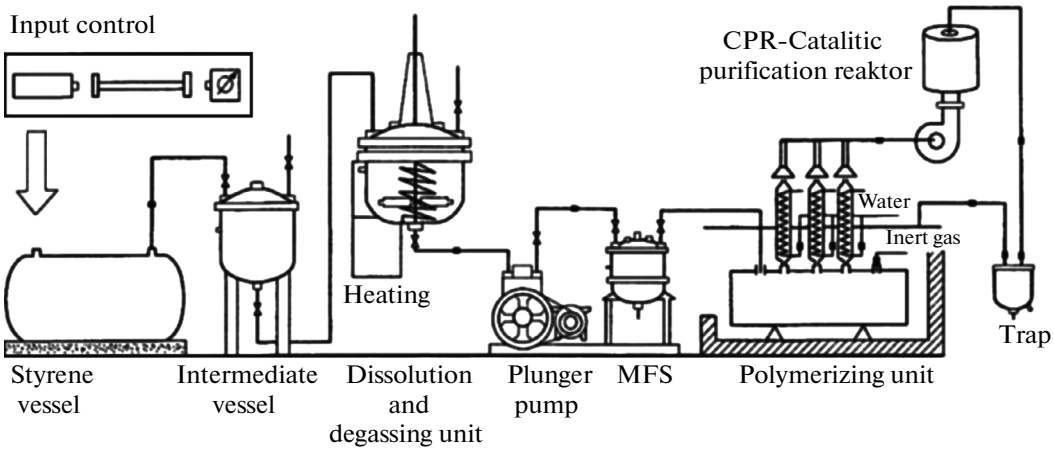

Fig. 2. Schematic view of the bulk polymerization plant at ISMA [5].

Manufacture of Organic Plastic Scintillators

Scintillators used in particle physics and nuclear physics experiments are manufactured in many places. The largest manufacturers are ISMA (Kharkov, Ukraine), FNAL/NICADD (United States), Bicron/Saint-Gobain (United States), Kuraray (Japan), IHEP (Protvino, Russia), Uniplast (Vladimir, Russia), Pol.Hi.Tech (Italy), and Chemo Technique (France).

The OPS production technology is quite well developed and based on polymerization of initial materials with subsequent bulk polymerization or injection molding or extrusion. Production of scintillators with high transparency and uniform FD distribution over the entire volume requires fulfillment of several production process conditions:

—Performing deep purification and thorough mixing of the initial materials.

—Maintaining the necessary temperature regime.

—Bubbling styrene with inert gas (argon) to avoid access of oxygen to the reaction mixture.

—Performing evacuation and microfiltration.

—Annealing the item to remove remaining monomer and relieve residual stresses.

Plastic scintillators are manufactured using commercially available pellets of base materials (styrene, vinyl toluene), FDs (p-terphenyl, PPO), and wavelength shifters (POPOP). Quantitative proportions of these components are based on the required characteristics of the scintillator, and for FDs and wavelength shifters they vary within 1–3% and 0.01–0.044% by weight of the base.

Bulk polymerization method. It is a traditional method widely used in both large and small laboratories for producing and machining scintillators of various shapes and sizes. The production process conditions discussed above should be strictly fulfilled for the method in question. Particular attention should also be given to heat removal to avoid local overheating during polymerization. The thus made scintillators have the highest transparency and uniformity and a higher light yield in comparison with scintillators manufactured by other methods.

ISMA in close cooperation with DLNP (JINR) produced a large number of tiles for HEP experiments with polystyrene as a base, 2% p-terphenyl, and 0.03% POPOP—a scintillator known as UPS-923A [5]. Later the UPS-923A production process was modified by decreasing the percentage of p-terphenyl to 1.5% and POPOP to 0.02% and changing the surface machining process. Instead of grinding and mechanical polishing, the surface of the tiles was machined using diamond turning with subsequent nonabrasive turning. As a result, the surface reached the quality of thermally processed glass, and the transparency of the scintillator was considerably improved. This scintillator was branded UPS-923D [5]. About 600 rectangular ($180 \times 17 \times 2$ cm^3, $300 \times 30 \times 2$ cm^3) and trapezoidal ($180 \times 40(30) \times 1.5$ cm^3) UPS-923A scintillation counters were made for various CDF-II muon subsystems and 2800 UPS-923D scintillation counters $125 \times 125 \times 20$ mm^3 in size for the CDF-II preshower system. Figure 2 shows the schematic view of the ISMA block polymerization plant [5].

Injection molding (IHEP/JINR LHEP). The dry mixture of commercial polystyrene pellets, PPO (1.5%), and POPOP (0.05%) is loaded into the automatic thermoplastic machine where the melt temperature 170–210°C and pressure about 150 kg/cm^2 are maintained [7]. A large number of $142 \times 146 \times 5$ mm^3 tiles for the hadronic calorimeter of the Tagged Neutrinos Facility [8] were produced by this method.

This method is highly productive: during mass production it takes about 2 min to make a tile. About 460000 trapezoid polystyrene tiles of 11 various sizes with a thickness of 3 mm for the Hadron Tile Calorimeter of the ATLAS spectrometer [9] and a large number of tiles for the LHCb calorimeters were made at

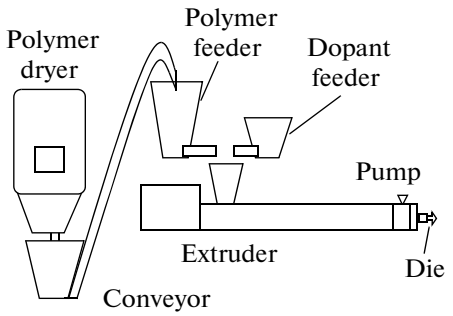

Fig. 3. Schematic diagram of the FermiLab/NICADD extrusion line [12].

IHEP (Protvino, Russia). A mixture of polystyrene with added p-terphenyl (1.5%) and POPOP (0.044%), predried at 60–70°C and melted, was injected in a special mold at 170–190°C at high pressure. It was important to maintain the temperature at a level of not higher than 190°C because at higher temperatures the fluorescent dopants could be destroyed.

The base was pellets of polystyrene PSM-115 (AKRO, Kazakhstan) and BASF-165H. In PSM-115 the monomer admixture was 0.1% and water admixture was below 0.1%. The prescribed geometrical parameters of the calorimeter set rigorous precision requirements on the scintillator tile size and consequently on the molds (<0.1 mm). Even more rigorous requirements were imposed on the smoothness and planarity of tile surfaces (better than 20 μm) because this directly affected the quality of the tile surface and ultimately the light yield and the attenuation length.

The scintillator tiles produced by this method were cheaper than those made by other methods, but their light yield turned out to be 20% lower than the light yield of the tiles produced by the bulk polymerization method. Nevertheless, the result satisfied the requirements of the Tile Calorimeter.

Molding method. Polystyrene pellets with FDs are melted and polymerized in light metal molds with mirror-polished walls and an open upper surface. This method is used to produce scintillators of various sizes that do not need machining (polishing) [9, 10]. Scintillators produced by this method at IHEP were used in the COMPASS experiments at CERN, KOPIO and PHENIX experiments at Brookhaven, and ISKRA and OKA experiments at IHEP.

Scintillators with remarkably reflective surfaces with roughness no higher than 0.001 μm were produced using the "glass" technique. Styrene was subjected to an ordinary purification process in the inert gas, and fluorescent dopants were dissolved in it. The resulting solution was filtered in the microfiltration setup to remove unsolved styrene and dopants from the melt, and polymerization was carried out in a special mold [6] that consisted of two plane-parallel polished silicate glasses mounted in a stainless steel frame with gaskets. Before filling, the surfaces of the glasses were thermally treated to reduce adhesion of the polymer to the glass. After the polymerization is completed, annealing is performed to relieve residual stresses.

Extrusion method. The method of producing scintillator strips (SSs) by extruding polymerized bulk scintillator through special dies were first used on large scale at Fermilab [11] and later found wide application in high-energy physics experiments, especially neutrino experiments, due to the following factors:

—A well-developed production process of this method allows SSs to be produced in large amounts (hundreds of tons) at a relatively low cost of $5 to $8 per kg as compared with $40 per kg in the bulk production process [11].

—It is possible to produce SSs as long as 10 m and even longer, varying in shape and cross section (rectangular, triangular).

—Simultaneously with extrusion of SSs, their surfaces are coated with a reflective TiO_2 film (except the groove area), and a hole in strip or a groove is made in one of their wide surfaces for setting the WLS fiber.

Extrusion of SSs at Fermilab. Scintillator strips for the MINOS, D0, STAR, T2K, and K2K experiments were produced at Fermilab's Scintillation Detector Development Technical Center [12]. Initially it was a two-step process: at the first step polystyrene pellets dried in a nitrogen medium to remove oxygen were mixed with FDs (1% PPO and 0.03% POPOP), and at the second step extrusion was performed simultaneously with injecting a mixture of polystyrene pellets and TiO_2 (about 15% by weight of in mixture) for applying a reflective coating. For MINOS, about 100000 strips with a rectangular cross section of 10 mm by 14 mm, a length of up to 8 m, and a groove for the WLS fiber in the wide side were produced.

For MINERvA [14], SSs were produced using the extrusion line recently installed at Fermilab in collaboration with NICADD (Northern Illinois Center for Accelerator and Detector Development) (Fig. 3) [12]. The strips had a triangular cross section and a hole with a diameter of 1.2 mm for the WLS fiber. Extrusion was performed as a single process without the first step, and the initial materials (polystyrene pellets, 1% PPO, 0.03% POPOP) were mixed, melted, and injected directly into the extruder. Before the extrusion, the initial materials underwent nitrogen purification and drying to avoid oxygen in the melting process because it considerably deteriorates transparency of SSs.

The extrusion technique was used to produce very thin TiO_2-coated strips of polystyrene with 1% PPO and 0.1% POPOP with a 3 mm by 10 mm cross section and a 1-mm hole for the WLS fiber [15].

The most expensive scintillator component is the FD. The price of the traditionally used PPO and POPOP is as high as $190–245/kg while the price of polystyrene is $1.2–1.65/kg [11]. The upper limit of

the price depends on the quality of the material and the volume of the order.

Screwless SS extrusion at ISMA [16]. The initial materials are commercially available polystyrene pellets and FDs. After thorough purification of the base material in the inert gas, removal of oxygen from it, and dissolution of the FDs in it, the polystyrene melt is bulk polymerized and extruded without using a screw. The melt is forced through the die by the excess pressure of the inert gas. This screwless extrusion technique was developed at ISMA. Not only was the extrusion process simplified, but transparency and light yield of SSs was also increased by a factor of almost 1.5 in comparison with SSs produced by extrusion using a screw. Over 3000 SSs with a rectangular cross section of 10 mm by 26 mm, a length of 7 m, reflective coating, and a groove for the WLS fiber were made for the OPERA detector [17].

Light Yield of Scintillators and Long-Term Stability of Their Characteristics

The most important characteristics of a scintillator are light yield, transparency, radiation spectrum, decay time, stability of characteristics, and radiation hardness. Only a small fraction (about 4%) of energy lost by a charged particle in the scintillator is transformed to light energy.

The light yield of a scintillator depends on many factors, such as materials (base, dopant, wavelength shifter), production technology, relationship of the emission and absorption spectra of the base, dopant, and wavelength shifter, and the sort of particles that cause scintillation. A number of photons are lost due to escape through the scintillator surface, and this number depends on the surface machining quality. A noticeable number of produced photons propagating along the scintillator are lost due to absorption on the organic and other impurities. Commercial-grade styrene contains up to 0.05–0.2% by mass of organic impurities, 0.06% by mass of water, and 0.01–0.0001% by mass of iron ions [6]. Photons are also lost due to scattering by these impurities, structural defects, and cavities in the polymer.

The scattering process is usually described by the formula

$$R = Ax\lambda^{-4} + B,$$

where λ is the photon wavelength, the first term arises from the Rayleigh scattering by inhomogeneity $<\lambda/20$ in size, and the second term arises from the scattering by inhomogeneity $>\lambda$ in size (Mie scattering). The initial purification of materials and high-level polystyrene production technology allow the Mie scattering to be avoided. Transparency and light yield of polystyrene can be increased by deep microfiltration, when polystyrene initially purified by aluminum oxide is vacuum distilled using track membranes. These microfiltration membranes with 10^6 to 10^9 identical pores per cm^{-2} produced at JINR (Dubna, Russia) allow the initial material to be purified of impurities of 150 to 200 nm in size. With deep microfiltration, polystyrene transparency can be increased to 2.5 m. Photon loss to scattering by structural defects and cavities in the matrix structure can be considerably decreased by optimizing the annealing process through varying the temperature, duration, and rate of annealing [18].

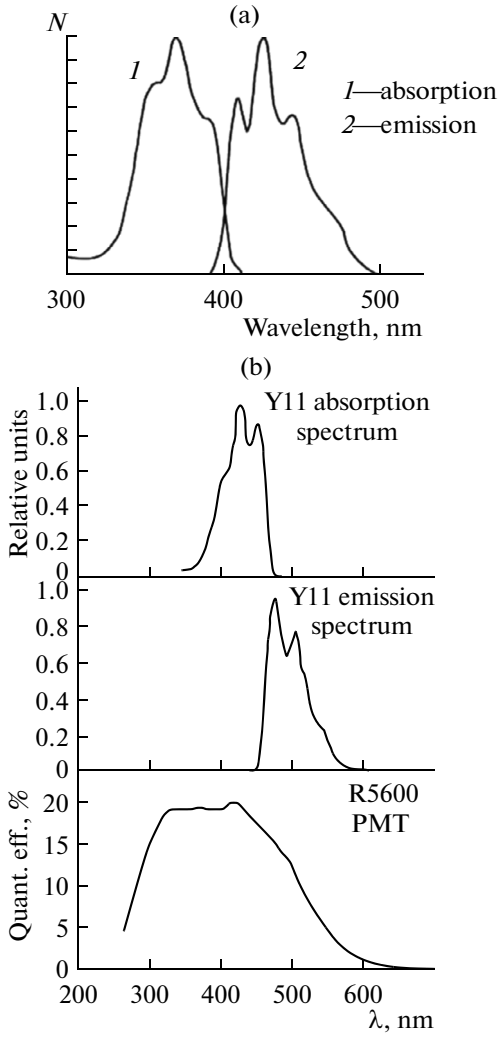

Fig. 4. Absorption and emission spectra of POPOP (a) and Y11 (b) and spectral sensitivity of the R5600 PMT (Fig. 4b, bottom).

The choice of FDs and wavelength shifters is largely dictated by their emission and absorption spectra. FD absorption spectra should be close to the base emission spectrum. The maxima of the wavelength shifter absorption and emission spectra should be as far away from one another (Stokes shift) as possible to avoid self-absorption of emitted photons (Figs. 4a, 4b). The commonly used wavelength shifters are Y11, POPOP, and 3HF (3-hydroxyflavone) with the Stokes shifts as large as 190 nm for 3HF [19] and 60 nm for POPOP (Fig. 4a) [20] and Y11 (Fig. 4b).

Table 1. Factor kB × 10^2, g/cm^2 MeV^{-1} for some of organic scintillators [1]

Type	NE102	NE213	PilotB	Stilbene	Anthracene	NE230	SCSN38
kB	1.31	1.26	1.59	0.86	1.46	1.10	0.86

Dependence of the scintillator light yield on the nature of the ionizing particle is determined by the fact that strongly ionizing particles produce local electric fields along the track, which leads to quenching of scintillations, i.e., to an increasing number of nonradiative transitions in excited molecules and, accordingly, to a decrease in the light yield dN/dx. For example, light yields from protons and α particles are respectively about 1/2 and 1/10 of the light yield generated by electrons. This fact is used to separate particles on the basis of the emission spectrum shape.

A decrease in the light yield as a function of the scintillator material is described by the Birks formula [1]

$$dN/dx = A(dE/dx)/[1 + kB(dE/dx)],$$

where dE/dx is the energy loss per unit path, A is a constant, and kB is the Birks factor.

Table 1 lists values of the kB factor for a number of organic scintillators.

The most commonly used scintillator based materials are polystyrene (PS) and polyvinyl toluene (PVT). The quantitative characteristic of the scintillator light yield and transparency are the technical attenuation length (TAL) and the bulk attenuation length (BAL).

The TAL of a scintillator tile is defined as a length over which the light yield decreases by the factor e, and it depends on the transparency and geometrical parameters of the tile (thickness and shape) and also on the surface machining quality. The BAL depends on the scintillator material and production technology and is defined as a length over which the intensity of the initial light decreases by the factor e. The TAL of a tile is determined by measuring its light yield from cosmic muons (or e from a radioactive source) at different distances from the PD, and the BAL is found by measuring the tile transmission for the monochromatic light whose wavelength is close to the scintillator emission wavelength (e.g., by a cadmium laser) [21].

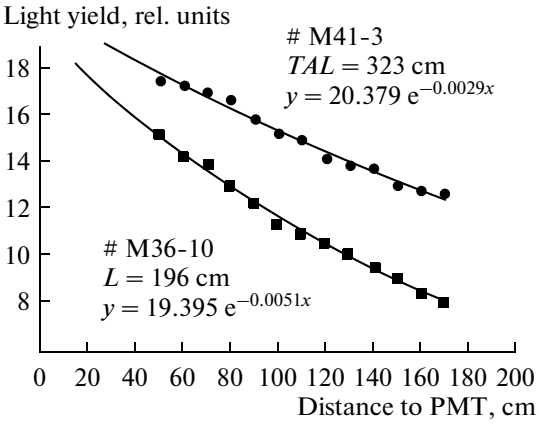

Fig. 5. Dependence of the light yield on the distance to the PMT for the UPS-923D (upper curve) and UPS-923A (lower curve) tiles 2 × 45 × 180 cm in size.

Light yield of scintillation counters is usually expressed in a number of photoelectrons, which is found using the spectrometric channel calibration procedure based on weak-intensity LED measurements [22]. This calibration is necessary for monitoring the operation of the counters and is performed before and after using the counters. Dependence of the light yield of the scintillator on its production technology and the number of FDs was investigated with cosmic rays incident on UPS-923D and UPS-923A tiles 2 × 45 × 180 cm in size (Fig. 5). The mean TAL of the UPS-923D and UPS-923A scintillators proved to be 323 cm and 196 cm, respectively, and the light yield from UPS-923D was about 1.7 times higher than from UPS-923A. Note that the UPS-923D scintillators were manufactured with fewer FDs than UPS-923A, and the surface machining procedures were also different [6].

Figure 6 shows the results of measuring the light yield of the UPS-923A and NE-114 scintillators (the latter is equivalent in characteristics to BC-416) [22]. The measurements were performed with cosmic muons incident on NE-114 tiles 2 × 30 × 200 cm^3 in size and two UPS-923A tiles 2 × 30 × 200 cm^3 and 2 × 30 × 300 cm^3 in size. One end of the 2-m tiles was blackened and the other was connected to the PD through a fish tail light guide. Their attenuation lengths turned out to be approximately identical, 115 cm in NE-114 and 130 cm in UPS-923A. The light yield from UPS-923A was about 25% higher than from NE-114, which was because UPS-923A scintillators were manufactured with an emphasis on achieving the optimum structure of the polymer and FDs during polymerization. The 3-m UPS-923A tile, in which the reflected light from its far end was used, showed more than 40 photoelectrons over the length of 3 m.

Long-term stability of scintillator characteristics. An important feature of a scintillator is stability of its characteristics, which is especially significant because scintillation counters are widely used in collider experiments, being exposed to high radiation doses for a long time.

The scintillator gradually loses its properties due to natural aging and exposure to various adverse factors, such as temperature, humidity, and radiation. The polymeric base of the scintillator suffers degradation of its chemical and physical structures, stresses, and thermal oxidation caused by atmospheric oxygen, which is manifested by formation of microcracks and micropores on the surface and in the bulk of the scintillator and by a change in its color. The aging process also depends on the scintillator material and production technique.

In polystyrene-based scintillators the matrix begins manifesting structural changes at $T > 50°C$. Scintillators produced by the injection molding technique are more thermally stable than scintillators produced by the bulk polymerization technique. Investigations of long-term stability under natural storage conditions were carried out for the Kuraray SCSN-81, Bicron BC-408, and ISMA UPS-98RH and UPS-923A scintillators. The samples used in the measurements were $4 \times 125 \times 125$ mm tiles and $4 \times 20 \times 200$ mm strips. The results are presented in Table 2 [6], where columns 2 and 3 show the time in years, within which the light yield and the mechanical strength of the samples decreased by 20%.

As is seen from the Table, UPS-923A loses 20% of light yield for 10 years and 50% of mechanical strength for 8.2 years, i.e., it, like SCSN-81, shows the best long-term stability of the light yield and mechanical strength.

Aging of UPS-923A and NE-114 was investigated in [23]. In four years of natural aging the light yield decreased by 30% in UPS-923A and by 70% in NE-114.

Another factor affecting the long-term stability of the scintillator characteristics is humidity. The surface of the scintillators, especially those produced by the bulk polymerization with subsequent machining, can have microcracks, which will expand in the course of time under the effect of O_2 and water vapor.

An important characteristic for the scintillators used in high-energy experiments is their radiation hardness. The State Scientific Institution "Institute for Single Crystals" (Kharkov, Ukraine) developed a radiation-hard scintillator UPS-98RH based on polystyrene with plasticizer that serves to intensify diffusion of O_2 and radiolysis products in the polymeric matrix and shows the highest radiation hardness in comparison with other radiation-hard scintillators like SCSN-81T (Kuraray, Japan), BC-408 (Bicron, United States), and UPS-09RH and UPS-923A (Amcrys-H, Ukraine) [24].

Samples of these scintillators in the form of $9 \times 20 \times 200$ mm strips with surfaces polished to optical purity and $4 \times 125 \times 125$ mm tiles with a groove holding a WLS fiber were exposed to a dose of 3 and 10 Mrad from the Co^{60} source at a dose rate of 0.02 Mrad/h. The strips were used to measure BALs and TALs as a function of the exposure time, and the tiles were used to measure light yield. During the measurements the strip end farthest from the PD was blackened and the WLS fibers were not mirrored. Immediately after the exposure to the dose of 10 Mrad all samples except UPS-98RH grew strongly colored yellow and their subsurface area was bleached. Their BALs decreased to 1–2 cm while the BAL of UPS-98RH was 17 cm (Fig. 7). The TALs showed a similar behavior. At a dose of 10 Mrad the TAL of UPS-98RH was larger than the TALs of SCSN-81 and BC-408 by a factor of 1.5 and 3.0 respectively (Fig. 8).

Table 2. Long-term stability of light yield and mechanical strength

Scintillator	τ_{20} (20% of light yield)	τ_{20} (50% σ_p)
SCSN-81	10	6.2
BC-408	6	5.1
UPS-98RH	8	5.8
UPS-923A	10	8.2

The light yield from the tile light guide assembly at a dose of 10 Mrad decreased by a factor of almost 8. However, in UPS-98RH it was 40% higher than in BC-408. In addition, radiation hardness of this scintillator turned out to be independent of the exposure dose rate. For these advantages, the UPS-98RH scintillator was chosen for use as the active absorber of the forward hadronic calorimeter in the highest radiation

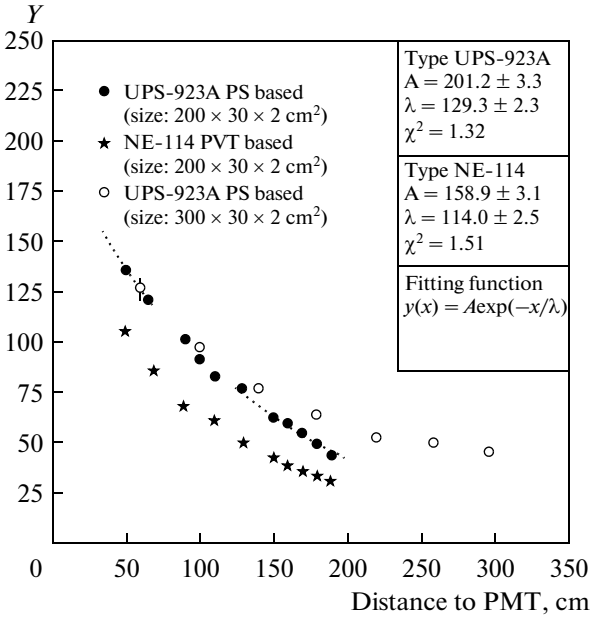

Fig. 6. Dependence of the light yield (Y) on the distance to the PMT for three tiles, two of which are produced from UPS-923A ($2 \times 30 \times 200$ cm and $2 \times 30 \times 300$ cm) and one from NE-114 ($2 \times 30 \times 200$ cm).

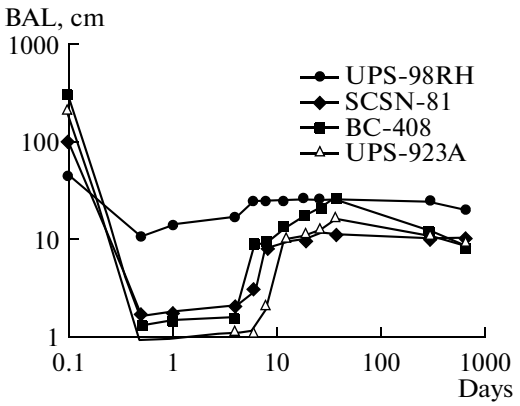

Fig. 7. Dependence of the BAL on the annealing time after exposure to a dose of 10 Mrad at a dose rate of 0.02 Mrad/h.

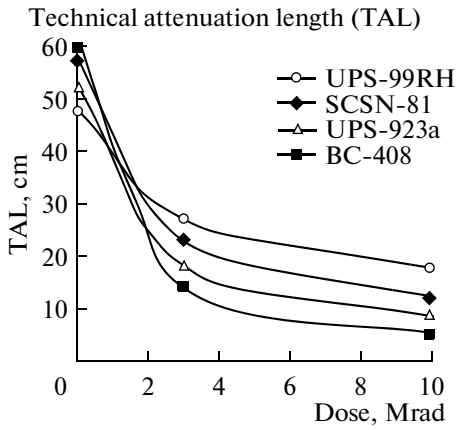

Fig. 8. Dependence of the TAL on the irradiation dose at a dose rate of 0.02 Mrad/h.

area of the CMS. The total dose in this area for 10 years of operation was estimated at about 10 Mrad.

To choose scintillators for the CDF electromagnetic calorimeter, the light yields and attenuation lengths were investigated in the SCSN-81, SCSN-38D, and BC-408 scintillators exposed to a dose of 0.5 and 1.0 Mrad from the Co^{60} source (the expected irradiation dose of the calorimeter for 10 years of operation is 0.5 Mrad). According to the requirements of the CDF experiment, the 10-year decrease in the light yield and attenuation length should not be larger than 15% and 30%, respectively. The results of the investigations presented in Tables 3 and 4 show that the scintillator meeting both requirements of the experiment is SCSN-38 [25].

Light Collection, Strips, Tiles, and Reflective Materials

Scintillator strips (SSs). Many high-energy experiments need scintillation counters capable of covering vast experimental areas (tens of thousands of square meters), with high segmentation and a great number of photodetectors. In this connection, the cost of the scintillators and PDs becomes as important as their quality. The quality of a scintillation counter depends not only on its light yield but also on the efficiency of the light collection system and on the characteristics of the PDs. A decisive contribution to the solution of this quality problem came from the extrusion and injection molding techniques, which allowed production of scintillator strips of various shapes and cross sections and scintillator tiles with thicknesses of a few millimeters to a few centimeters and areas up to a few thousands of square meters. Light from strips and tiles is collected using WLS fibers, which are inserted into grooves and holes made in strips and tiles specially for them and which guide the collected light to the multichannel PDs.

Table 3. Light yield of the tile–fiber system as a function of the exposure dose

PS sample	Light yield, p.e./MIP	Relative decrease in light yield, %	
	before exposure	after dose of 0.5 Mrad	after dose of 1.0 Mrad
SCSN-81	9.14 ± 0.14	2.2 ±0.1	8.0 ± 0.2
SCSN-38	10.46 ± 0.14	5.6 ± 0.1	13.6 ± 0.3
BC-408	8.95 ± 0.13	8.1 ± 0.2	14.6 ± 0.4

Scintillator strips were first manufactured in a large amount at Fermilab for the MINOS experiment [11] aimed at studying neutrino oscillations. About 100000 SSs based on polystyrene with the dopants 1% PPO and 0.03% POPOP were produced. The strips had a rectangular cross section 4.1 cm wide and 1.0 cm high and their length was 8 m (Fig. 9). The total area covered by the strips was about 28000 m^2. Each strip was coextruded with the reflective material TiO_2 and had a groove in its wide side for the Kuraray Y11 non-S type two-clad WLS fiber 1.2 mm in diameter. The width and depth of the groove were 2.3 and 2.0 mm, respectively. For efficient light collection, the fiber was inserted into the groove deeply and glued to it, and the groove with the fiber was covered with Mylar film.

Scintillator strips for the MINERvA [14] experiment on the study of neutrino–nucleus interactions were produced from the same materials as the strips for MINOS, but they were triangle shaped with a width of 33 ± 0.5 mm and a height of 17 ± 0.5 mm. Holes for WLS fibers were made in the strips simultaneously with their extrusion, and the reflective TiO_2 coating (15% by weight of PS in mixture) was applied (Fig. 10). The hole was 2.6 ± 0.5 mm in diameter. Both ends of the strip were painted by Elijen EJ-510 TiO_2 paint. The total number of the strips was 32000. An advantage of the triangular strips arranged as in

Fig. 10b was better spatial accuracy of measurements and absence of dead zones between the strips.

Very thin 3 × 10 mm strips supposed to serve as active absorber were produced by the extrusion technique for the International Linear Collider (ILC). These strips, together with tungsten as passive absorber, can ensure high segmentation with cells about 1 × 1 cm in size. The light yield and attenuation length of these strips turned out to be comparable with the characteristics of the scintillators produced by the molding technique. In addition, strips irradiated with electrons at a dose of 100 krad, which is equivalent to three-year radiation dose in the central regions of modern colliders, lost about 20% of light yield but completely restored the loss after annealing [15].

Light collection depends not only on the scintillator transparency but also on the quality of the scintillator surface and reflective materials used. Various materials with the reflection factor $R > 90\%$ are used for reflective coating, e.g., aluminized Mylar, TYVEK, TiO_2, MgO, ZnO, $BaSO_4$, various films, white paper, and white paint. The first three materials are most commonly used in physics experiments.

To wrap up tiles for the CDF-II electromagnetic calorimeter, various reflective materials were investigated, among them white paper, E65 film, and Al Mylar. The E65 film was chosen for the lowest light collection nonuniformity of 2.05 ± 0.12% [28].

To wrap up long strips in TYVEK or Mylar is a rather laborious process. The best practical method, developed at MINOS, turned out to be application of TiO_2 coating simultaneously with the extrusion of the scintillator [11]. Pellets of TiO_2 were mixed with polystyrene pellets in an amount of about 15% by weight of the polystyrene and fed into the extrusion line. The thus obtained coating not only features remarkable reflective power but also ensures good adhesion to the base and protection of inner layers against mechanical and potential chemical damage.

The quantity R depends on many factors like the material used, its concentration k, coating thickness, and the technique of its application. In [26] TiO_2 coating with its high refractive index was investigated for light collection and reflection factor as a function of TiO_2 concentration in the mixture with polystyrene. The results were compared with the figures obtained by the world leaders MINOS, Pl.Hi.Tech., and Chemo Technique. It was shown that R increases with increasing TiO_2 concentration, and at $k = 18\%$ it is 96% and the number of photoelectrons is 8.2, which is almost 40% larger than in MINOS. As the TiO_2 concentration continues increasing, the number of photoelectrons increases insignificantly, but there arises a problem of coating nonuniformity during extrusion. The minimum coating thickness (or TiO_2 concentration) is limited by a possibility of ultraviolet photons leaving the coating. The purity of the material and the size of the particles are the factors which are most important for light collection and the reflecting power. The best results were obtained with the strips made from Du Pont materials with the purity of 96 to 97% and the particle size of about 0.2 μm.

Table 4. Attenuation length (L) of plastic scintillator samples as a function of the exposure dose

PS sample	Attenuation length (L), mm	Relative decrease in attenuation length, %	
	before exposure	after dose of 0.5 Mrad	after dose of 1.0 Mrad
SCSN-81	648 ± 43	32 ± 2	41 ± 3
SCSN-38	402 ± 20	16 ± 1	29 ± 2
BC-408	644 ± 12	31 ± 2	32 ± 2

Scintillator tiles based on polystyrene with the FDs 2% p-terphenyl and 0.01% POPOP produced by the Uniplast Company (Vladimir, Russia) using the extrusion technique has a diffuse reflector applied by treating the polystyrene surface with a special chemical solution [27].

Scintillator tiles. Tiles traditionally find wide use in time-of-flight detectors, triggers, and hadronic and

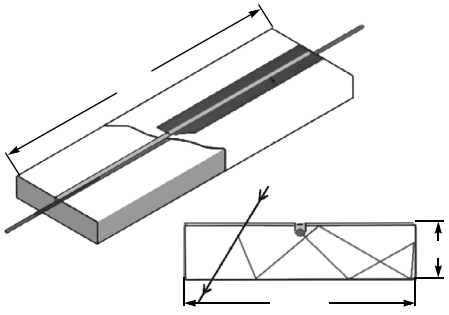

Fig. 9. Strips used in the MINOS experiment [11]: cross section 10 mm by 41 mm, length up to 8 m, groove depth 2.3 mm, and groove width 2.0 mm.

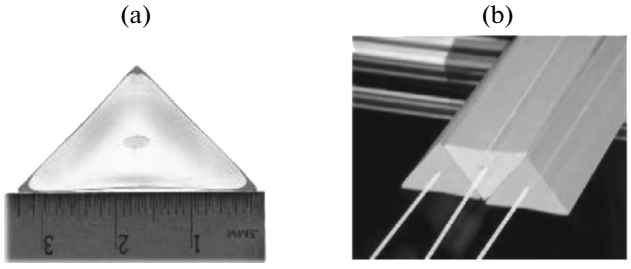

Fig. 10. (a) Cross section of a triangular strip: the wide side length 33 ± 0.5 mm, height 17 ± 0.5 mm, and hole diameter 2.6 ± 0.5 mm; (b) a view of the triangular strips with inserted fibers for the MINERvA experiment [14].

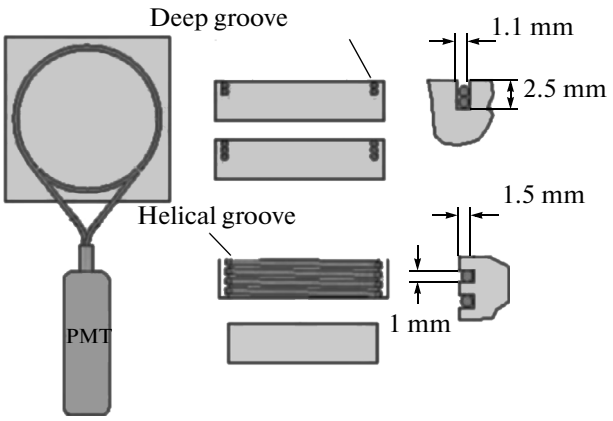

Fig. 11. Drawing of the prototype tiles with different grooves for the PD and SPD of the LHCb spectrometer.

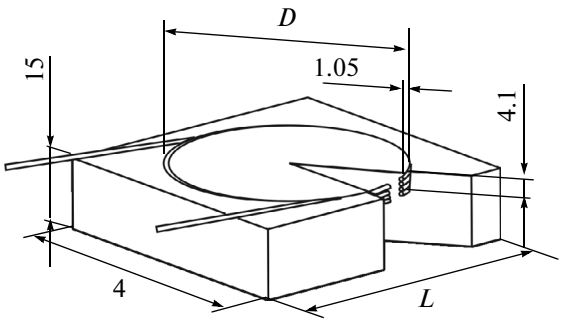

Fig. 12. Drawing of the tile for the PD and SPD of the LHCb spectrometer. All tiles have a square shape and identical thickness of 4.1 mm.

electromagnetic calorimeters. The size, shape, and material of the tiles depend first of all on their destination. Linear dimensions of tiles can vary from a few to ten centimeters.

Tiles for the CDF-II preshower detector [28] and the preshower detector (PD) and scintillation pad detector (SPD) of the LHCb spectrometer [29] were made by cutting them out from scintillator plates and subsequently milling and polishing their sides.

Tiles for the ATLAS hadronic calorimeter were made at IHEP using the injection molding technique [9] with a size tolerance no larger than ± 0.1 mm preset by the mold size precision. Light collection was performed from two opposite sides of the tiles using WLS fibers. The same technique was used at IHEP to produce tiles for the electromagnetic calorimeter (ECAL) of the LHCb spectrometer.

Light collection from the PD and SPD tiles was performed using Y11(250) multiclad WLS fibers 1.2 mm in diameter placed in special grooves cut in the wide side of a tile (Fig. 11). In [29] the dependence of light collection on the shape and depth of the grooves, optical adhesives and greases, number of WLS fiber turns in a groove, scintillator material, and fiber material was comprehensively analyzed. Light yields from the tiles with a deep rectangular groove and a screw-shaped groove (Fig. 11) were compared. It was shown that light yields from both tiles differed insignificantly but the light yield from the tile with the deep groove is more homogeneous than from the tile with the helical groove. Tiles of smaller size also feature more homogeneous light yield. In terms of groove-making simplicity, a deep-groove tile was preferred.

Dependence of the light yield and its uniformity on the shape and depth of the grooves in the tiles and on the groove curve radius was investigated in [29]. The tiles measured $4 \times 100 \times 100$ mm and $4 \times 200 \times 200$ mm. It was shown that smaller-sized tiles with a keyhole-shaped groove 1.7 mm deep with a curve radius of 30 mm had the highest light yield (>3 photoelectrons) and the lowest nonuniformity (~2%) and tile-to-tile light crosstalk (<2%).

The BC-408 scintillators based on PVT have light yield higher by a factor of 1.6 than PS-based scintillators. However, the machining of BC-408, especially groove making, and their use, meet with certain difficulties. A lower light yield of the polystyrene tile can be compensated by its larger thickness. For example, a 15-mm-thick PS tile yields as much light as a 10-mm-thick PVT tile. Considering these points, PS was chosen as a base of tiles for the LHCb spectrometer.

Figure 12 shows a drawing of the tile used in the PD and SPD of the LHCb spectrometer. In one of the tile faces, a groove with a rectangular cross section of 4.1×1.06 mm^2 was cut to house three WLS fiber turns. The modeled tiles of the detectors to be used in different areas relative to the beam were different in size. For example, the groove diameter D and the side L of the tile in the inner, middle, and outer PD areas were $D =$ 37, 56, and 110 mm and $L = 39.5$, 59.5, and 119.1 mm, respectively.

The light yield increased when the BC-600 adhesive or the BC-630 grease was used to insert the fibers into the groove instead of dry setting. The positive effect was about 30% in both cases.

The PD $4 \times 4 \times 1.5$ cm^3 tiles with a deep groove housing 3.5 turns of the Kuraray Y11(250) S-type 1-mm-diameter multiclad WLS fiber glued into it were irradiated by a 50 GeV electron beam. Photomultipliers with a quantum efficiency of 15% were used. The light yield was obtained to be 30 photoelectrons (p.e.) [29].

In the extended $10 \times 170 \times 870$ mm^3 tiles for the KLM detector of the Belle-II spectrometer a 3-mm-deep S-shaped groove was milled to hold the Kuraray Y11 WLS fiber glued into it (Fig. 13). The light collection from both fiber ends to the micropixel avalanche photodetectors with quantum efficiency of 10 to 20% in the green region was 26 photoelectrons [27].

In the CDF-II PD 125 × 125 × 20 mm^3 tiles, an Ω-shaped groove (Fig. 14) was milled to hold two WLS fiber turns from which light was transmitted through an optically clear cable to the 16-channel R5900-16 PMT. This system provides more than 20 photoelectrons from minimum ionizing particles [28].

A special method employing a bundle of WLS fibers was used to collect light from large extended tiles in the CDF-II central muon scintillation detectors [23]. This bundle of densely laid parallel 1-mm-diameter Kuraray Y11(200) S-type multiclad fibers was glued to one of the narrow sides of the long tiles and was covered, like the opposite side, with an Al strip. The wide sides of the scintillator were covered with diffusely reflecting aluminized paper of the "orange skin" type. All sides of the scintillator except the one with the fibers glued to it were thoroughly polished. The fiber ends farthest from the PMT were also polished and an Al mirror was glued to them. The number of the fibers in the bundle was 15 or 20 depending on the tile thickness. Light from all WLS fibers in the bundle was collected in a 2.2 × 2.2 × 6 cm H5783 photodetector (with R5600 PMT) with a photocathode 0.8 cm in diameter and a quantum efficiency of ~12% (Fig. 15).

The cosmic-muon measurements performed with counters 160 and 320 cm long showed the results much higher than the CDF-II requirements: the attenuation length and the number of photoelectrons at the WLS fiber ends farthest from the PMT in different muon subsystems were 290 cm and 37 and 470 cm and 25, respectively [25].

These results were obtained even with WLS fibers whose farthest ends from the PMT were treated using a simplified technology without thorough polishing and Al deposition, which resulted in a reflection factor of about 60% instead of 80 to 90% obtained with the improved technology.

Light emitted by scintillators as charged particles pass through them is predominantly in the ultraviolet region. To transmit this light directly to the PMT is rather difficult and ineffective for several reasons. PMTs with the spectral sensitivity in the ultraviolet region are very expensive, and transmission of ultraviolet light over some distance involves high losses. Therefore, ultraviolet light is usually converted to green light compatible with the sensitivity region of cheaper standard PMTs. Light is converted by wavelength-shifting light guides, or fibers, and further transmitted to the PMT by total internal reflection from thoroughly polished sides of the light guide and surfaces of fibers.

Light from extended scintillators was read out via bar-shaped Plexiglas light guides placed at the light-collecting faces of the scintillator tiles. For efficient light transmission, the tile and light guide faces were polished and separated from each other by a small air gap. If there were no air gap, reemitted light would scatter back to the scintillator. The light guide–scintillation connection areas should be identical (Fig. 16a).

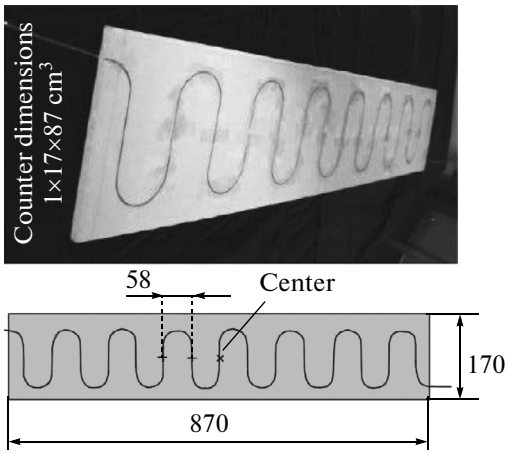

Fig. 13. KLM prototype 10 × 170 × 870 mm^2 tile.

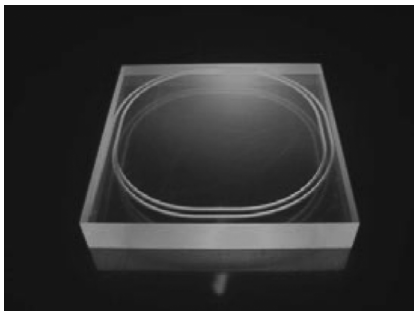

Fig. 14. CDF-II 125 × 125 × 20 mm^2 tile.

Fish-tail light guides are also used. Their flat end is connected to the scintillator end and the round end is connected to the PMT (Fig. 16b). The dimensions of the light guide ends should be identical to the corresponding scintillator and PMT dimensions. Light from large scintillators more than 10 cm wide is collected via an adiabatic light guide assembled of identical Plexiglas strips twisted like a fan (Fig. 16c) [32]. This light guide allows more uniform light collection and ensures identical time of arrival of photons from different areas of the light-collecting scintillator face at the PMT photocathode. Strips are twisted by heating at a temperature of about 150°C.

However, there are difficulties in using these light guides, especially in large spectrometers at modern accelerators. They and PMTs with large-sized photocathodes coupled to them occupy a large space, thus increasing the dead areas. Scintillation counters and PMTs can find themselves in stray magnetic fields, and it is therefore necessary to protect PMTs against the magnetic field. Light guides should be compact, stable, and economical and ensure efficient light collection and coupling to a PMT.

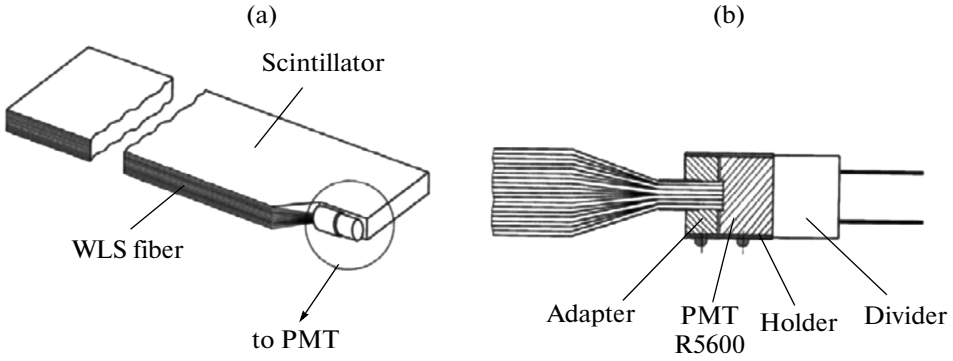

Fig. 15. (a) CDF-II tile with WLS fibers forming a ribbon; (b) connection of the WLS fibers to the PMT [23].

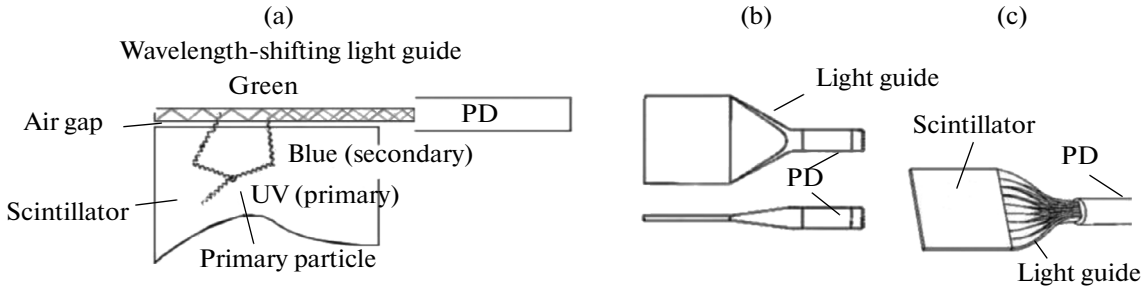

Fig. 16. Types of light guides: (a) wavelength-shifting light guide; (b) fish tail; (c) adiabatic light guide.

Another method of light collection from strips (tiles) that largely meets these requirements is to use WLS fibers inserted into special grooves milled on the surface of a strip (tile) or holes made in strips. With this light collection method, the necessary area of the PMT photocathode and the number of PMTs can be decreased because light from each particular strip (tile) can be transmitted to a particular pixel of the multianode PMT. The use of WLS fibers allows PMTs to be placed outside the spectrometer where the magnetic field effect is insignificant. In this case, light is transmitted to the PMT through clear fibers (fibers without scintillating dopants and wavelength shifters) coupled to the WLS fibers. This method has found wide application in particle physics and nuclear physics experiments where scintillator tiles and extended scintillator strips are used. Their light yields are determined by the geometrical dimensions (length, cross section shape) of the scintillator used, dimensions and shape of grooves or holes, and also by the properties of the WLS fibers and the way of their setting into the grooves' holes.

Losses are lower when light is transmitted to the PMT via the fibers rather than via a fish tail or an adiabatic light guide because in the latter case light travels to the light guide through the bulk of the strip where it is partially absorbed.

Comprehensive study of light collection from a strip using WLS fibers was performed for the MINOS project [11]. One option was to insert fibers into a groove and the other was to insert them into a hole. In both options it was a dry setting. In the former case the light collection was 10% lower than in the latter. Light collection from the fiber glued into a groove was a factor 1.8 higher than from the dry-set fiber. Considering the required effort, the strip with the groove for fiber setting with glue was chosen as a working option. Two samples with an identical thickness of 1 cm and a width of 2 and 4 cm were used to investigate light collection as a function of the strip thickness-to-width ratio. Light collection from the 2-cm-wide strip turned out to be only 1.3 times higher than from the 4-cm-wide strip. Since it is more economical to manufacture a 4-cm strip than two 2-cm strips, the choice was in favor of 4-cm strips.

Wavelength-Shifting Fibers

Ultraviolet scintillation light produced in the strip by a charged particle is partially absorbed and reemitted in the WLS fiber and then transmitted to the PMT by the total internal reflection from the surfaces of the claddings. The main world manufacturers of WLS fibers are Kuraray (Japan) [33] and Saint Gobain Crystals (United States) [34].

Fibers can be single clad and multiclad (mainly double clad), round-shaped with diameters of 0.2 to 2.0 mm, and square-shaped with dimensions of 0.3 to

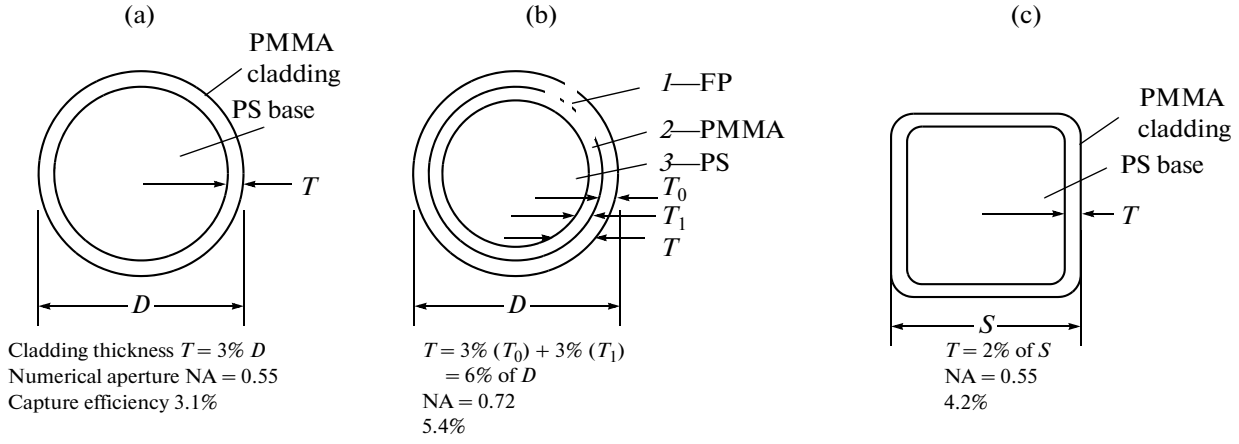

Fig. 17. Schematic views of Kuraray WLS fibers: (a) round-shaped single-clad; (b) round-shaped double-clad; (c) square-shaped.

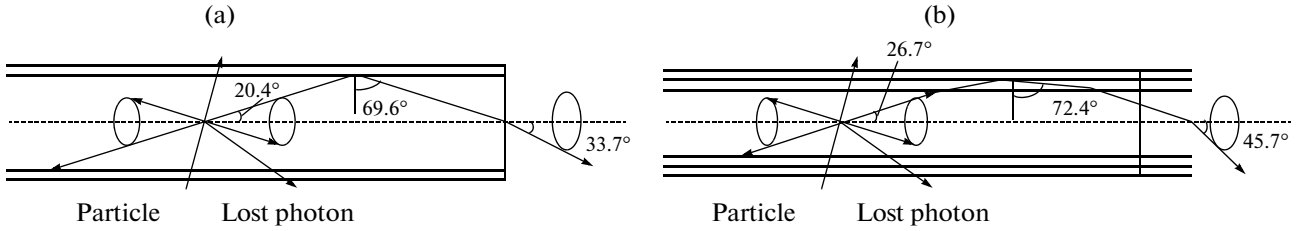

Fig. 18. Scheme of light propagation in a single-clad (a) and double-clad (b) fiber.

3.0 mm (Figs. 17a, 17b, and 17c respectively). Thickness of claddings is about 2 to 3% of the fiber diameter or square side.

The fiber core is most often made from polystyrene, and PMMA is used for the cladding of a single-clad fiber and for the inner cladding of the double-clad fiber. The outer cladding of the double-clad fiber is made from fluorinated polymer (FP) (Fig. 17b).

The refractive index n of the core, inner cladding, and outer cladding is 1.59, 1.49, and 1.42 respectively. This ratio of n contributes to the efficient light collection in the fiber by the total internal reflection in the cladding (claddings). The second cladding with n smaller than n of PMMA provides additional gain in light collection as compared with the single-clad fiber because the light capture cone increases and, consequently, so does the light capture efficiency (from 3.1% to 5.4%) (Figs. 18a, 18b). The outer surface of the fibers is sometimes coated with another cladding, white or black, with a thickness of 10 to 15 μm to eliminate light crosstalk of adjacent fibers [33].

WLS fibers are more transparent to their own emission than scintillators, and their constituent dopants like Y have partially overlapping emission and absorption spectra (Fig. 4b), which leads to the absorption in the short-wave region of the spectrum and reemission in the longer-wave region, where absorption is less significant. As a result, the effective attenuation length of the fiber increases, entailing an increase in the attenuation length of the scintillator with the fiber light guide.

Kuraray manufactures scintillating fibers SCSF-78 (blue) and SCSF-3HF (green, radiation hard) with the attenuation length $L_{att} > 4$ and 4.5 m, respectively, and wavelength-shifting fibers Y7(100) (green) and Y11(K-27) (green) with $L_{att} > 3$ and 3.5 m, which can also be of the non-S type and S type. The former have a more uniform and transparent structure, and the latter are less transparent because of orientation of molecules along the fiber pulling line but more strong mechanically and flexible (see Appendix B) [33].

In the MINOS experiment [11] light collection from the strips was performed using standard (non-S type) Kuraray Y11(175) double-clad WLS fibers 1.2 mm in diameter. This fiber is characterized by a homogeneous structure, high transparency, high light yield, and large attenuation length. The choice of the fiber diameter was dictated by the close packing of eight fibers of 4×4 mm^2 pixels of the 16-anode Hamamatsu PMT to be used in MINOS. WLS fibers 9 m long and clear fibers 3 m long were tested. Ultraviolet light photons produced in the strip and multiply scattered from its reflecting faces are partially absorbed in the WLS fiber, reemitted into green light photons, and then travel over the fiber due to total internal reflection. Signals from long strips were col-

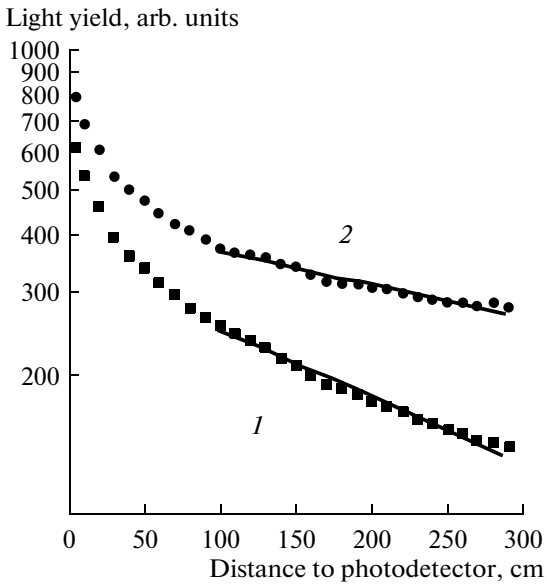

Fig. 19. Light yield of the $7 \times 40 \times 2800$ mm^3 strip as a function of the distance to the PD [27]. Curve *1* is for the fiber without mirroring (attenuation length 302 cm), and curve *2* is for the fiber with mirroring (attenuation length 605 cm).

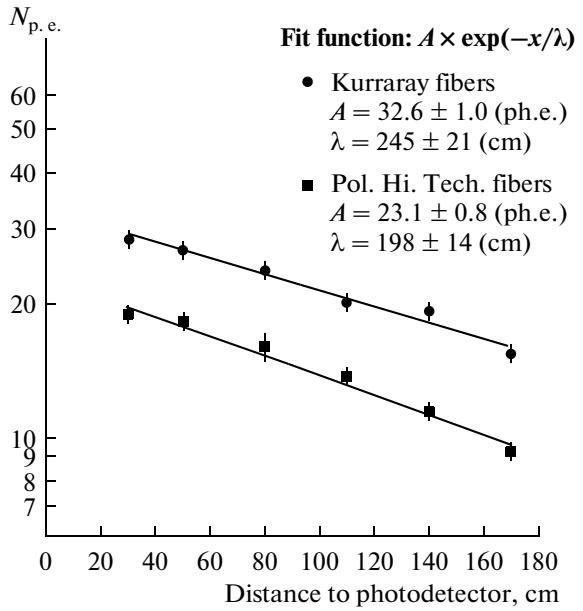

Fig. 20. Light yield of WLS fibers (Np.e.) from different manufacturers as a function of the distance to the PMT [31].

lected at both ends of the WLS fibers, and signals from short strips were collected at one end while the other was mirrored. The mirroring procedure involved ice-polishing, deposition of 99.999% pure Al as the reflective coating, and application of the protective Red Spot UV Epoxy layer.

To reduce loss of light, it is transmitted from the WLS fiber to the PMT through a clear fiber of the same diameter as the WLS fiber. In the WLS fiber the attenuation length is about 5 m, and in the clear fiber it is about 10 m. For example, the clear fibers used in the central tracker of the D0 spectrometer were 800 km long while the WLS fibers were 200 km long [35].

In the D0-II forward proton detector (FPD) intended for measuring small-angle proton and antiproton scattering, BCF-10 double-clad fibers with a square cross section of 0.8 mm were used [36]. The fibers were arranged in groups (0.8×3.2 mm) of four fibers placed in parallel. One end of each fiber was coated with 3-μm-thick Al and the other end was connected to the Bicron BCF98 double-clad clear fiber with the same cross section as the WLS fiber. The clear fibers arranged in groups of four were connected to a channel of the 16-anode H6568 PMT. Their light yield was 10 photoelectrons. Square fibers have an obvious advantage over round fibers in terms of light collection, which amounts to 20% due to a possibility of their closer packing. The spatial resolution of the FPD was about 130 μm.

High light collection (14 photoelectrons) was obtained in [27] with Uniplast $7 \times 40 \times 2800$ mm^3 strips of polystyrene with 2% PTP and 0.01% POPOP. The Kuraray Y11(MC) 1.2-mm-diameter WLS fiber was inserted into the strip groove with optical gel. One end of the fiber was mirrored and the other was connected to the multipixel avalanche photodiode manufactured at the Center for Advanced Technologies and Equipment (Moscow). The active area of the photodiode was 1.27 m^2 and its quantum efficiency was 24%. Figure 19 shows light yields from two WLS fibers as a function of the distance to the photodetector. The upper curve corresponds to the fiber with the mirrored end and the lower to the fiber without mirroring.

Fibers are most often glued into grooves using the Bicron-600 epoxy. In MINOS, Shell Epon 815C epoxy resin with TETA hardener almost identical to Bicron-600 in characteristics was used. Tests of epoxied fibers for mechanical and thermal load revealed quite good strength and quality of the epoxied joint.

Kuraray Y11(200 ppm) WLS fibers have a 40% higher light yield than Pol.Hi.Tech K27(200 ppm) fibers (Fig. 20) [31].

In addition to the light yield, important characteristics of WLS fibers are their mechanical properties, radiation hardness, and time response. Kuraray Y11 and Bicron BCF-91A WLS fibers have approximately identical light yield, but the former shows higher mechanical flexibility at small bending radii, which is particularly important with small-sized tiles. Kuraray S type WLS fibers are used in this case. Time response of the Kuraray Y11 WLS fiber is faster than that of BCF-91A.

Table 5. Time parameters of light signals from scintillators and WLS fibers [23]

Material	Rise time, ns (level 0.1–0.9)	Decay time, ns (level 0.9–0.1)	FWHM, ns (level 0.5–0.5)	Pulse duration, ns (level 0.1–0.1)
UPS-923A	0.8	5.3	3	7.2
UPS-923A + K27	1.7	17.3	7.8	19.1
UPS-923A + Y11	2.2	18	8.8	22.4
Plexiglas	0.23	0.23	0.33	0.65

Light signals of scintillators are characterized by fast rise time and slow (exponential) decay. Table 5 presents time parameters of light signals from the UPS-923A scintillators and from the same scintillators with the K27 and Y11 WLS fibers used to collect light [23]. It also presents time characteristics of Cherenkov light signals from Plexiglas. Apparently, light signals from the scintillators with the WLS fibers have a fast rise time (~2 ns), which makes them suitable for the use in time-of-flight detectors and coincidence systems.

SCINTILLATION COUNTERS IN HIGH-ENERGY PHYSICS EXPERIMENTS

This section deals with the purpose of principle requirements on the scintillation counters used in detectors of large spectrometers both in operation and out of service, such as D0, CDF, ATLAS, CMS, LHCb, ALICE, KLOE, MINOS, OPERA, AMS-2, and some others. Used in the investigations at these spectrometers, scintillation counters made a considerable and sometimes decisive contribution to identification of particles by detecting systems like calorimeters, triggers, trackers, time-of-flight detectors, and veto systems.

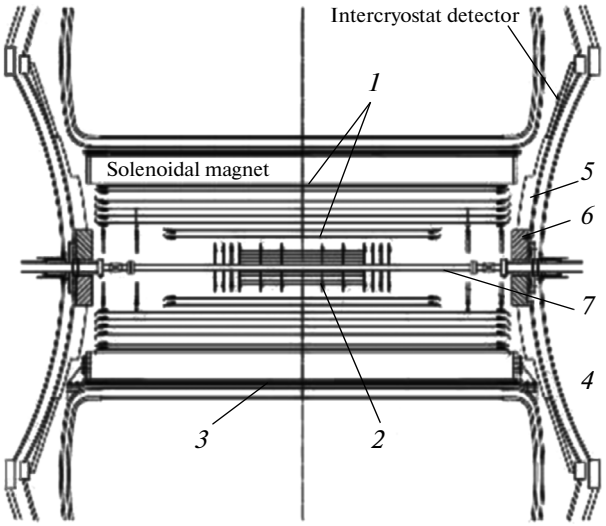

Fig. 21. Schematic view of the D0-II central tracking system [35]: (*1*) central fiber tracker, (*2*) Si microstrip tracker, (*3*) central preshower, (*4*) end calorimeter, (*5*) forward preshower, (*6*) luminosity monitor, (*7*) beam.

Detectors at the Tevatron (D0, CDF)

D0 and CDF spectrometers at Fermilab's Tevatron. After the upgrading the Tevatron in 1996–2000, its luminosity increased by an order of magnitude ($L \sim 3 \times 10^{32}$ cm^{-2} s^{-1}), the center-of-mass energy W grew as high as 1.96 TeV, the time interval between bunches changed from 3.5 μs to 132 ns, and requirements of radiation hardness of detectors became more severe. As a result, some of the detectors of two main Tevatron spectrometers D0 and CDF used in Run I over the period 1992–1996 had to be replaced or upgraded.

D0 tracking system. The central tracking system of the D0 spectrometer was entirely replaced. The new Run II system consisted of the silicon microstrip and scintillation fiber trackers located inside the 2-T superconducting solenoid magnet (Fig. 21) [35]. The central fiber tracker (CFT) consisted of eight cylindrical fiber layers mounted 20 cm (innermost) to 52 cm (outermost) from the beam in the radial direction, covering the pseudorapidity region $|\eta| < 1.7$. Two-layer bundles of WLS fibers were attached to both surfaces of each cylindrical layer (Fig. 22). Kuraray double-clad WLS fibers 835 μm in diameter and 1.66 m long were used for two inner cylindrical layers, and those 2.52 m long for the other six cylindrical layers. The fiber core was made of polystyrene, the inner cladding was of the FD *p*-terphenyl (1% by weight), and the outer cladding was of the wavelength shifter 3-hydroxyflavone (1500 ppm). In this fiber the excitation of

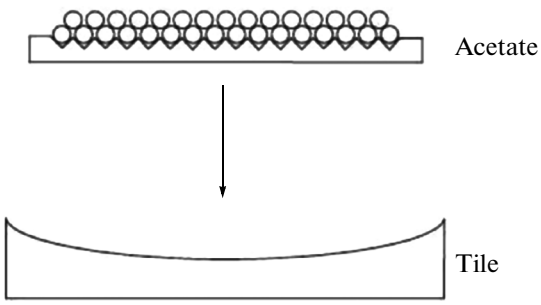

Fig. 22. Schematic view of a two-layer ribbon of WLS fibers [35].

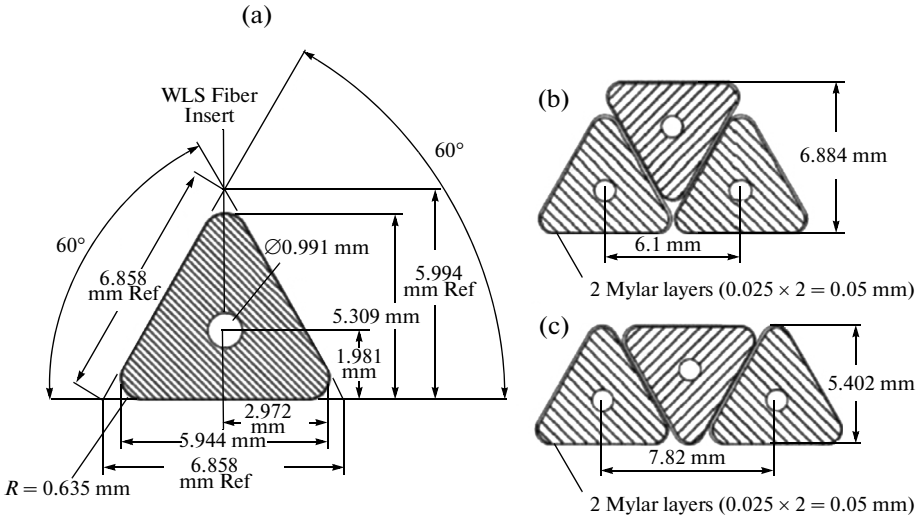

Fig. 23. Cross section of the triangular strip (a) and the layout geometry of the strips in the CPS detector (b) and FPS detector (c).

core molecules caused by a charged particle is transferred to PTP molecules by nonradiative Forster dipole–dipole interactions, and the PTP subsequently emits photons with a wavelength of about 340 nm. The wavelength HF absorbs these photons and reemits photons with a wavelength of 530 nm.

Two-layer bundles of 128 WLS fibers in each layer were made with the fibers inserted into grooves and glued to each other (Fig. 22). The grooves were machined in acryl with high precision. The spacing between the grooves ranged from 928 to 993 μm. The fibers on the lower surfaces of the cylindrical layers were mounted parallel to the beam and the fibers on the upper surfaces were alternatively mounted at an angle of +3° or −3° depending on the layer number. The position of the fibers in the bundle was determined with an accuracy of 25 μm. Some WLS fiber ends were connected to clear fibers that served as light guides and the other ends were mirrored by applying Al with a reflection factor of 90%. The optically clear fibers were 7.8 to 11.9 m long. The light attenuation lengths in the WLS fiber and the clear fiber we1re 5 m and 8 m respectively.

Two hundred fifty-six fibers from each cylindrical layer were inserted in a light-proof box and connected to visible light photon counters (VLPCs). They have high quantum efficiency (higher than 75%), are capable of detecting single photons with a high resolution, and are insensitive to the magnetic field. The VLPCs are housed in a special cassette consisting of eight modules, and a bundle of 128 WLS fibers from each cylinder is routed to each module. Each cassette provides 1024 pixels, and a single VLPC chip consists of eight pixels 1 mm in diameter [35].

Both central tracking detectors determine the primary interaction vertex with a resolution of about 35 μm along the beam.

Preshower detectors. To cover different pseudorapidity (η) regions, the upgraded D0 comprised the central preshower (CPS) detector ($|\eta| < 1.3$) and the forward preshower (FPS) detector ($1.5 < |\eta| < 2.5$). The CPS detector is located in a 5-cm gap between the solenoid magnet and the central calorimeter, and the FPS detector is located in front of the forward calorimeter (Fig. 21).

The preshower detectors fulfill important functions:

—Aiding in electron and photon identification.

—Rejecting background events during triggering and off-line reconstruction.

—Correcting electromagnetic shower energy measurement of the central and end calorimeters for losses in the solenoid, cables, and supports.

In addition, due to fast energy and position measurements, the information from the preshower detectors is included in the Level 1 trigger.

Both preshower detectors are composed of triangular scintillator strips with holes in the central part to insert fibers (Fig. 23a).

The CPS detector is cylinder-shaped and consists of three layers of scintillator strips and an absorber, which is a lead plate ($1X_0$) covered by stainless steel skins ($0.1X_0$). The total thickness of the absorber and the solenoid ($0.9X_0$) was about $2X_0$ for particles passing through detector at an angle of 90°. Each layer contained 1280 strips oriented along the beam in the inner layer and at the angles of 23.774° and 24.016° in the other two layers.

The FPS detector consists of two detectors (north and south). Each of them is made of two pairs of strip planes (layers) separated by an absorber (Pb–Fe, $2X_0$). The strips are arranged at a stereo angle of 22.5° (Fig. 24). Two upstream layers are called the MIP lay-

ers, and two downstream layers behind the absorber are called the shower layers. In the MIP layers electrons, unlike γ rays, will produce signals corresponding to MIPs, and in the shower layers electrons and γ rays will generate showers while heavy charged particles do not generate showers and produce signals similar to those from MIPs.

The triangular scintillator strips were made of polystyrene with 1% *p*-terphenyl and 150 ppm of diphenyl stilbene produced by extrusion, and their light yield was close to that of Bicron 404. Each scintillator strip was machine wrapped in Al Mylar, and the ends were painted white. After the extrusion and wrapping, the scintillator strips tended to bend, which was eliminated by heating them up to 48.9°C and then gradually cooling down to room temperature for two hours.

In both preshower detectors Kuraray double-clad WLS fibers identical to those in the central fiber tracker were used to collect and transmit the light to the end of the scintillator strip. The WLS fibers were inserted in the holes in the scintillator strips, and the strips were arranged as shown in Fig. 23b (CPS detector) and Fig. 23c (FPS detector). Light was collected from one of the fiber ends and transmitted via the optical switch to the clear fiber. The opposite ends of the fibers were diamond polished and coated with silver. The clear fibers were connected to the VLPCs as in the CFT. A total of 86000 VLPCs were used in the CFT and both preshower detectors of the D0 spectrometer.

Run II muon trigger systems (MTSs) for D0. Capabilities of the D0 MTSs in Run II were enhanced by increasing the number of scintillation counters with high segmentation and improved time resolution. Muon counters were grouped into two systems, one covering the central region of $|\eta| < 1.0$ and the other covering the forward region of $1.0 < |\eta| < 2.0$. The central region was composed of two scintillator planes located inside and outside the central toroidal magnet, and the forward region was composed of three scintillator planes, one inside and the other two outside the end toroidal magnet.

The forward muon trigger system (FMTS) was substantially modified to be capable of withstanding the harsh radiation environment typical of this region. The proportional drift chambers used in Run I were replaced by mini drift tubes (MDTs) manufactured at JINR, which featured high radiation hardness, good coordinate resolution (<1 mm), and short drift time (<60 s) [36].

About 5000 scintillation counters were produced for the trigger system. They were made of the Bicron 404A scintillator (emission spectrum maximum at 420 nm, decay time 2.0 ns, attenuation length 1.7 m) by cutting 0.5-in-thick scintillator plates in a trapezoidal shape. The counters were of three sizes: large 60×110 cm^2, typical 24×34 cm^2, and small 18×24 cm^2 [38, 39].

The light guides were Kumarin 30 WLS bars with a cross section of 4.2×12.7 mm^2, whose absorption

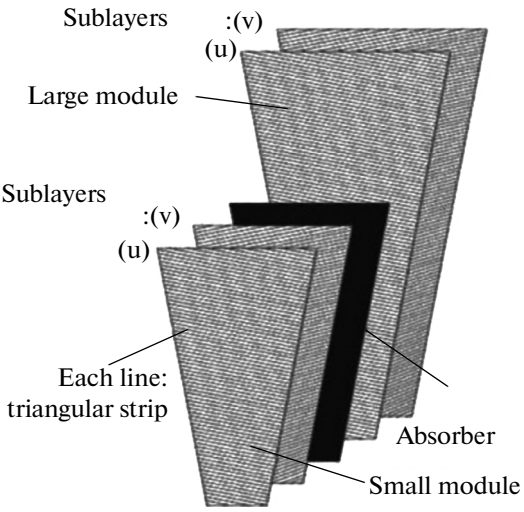

Fig. 24. Structure of the D0 FPS detector.

spectrum corresponded to the scintillator emission spectrum. The counter plate sides were unpolished. Light was collected from two sides of the plate using two bars attached to the scintillator with a small air gap, which allowed more light to be collected and the light to be more uniform. In addition, the cost was decreased. Figure 25a shows a typical FMTS counter.

The bars were bent at 45° for connection to the FEU–115M photomultiplier with a 25-mm-diameter window manufactured at the MELZ factory (Moscow, Russia). These photomultipliers had a quantum efficiency of 15%, green-extended sensitivity spectrum, high light collection of about 10^6, rise time of 2 ns, and shielding against the magnetic field [40]. The scintillator and the light guide were wrapped up in Tyvek and two layers of black paper and placed in an Al casing.

Kumarin 30 bars had a decay time of 2.7 ns, emission wavelength maximum of 460 nm, and attenuation length of 1.4 m; the respective characteristics of the Bicron 404A scintillator are 2.0 ns, 408 nm, and 1.7 m [41].

Tests of the counters in the 127-GeV/*c* muon beam with the appropriate selection of high voltage showed their high efficiency (99.8%) and time resolution better than 1 ns (Fig. 25b) [35]. The mean number of photoelectrons was 60 and 184 for large and small counters, respectively. Thus, this system of scintillation counters met the time resolution requirements placed on them as D0 forward muon system triggers.

Time-of-flight measurements at CDF-II. Time-of-flight measurements require scintillation detectors meeting high time resolution requirements on both the scintillators themselves and photodetectors.

To improve identification of low-energy π and K mesons, the CDF-II time-of-flight system was made up of scintillation counters based on $4 \times 4 \times 279$ cm^3 BC-408 scintillator strips [42]. Each of 216 strips was

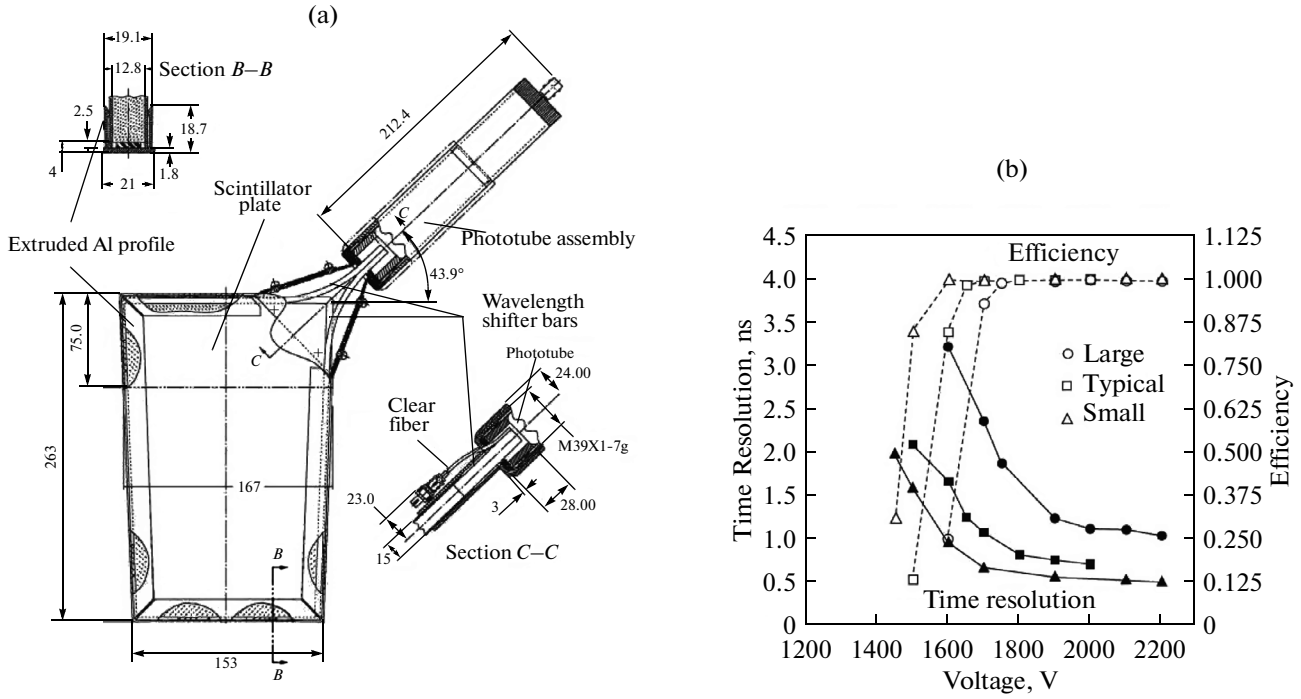

Fig. 25. (a) Typical FMTS counter; (b) FMTS efficiency and time resolution.

wrapped up in white paper. Light collection was performed from both ends of the strips to the Hamamatsu 7761 PMT with fine meshes capable of operating in the magnetic field of 1.6 T. The contact of the strip ends with the PMT was through optical adhesive and special powder; the PMT was spring loaded to ensure good contact. The time resolution was about 100 ps, which allowed K/π and P/π discrimination at a level of 2σ in the momentum region up to 1.6 GeV/*c*.

The mass m of a particle is calculated using its momentum p and free path L measured by the central tracking drift chamber and its time of flight measured by the time-of-flight system

$$m = p/c\sqrt{c^2t^2/L^2 - 1} \text{ and}$$
$$\omega_K(t_K) = (t_K - t_0)/\sqrt{\sigma^2_{ik} + \sigma^2_{to}} = \Delta t_k/\sigma_t.$$

A good time resolution of the scintillation counter was obtained in [43]. The scintillation counter was made of polystyrene with 3% *p*-terphenyl and 0.04% POPOP and used modified FEU-87 photomultiplier tubes. Those PMTs were modified by selecting an appropriate high voltage divider to ensure maximum focusing of electrons near the optimum trajectory in the PMT. Monoalkali cathodes (SbCs) were used. With those PMTs, the time resolution of the detector was about 70 ps, which improved P/K/π identification using also ionization measurements of time-projection chambers in the momentum range of 3 to 8 GeV/*c*.

Those counters were used in the 900-channel time-of-flight systems of the facilities NA49 at CERN [44] and SFERA at JINR [45].

Muon triggers of the CDF-II spectrometer. Identification of μ mesons is of major importance for selecting and searching for candidate events for production of top quarks, W bosons, and H bosons because decays of these particles involve μ mesons. Scintillation counters are used in the on-line muon trigger system for identifying μ mesons in combination with drift chambers. They are located behind the central calorimeter and a massive Fe wall 61 cm thick that almost entirely absorbs particles leaving the target except muons and neutrinos. The system of muon scintillation counters covers the pseudorapidity region $-1.5 < \eta < 1.5$. Since the upgrading of the Tevatron in 1996–2000 required muon detectors with high segmentation and good time resolution, it was decided to use scintillation counters made at JINR from polystyrene scintillators with 2% PTP and 0.03% POPOP manufactured by ISMA. The scintillators measured $160 \times 16 \times 1.5$ and $320 \times 30 \times 2$ cm^3 and were used in two CDF-II subsystems, CSP (Central Scintillator uPgrade counters) and BSU (Barrel Scintillator Upgrade counters) (Fig. 26) [46]. About half of 1200 CDF-II counters were substituted with the above counters.

All surfaces of the scintillator were polished to purity class 12 and wrapped in diffusely reflecting aluminized paper. Light was collected from one of the scintillator sides and transmitted to the PD via Kuraray Y11(200) S-type double-clad WLS fibers

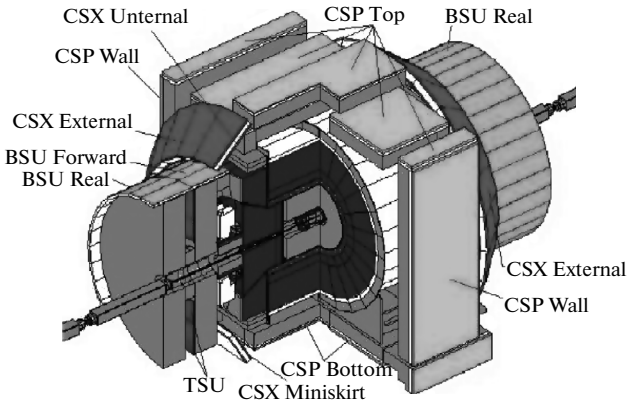

Fig. 26. Arrangement of scintillation counters in the CDF-II spectrometer [46].

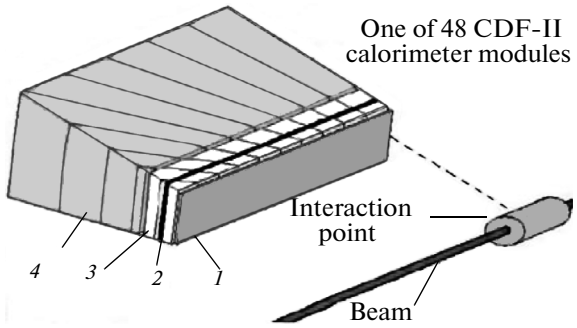

Fig. 27. CDF-II calorimeter module [48]: (*1*) preshower detector, (*2*) electromagnetic calorimeter (maximum shower), (*3*) electromagnetic calorimeter, (*4*) hadronic calorimeter.

assembled into a bundle (Fig. 15). There were 20 or 15 fibers in the bundle depending on the width of the scintillator side. The fibers were 1 mm in diameter, and their attenuation length was 250 cm [47]. The ends of the fibers were bundled, polished, and connected without grease to the compact Hamamatsu H5783 photodetector based on the 5600 PMT, for which a special small cut was made. The opposite ends of the fibers were treated by a simplified process (without thorough polishing and Al deposition), which resulted in a reflection factor of about 60%.

These fibers also substituted for fish-tail Plexiglas light guides in some of the old scintillation counters, which appreciably increased light collection from them.

Measurements with cosmic muons yielded results that met the CDF-II requirements. The number of photoelectrons at the WLS fiber ends farthest from the PMT in different subsystems was 37 (BSU), 25 (CSU), and 21 (WSU). The effective attenuation lengths were 290 (BSU), 470 (CSU), and 350 cm (WSU).

CDF-II preshower detector [28, 48]. The considerably increased luminosity of the Tevatron in Run II, $\sim(2-5)\times10^{32}$ cm^{-2} s^{-1}, imposed more severe requirements on the CDF-II preshower detector. In Run I the PD consisted of slow proportional chambers with a relatively weak signal and low operation speed, resolution, and segmentation. In Run II these chambers were replaced by scintillation detectors, which increased the operation speed and segmentation of the detector and improved both identification of electrons and single photons against the π meson background, as well as energy resolution of jets. The background of charged π mesons decreased by a factor of 2 to 3. The η segmentation increased by almost an order of magnitude [28, 48].

The detector was made from $125\times125\times20$ mm^3 tiles of the ISMA-manufactured scintillators with Ω-shaped grooves milled on their surface (Fig. 13). Light was collected from the tiles using WLS fibers arranged in two rows laid in the grooves. The light collection was at least 20 photoelectrons from a tile and 12 photoelectrons at the exit of the entire optical channel according to the data averaged over all tiles of one module. A detector module was assembled of 54 tiles, and the total number of modules was 48 (Fig. 27). The light collected from each tile by the WLS fiber was transmitted via 5-m-long optically clear fibers to one of the pixels of the 16-channel Hamamatsu R5900-16 PMT. The optically clear fibers from Pol.Hi.Tech. with the attenuation length of 7 m were used.

Detectors at the LHC (ATLAS, CMS, LHCb, ALICE)

After the Large Hadron Collider with its center-of-mass energy of colliding particles up to 14 TeV, luminosity of 10^{34} cm^{-2} S^{-1}, and the bunch-crossing rate of 40 MHz was commissioned at CERN, there arose a need for detectors with high time, spatial, and energy resolution capable of operating in a very harsh radiation environment. Among the main objectives of LHC experiments were the search for and discovery of new particles, first of all H bosons (ATLAS, CMS) and rare B meson decays (LHCb), and investigation of quark–gluon plasma in interactions of heavy nuclei (ALICE). Of particular aid in fulfilling those objectives were specific H boson and B meson decay modes, which involved high-energy leptons and γ rays, and the major tools for their identification were calorimeters with scintillators extensively used as an active absorber.

Calorimetry. Calorimeters are used to measure energy depositions and coordinates of particles and showers and also serve as triggers for selecting particular events. Calorimeters consist of a passive and an active absorber (sampling calorimeters) or only one absorber combining the functions of both (homogeneous calorimeters). Particle energy is predominantly absorbed by the passive absorber, which must be large enough to absorb as much particle energy as possible. At energies in the region of 1 TeV, the absorber thick-

Table 6 [49]

Characteristics	CsI	BGO	$PbWO_4$	Liquid Ar	Liquid Kr
ρ, g/cm^2	4.53	7.13	8.28	1.4	2.5
X_0, cm	1.85	1.12	0.89	14	4.7
R_M, cm	3.8	2.1	2.2	7.2	4.7

ness must be about $30X_0$ (18 cm Pb) to ensure full containment of electromagnetic showers and about 11 nuclear lengths (2 m Fe) for full containment of hadronic showers. Passive absorbers are usually substances with large Z (Cu, Fe, W, Pb, U) and active absorbers are predominantly polystyrene scintillators (tiles or WLS fibers) and liquid argon. Homogeneous calorimeters use various inorganic crystals ($PbWO_4$) and liquefield noble gases (Ar, Kr, Xe).

Calorimeters allow discriminating particles, e.g., distinguishing electrons and γ rays from hadrons and muons, and are usually segmented into a lot of cells no larger than characteristic transverse dimensions of showers in a particular experiment. It is therefore possible to determine coordinates of the particle that caused the shower with an accuracy better than the size of the cell. For example, the azimuthal angle (π) and pseudorapidity ($\acute{\eta}$) segmentation of the CMS hadronic calorimeter and the internal segments of the ATLAS hadronic tile calorimeter are respectively $\Delta\varphi\Delta\acute{\eta} = 0.087 \times 0.087$ and 0.01×0.01, where $\Delta\varphi$ is in radians.

The calorimetric system of large spectrometers usually consists of electromagnetic calorimeters (ECALs) followed by hadronic calorimeters (HCALs) and preceded by a preshower detector (PSD).

The PSD consists of two layers of a highly segmented active absorber with a layer of a passive absorber (Fe, Pb) about $2X_0$ thick sandwiched between them. The PSD allows separating of electrons and γ rays before they hit the ECAL and distinguishing of single γ rays from π^0 from γ rays of meson decay, and π mesons from electrons.

The characteristic dimensions of the electromagnetic and hadronic showers produced in calorimeters by electrons/γ rays and hadrons respectively dictate (at the given energy of the primary particles and calorimeter working material) the length (thickness) of the calorimeter and the size of the calorimeter cells (segments).

The length over which the electromagnetic shower develops to its maximum is

$$t_{max} \approx \ln(E_0/E_t) + c_i,$$

where E_0 is the energy of the primary particle (e or γ), Ec is the critical energy, and $c_i = -0.5$ for electrons and $+0.5$ for gammas. The transverse dimension of the electromagnetic shower is mainly determined by multiple scattering of electrons and positrons and by bremsstrahlung photons from those particles. It is usually specified by the Molière radius R_M, a radius of an infinitely long cylinder within which 95% of the shower energy is concentrated, and calculated by the formula [49]

$$R_M \text{ (g/cm}^2) \approx 21\ X_0/E_c, \text{ where } E_c \text{ is in MeV.}$$

The length of the calorimeter is dictated by the requirement of absorbing a particular amount of the shower energy. For example, to absorb 98% of the shower energy, the ECAL length in units of X_0 should be such as to obey the relation

$$L(98\%) \approx 2.5t_{max} \text{ [49].}$$

Table 6 presents densities ρ, radiation lengths X_0, and Molière radii R_M for a number of the most commonly used materials.

Development of hadronic showers has specific features that substantially affect the HCAL design, dimensions, segmentation, and energy and spatial resolution.

Hadronic showers consist of (i) an electromagnetic component, which involves decays of π^0 and $\acute{\eta}$ mesons into γ rays initiating electromagnetic showers, and (ii) a nonelectromagnetic component, which involves all the other hadrons, nuclear fragments, and also neutrinos and μ mesons leaving the calorimeter without producing any signal.

The electromagnetic component f_{em} strongly fluctuates from event to event and accounts for a considerable fraction of the primary hadron energy E_0, which increases with E_0 to ≈30% at 10 GeV and ≈50% at 100 GeV. The rest of the shower energy is accounted for by ionizing particles (56%, 2/3 by protons), 10% by neutrons, and 34% by invisible energy (nucleon binding energy in a nucleus) [50]. Due to invisible energy, hadron responses in the HCAL are lower than those from electrons, which deteriorate the energy resolutions and call for compensation.

Compensation can be performed by (i) suppressing the electromagnetic component response, (ii) enhancing the hadronic component response, and (iii) using off-line compensation.

Suppression of the electromagnetic component response is based on the fact that most of the electromagnetic shower photons have energy <1 MeV and thus lose it mainly due to the photoeffect with a cross section of $\sim Z^5$. Heavy materials like U almost completely absorb these photons. The electromagnetic

component response can be additionally suppressed by shielding the absorber with thin Fe foils.

The hadronic component response can be enhanced using ^{238}U fission since γ rays and evaporation neutrons resulting from the fission carry away the energy that partially compensates for the invisible energy. Soft neutrons elastically scattered from protons transfer part of their energy to the protons which produce detectable signals in the active absorber.

Compensation can be obtained by selecting the optimum ratio between the thicknesses of the passive and active absorbers. It is, for example, 4 : 1 for Pb/scintillator and 1 : 1 for U/scintillator.

The hadronic shower extension is characterized by the nuclear interaction length $\lambda_h \sim A^{1/3}$ g/cm^2, which is much larger than the radiation length X_0. Table 7 lists X_0 and λ_h values for a number of the most often used materials [49].

For 99% hadronic shower containment, calorimeters should have the length (thickness) $3.5\lambda_h$ at the primary pion energy 10 GeV and $7\lambda_h$ at 100 GeV. Figure 28a shows energy dependences of the calorimeter thickness for the pion shower containment at the 95% and 99% levels, and Fig. 28b presents dependences of the shower containment in the Pb absorber on the radius of an infinite cylinder at the pion energies 10, 40, and 150 GeV [51].

The most important characteristic of the calorimeter is its energy resolution. There are many factors that affect it:

—Statistic fluctuations of the number of particles in the shower.

—Fluctuations of shower leakage from the calorimeter.

—Electronic noise.

—Sampling fluctuation.

Table 7

	X_0		λ_h	
	g/cm^2	cm	g/cm^2	cm
Liquid Ar	30	14	119.7	83.7
Fe	13.8	1.76	132	16.8
Pb	6.3	0.56	193	17.1
U	6.1	0.32	199	10.5

The energy resolution of a calorimeter is described by the formula

$$\sigma_E/E = a/\sqrt{E} \oplus b/E \oplus c.$$

Its first term is the stochastic term determined by the fluctuations of the number of particles that produce signals in the active absorber (sampling fluctuations), the second term is determined by the electronic noise, and the third term is a constant depending on many factors, including fluctuation of shower energy losses in the longitudinal direction, nonuniform signal collection, imperfect calorimeter design, fluctuation of energy losses in the calorimeter itself and in inert materials, and calorimeter calibration.

The sign ⊕ hereafter means quadratic addition of all terms.

Below we consider calorimeters of the ATLAS, CMS, and LHCb spectrometers which feature high energy and spatial resolution obtained due to up-to-date innovations. The emphasis will be placed on the use of scintillators and light collection, and transmission of their signals via WLS fibers.

ATLAS hadronic tile calorimeter [52]. It is a noncompensating ($e/h = 1.4$) sandwich calorimeter made of alternating steel plates (14 mm) and polystyrene scintillator tiles (3 mm), which is designed for a preci-

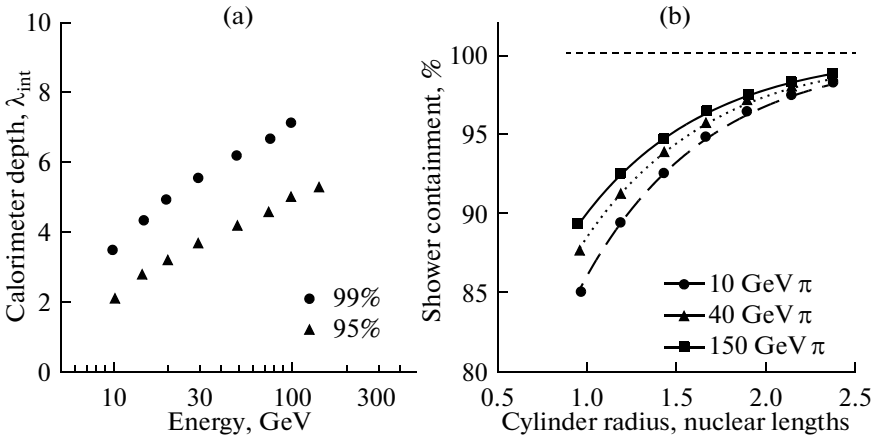

Fig. 28. (a) Depth of the calorimeter (Fe) as a function of the pion energy for two containment levels (95% and 99%); (b) dependence of the shower containment in the Pb calorimeter on the radius of the infinitely long cylinder in units of nuclear lengths at the pion energies of 10, 40, and 150 GeV.

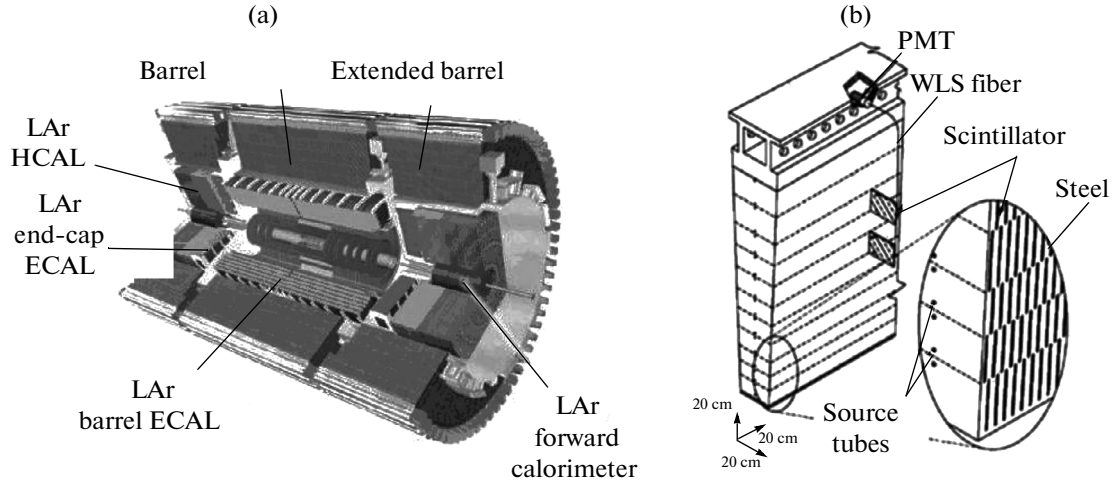

Fig. 29. (a) General view of the ATLAS calorimeters; (b) schematic view of the tile calorimeter module.

sion determination of energies and coordinates of hadrons and showers in a combined operation with other ATLAS calorimeters. It is subdivided into three barrels with an inner radius of 2.28 m and an outer radius of 4.25 m, which cover the regions $|\eta| < 1.0$ (central barrel) and $0.8 < |\eta| < 1.7$ (lateral barrels) (Fig. 29a). The calorimeter is assembled from 64 wedge-shaped modules (Fig. 29b). Due to the liquid argon + Cu sandwich calorimeter the hadronic tile calorimeter was extended into the pseudorapidity region $1.5 < |\eta| < 3.2$.

The calorimeter uses about 460000 trapezoidal tiles of 11 standard sizes with a length ranging from 200 to 400 mm, width ranging from 97 to 187 mm, and identical thickness of 3 mm within a size tolerance of ±0.1 mm. The tiles were made from polystyrene with FDs using the injection molding technique [9]. Signals are collected from two opposite sides by WLS fibers connected to the Hamamatsu 7877 PMT with an active area of 26×26 mm^2 and with the body and dynodes made of metal. Each tile is calibrated and monitored using a radioactive Cs^{137} source moved by a liquid in a tube set in motion by a hydraulic drive. A distinctive feature of the ATLAS tile calorimeter is that the tiles are orientated orthogonally to the beam.

Each module was radially segmented into three sections measuring 1.5, 4.1, and 1.8 nuclear lengths in the central section and 1.5, 2.6, and 3.3 nuclear lengths in the lateral sections. The total nuclear length with allowance for the module supports (1.3) was about 11 nuclear units, enough for full containment of hadronic jets. Segmentation of the calorimeter in $\Delta\eta$ (pseudorapidity) and $\Delta\varphi$ (azimuthal angle) was $\Delta\eta\Delta\varphi = 0.1 \times 0.1$ except for the last segments, where it was 0.1×0.2, which is smaller than characteristic transverse dimensions of showers and thus allows coordinates of jets to be measured with good accuracy.

The energy resolution of the tile calorimeter measured in the beam is described by the formula [51]

$$\sigma_E/E = (52.9 \pm 0.9)\%/\sqrt{E} \oplus (5.7 \pm 0.2)\%.$$

ALFA detector of the ATLAS spectrometer [53]. This detector is intended for high-precision measurements of the LHC luminosity using small-angle proton–proton scattering. It is located ±240 m away from the interaction point in Roman Pots and is inserted in the vacuum tube as close as 1 mm to the beam axis. ALFA is a high-precision tracking detector made of ten double-sided modules, each with 64 Kuraray SCSF-78 S-type fibers with a square cross section of 0.5×0.5 mm^2 arranged in the u–v geometry. Signals from the fibers are read out by the 64-anode Hamamatsu R7600-64 photomultipliers. Special attention was given to suppressing crosstalk of the fibers. To this end, fibers were subjected to vacuum Al deposition and their claddings were painted black. The spatial resolution of 25 μm was obtained, which met the requirements on the detector.

Hadronic calorimeter of the CMS spectrometer [54]. The CMS spectrometer comprises a homogeneous electromagnetic calorimeter made of ~80000 $PbWO_4$ crystal and a sandwich-type noncompensating ($e/h = 1.4$) hadronic calorimeter made of interleaving brass and polystyrene tiles. In front of the end-cap ECAL there is a preshower detector (Fig. 30).

Since the HCAL is in the magnetic field of the solenoid (3.8 T), a nonmagnetic material, brass (70% Cu + 30% Zn), was chosen to be the absorber, and Kuraray SCSN81 with its long-term stability of characteristics and moderate radiation hardness was chosen to be the basic scintillator. For example, SCSN81 scintillators 3.7 mm thick were used in layers 1 to 15 of the HB calorimeter and those 9 mm thick in layer 16. The so-called layer 0 was made up of 9-mm-thick BC-408 scintillator. Brass plates were 50.5 and 56.5 mm thick in the HB and 80 mm thick in the HE.

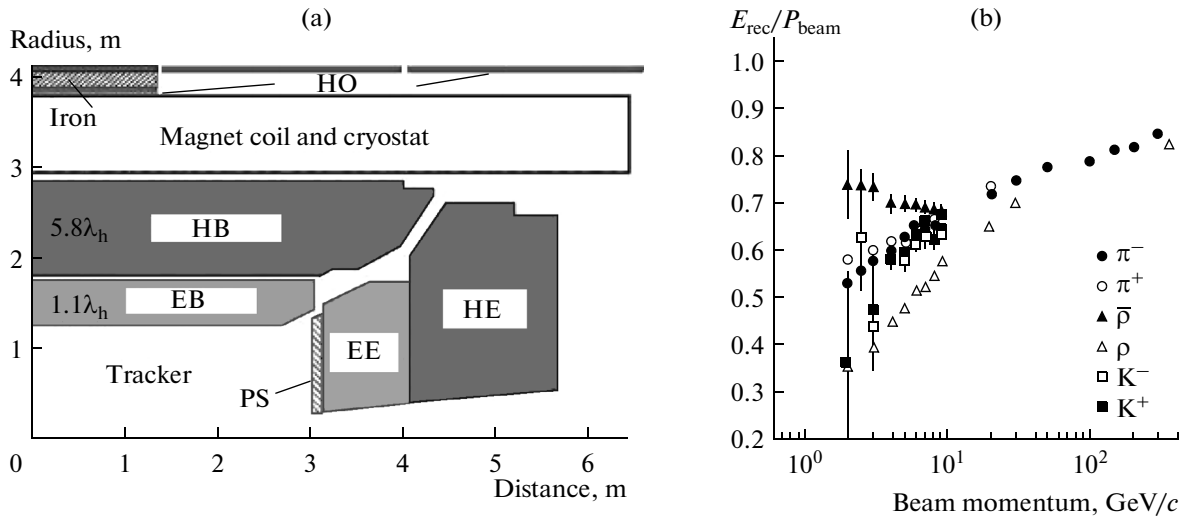

Fig. 30. (a) Arrangement of CMS calorimeters: EB and EE are the barrel and end-cap sections of the ECAL, HB and HE are the barrel and end-cap sections of the HCAL, and PS is the preshower detector. HB and HE thickness are given in units of the nuclear length λ_h at $\eta = 0$; (b) responses of various particles in the combined calorimetric systems as a function of the beam momentum.

Thirty-six modules (towers) were assembled from these tiles and plates for the barrel calorimeter (HB) and two end-cap calorimeters (HE) (Fig. 30). The total thickness of a module at $\eta = 0$ and 1.3 was 5.82 and 10.6 nuclear lengths, respectively. Due to the use of $PbWO_4$ in ECAL, the total nuclear length was increased by 1.1 irrespective of η. In addition to the HB, the Hadron Outer calorimeter (HO) is mounted outside the magnet coil to increase the total nuclear length thickness of the hadronic calorimeter and avoid possible leakage. The HB and HE cover the region $|\eta| < 3$. The pseudorapidity region of the hadronic calorimeters was increased ($3 < |\eta| < 5$) by installing quartz-fiber forward calorimeters.

Signals from the tiles were collected and summed using Kuraray Y11 WLS fibers 0.92 mm in diameter inserted in grooves milled on the wide side of the tiles. Fibers from all layers of a tower were arranged into bundles 4.8 mm in diameter, making up one of 10000 readout channels. Since the HCALs (except the HO) were located within the strong magnetic field, hybrid avalanche photodiodes (HAPDs) were used as photodetectors. However, because of the inhomogeneity of the magnetic field in which the HO HAPDs operate, they are gradually replaced with micropixel avalanche photodiodes (MAPDs). The high HCAL segmentation in η and φ ($\Delta\eta$, $\Delta\varphi$) = (0.087, 0.087) allowed responses of various shower particles to be thoroughly investigated at energy <10 GeV (Fig. 30b) [54]. This investigation is of great interest in view of the experiments at the projected ILC, in which detailed identification of all shower particles is supposed.

Calorimeters of the LHCb spectrometer [29, 55]. The main objective of the LHCb experiment is precise measurement of B meson decays for CP asymmetry investigations. The objectives to be solved by the LHCb calorimeter system were (i) searching for rare B meson decays like radiative decays B_d–$K\gamma$, and B_s–$\varphi\gamma$; decays involving π^0 and η B_d–$\pi^+\pi^-\pi^0$, $J/\psi\eta$, and D_0–$K^-\pi^+\pi^0$; and decays involving e $B - K^*e^+e^-$, and (ii) detecting hadrons, e, γ, and π^0 with high P_t.

This required reliable identification of electrons, gammas, and hadrons, measurement of their energies and coordinates, and discrimination between single γ rays and π^0 decay γ rays. These requirements dictated the structure and characteristics of the calorimetric system to be used.

The LHCb calorimeter system consists of an electromagnetic calorimeter (ECAL) and a hadronic calorimeter (HCAL). A scintillating pad detector (SPD) and a preshower detector (PSD) with a $2.5X_0$-thick Pb absorber are mounted in front of the ECAL.

The SPD and the PSD are two highly segmented scintillation planes made up of tiles of three standard sizes (cells) with an identical thickness of 15 mm. The characteristics of the tiles are given in the first section, subsection *Scintillation tiles*. The SPD determines whether particles hitting the calorimeter system are charged or neutral, and the PSD determines whether the incident particle is an electron or a γ ray (which initiate an electromagnetic shower) or it is a π meson (there is no electromagnetic shower). The total number of the scintillating pads was about 12000. The PSD in combination with the ECAL are used in the trigger logic to indicate presence of e, γ rays, and π^0 mesons.

Segmentation of the SPD/PSD corresponds to that of the ECAL: each SPD and PSD plane was divided into three sections, inner (3072 4×4 cm^2 cells), middle (3584 6×6 cm^2 cells), and outer (5376 12×12 cm^2 cells). This segmentation of the calorimeter system was dictated by the fact that the parti-

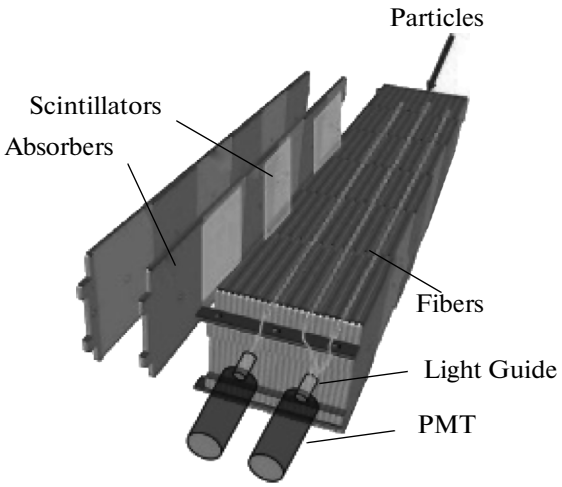

Fig. 31. Schematic view of the LHCb hadronic calorimeter.

cle flux density varies by almost two orders of magnitude over the surface of the calorimeters.

Light from the tiles is collected using WLS fibers. Three and a half coils of fiber are laid into the groove made in the tile. Clear fibers are used to transmit light from the WLS fibers to the photomultiplier. This system allowed collection of 20 to 30 photoelectrons per cell from minimum ionizing particles. Photomultipliers with 64 channels and 2×2 mm^2 pixels, each connected to one WLS fiber, were used. The number of photomultipliers needed for reading ~12000 pads was thus reduced to ~200.

The e/π discrimination of the prototype PSD was tested in the SPS e and π beams at momenta of 10 to 50 GeV/c. The measurements showed that rejection of π mesons at the cutoff threshold of five minimum ionizing particles was 99.6, 99.6, and 99.7% with e kept at a level of 91, 92, and 97% at the momenta of 10, 20, and 50 GeV/c, respectively [29].

LHCb hadronic calorimeter [29, 55]. The LHCb HCAL is a sandwich calorimeter of Fe plates 16 mm thick interspaced with scintillator tiles 4 mm thick (Fig. 31). The plates are arranged parallel to the beam. In the lateral direction tiles are interspaced with 1 cm of iron (matching with one radiation length), while in the longitudinal direction the total length of the alternating Fe spacers and scintillator tiles corresponds to the nuclear interaction length in iron. Light collected by Kuraray Y11(250) MSJ 1.2-mm-diameter WLS fibers running along the tiles is transmitted to the PMT.

The transmitted light is attenuated, which results in nonuniform light collection from the tiles located at different distances from the PMT. To eliminate this effect, the contact between the fiber and the tile was adjusted. For example, the contact between the PMT and the nearest tiles was made 22% weaker than that between the PMT and the farthest tiles. This procedure allowed the light collection uniformity at a level of a few percent to be obtained.

The LHCb HCAL segmentation is like that of the ECAL, where cells of the inner section are 13×13 cm^2 and those in the outer section are 26×26 cm^2.

The energy resolution of the HCAL is expressed by the formula [29]

$\sigma_E/E = (69 \pm 5)\%/\sqrt{E} \oplus (9 \pm 2)\%$, where E is in GeV.

Detectors of the Shashlik and Spaghetti Type

LHCb electromagnetic calorimeter. The LHCb ECAL is a shashlik-type calorimeter made of alternating lead plates and scintillator tiles with holes for setting WLS fibers. A typical feature of such a calorimeter is high homogeneity and time resolution, radiation hardness, and reliable operation.

The ECAL was assembled from individual modules 42 cm long with a cross section of 12.2×12.2 cm^2, each being a stack of 67 scintillator tiles (cells) 4 mm thick and 66 lead plates 2 mm thick. Modules of three types that differed by the size and number of cells were used in accordance with the flux rate. Each layer of modules consisted of nine in the inner, heaviest-flux region, four 6×6 cm^2 cells in the middle region, and one 12×12 cm^2 cell in the outer region. The tiles and lead plates had holes for setting WLS fibers 10.1 mm distant from each in the inner and middle modules and 15.35 mm in the outer modules. The number of fibers in the cells of the inner, middle, and outer modules was 9, 36, and 64 respectively. Figure 32a shows the inner module with nine tiles in a layer, and Fig. 32b presents three types of modules used in different ECAL regions. Light was collected using Kuraray Y11(250)MSJ 1.2-mm-diameter WLS fibers. For better light collection each fiber formed a loop traversing the module twice. Light was detected by Hamamatsu R7899-20 PMTs.

The total radiation length of the module is $25X_0$, and the Molière radius is 3.5 cm. The total number of modules is 3312. The scintillator tiles were made using the injection molding technique [9]. The edges of the tiles were chemically treated to have a diffusely reflecting surface, which allowed tile-to-tile crosstalk to be eliminated and light collection from module edges of inert materials ~0.2 mm thick to be improved. However, this treatment of tile edges resulted in a 30% decrease in the light collection as compared with tiles with polished edges.

The energy resolution of the calorimeter strongly depends on uniformity of light collection from tile to tile. Measurements revealed a light collection spread from tile to tile, but special treatment of the tile edges reduced it to less than 2.5% of the root-mean-square error. The ECAL energy resolution measured in the e and π beams with the momenta of 10 and 50 GeV/c at SPS channel X7 at CERN is expressed by the formula $\sigma/E \sim 9\%/\sqrt{E} + 0.8\%$ [29]. It is worse than that of the

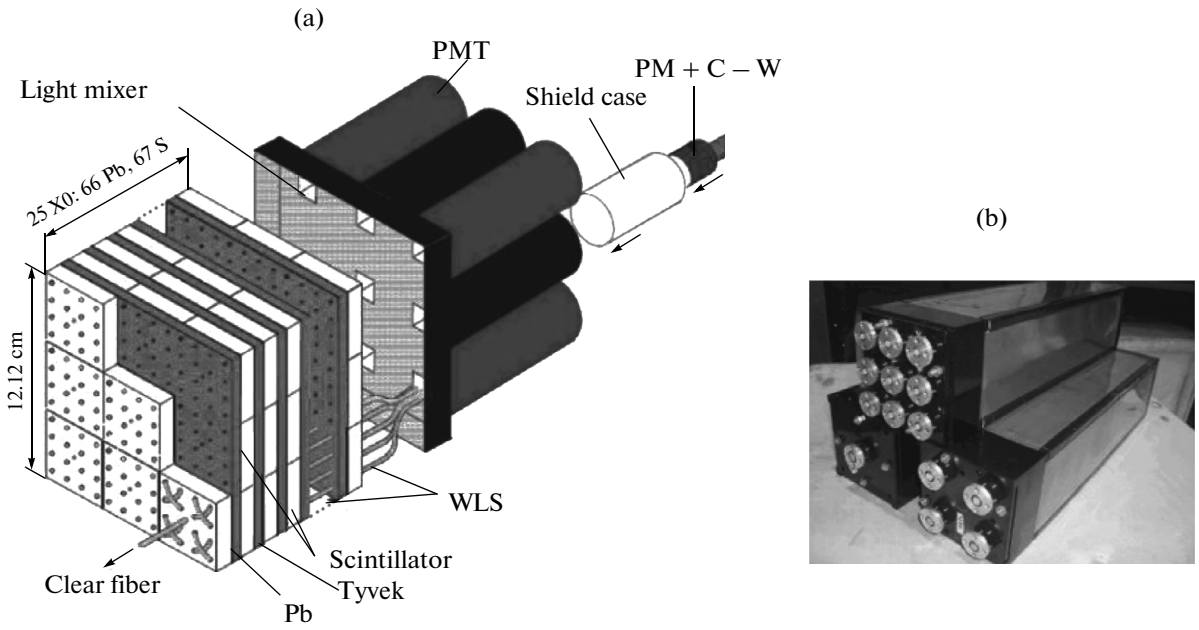

Fig. 32. (a) Schematic view of the LHCb ECAL; (b) three types of the LHCb ECAL modules.

$PbWO_4$ ECAL, where the stochastic term amounts to a few percent, but its cost is considerably higher.

Electromagnetic calorimeter of the KOPIO detector [56]. In the KOPIO detector intended for searching for CP violation in very rare $K_L \to \pi^0\nu\nu$ decay processes, very high requirements were imposed on detection of γ rays (>99.99%) because it was necessary to distinguish those processes from $K_L \to \pi^0\pi^0$ decays. An electromagnetic calorimeter of the shashlik type was used. It consisted of modules that comprised 300 layers of Pb and scintillator tiles with a thickness of 0.275 and 1.5 mm respectively and a cross section of 109.7 × 109.7 mm^2. The total radiation length of the calorimeter was ~$16X_0$. The tiles had 144 holes 1.3 mm in diameter and 9.3 mm distant from each other in which 72 Kuraray Y11(200) multiclad WLS fibers were inserted. Each fiber traversed the module twice, forming a loop (Fig. 33). Signals were collected from both ends of the fiber.

A very good energy resolution

$$\sigma_E/E = (1.96 \pm 0.1)\% \oplus (2.74 \pm 0.05)\%/\sqrt{E\,\text{GeV}}.$$

was obtained for the KOPIO calorimeter by decreasing dead zones, increasing light collection uniformity (light collection nonuniformity <3%), using molded BASF-143E scintillator with 1.5% PTP and 0.44% POPOP, and employing API 630-70-74-510 shower photodiodes (Advanced Photonix Inc.) with a large active area (220 mm^2) and a quantum efficiency of 94%. The time resolution of the calorimeter is described by the formula

$$\sigma_t = (72 \pm 4)\text{ps}/\sqrt{E\,\text{GeV}} \oplus (14 \pm 2)\text{ps}/E\,(\text{GeV}).$$

ALICE electromagnetic calorimeter [57]. The calorimeter is intended for measuring electromagnetic showers produced by electrons and γ rays with momenta up to ~250 GeV/c and serves as an efficient trigger for high-energy showers from e/γ and for γ/π and e/h discrimination. In view of these tasks, severe energy and spatial resolution requirements are imposed on the calorimeter.

The shashlik-type spectrometer used for the ALICE spectrometer was similar to that of the LHCb, except that it operated in a strong magnetic field, which ruled out the use of vacuum PMTs.

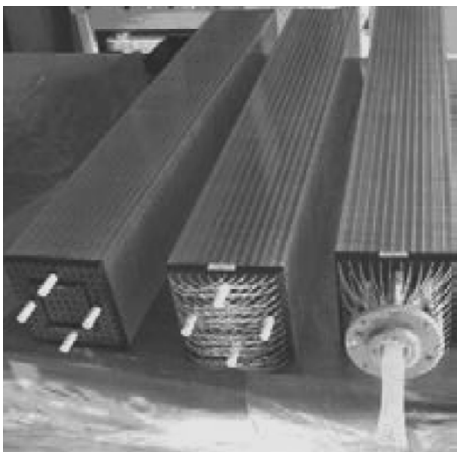

Fig. 33. KOPIO calorimeter modules at different manufacture stages.

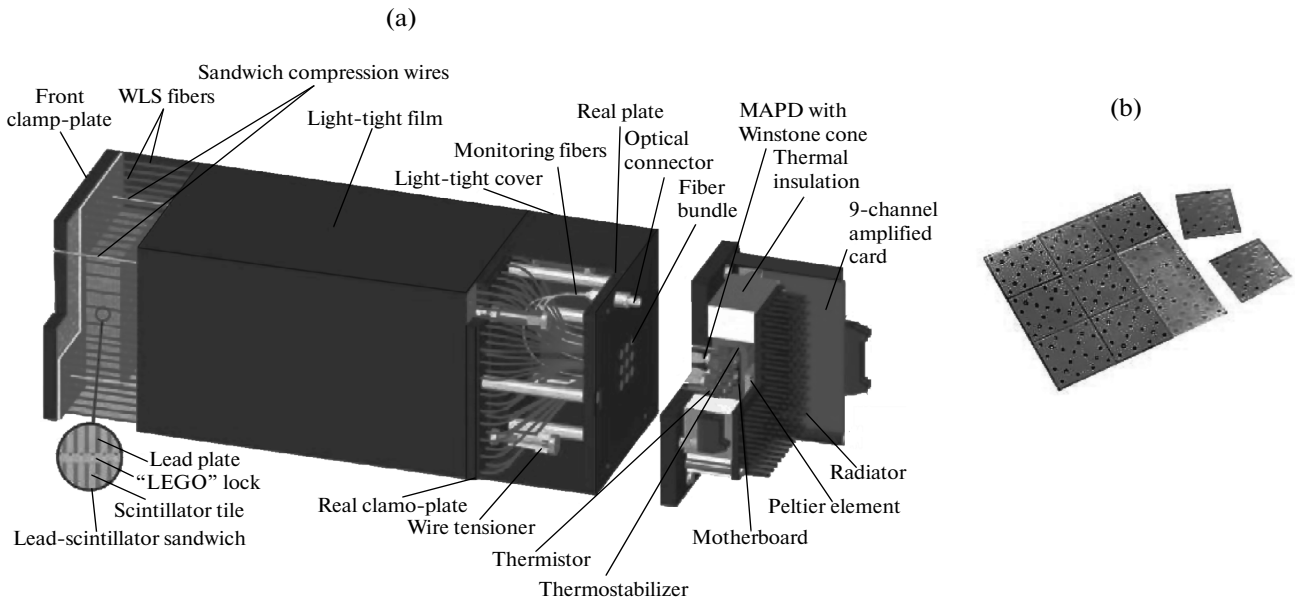

Fig. 34. (a) Design of the shashlik-type calorimeter module; (b) tiles with perforated holes.

The calorimeter was assembled from modules comprising 76 Pb layers 1.44 mm thick and 77 scintillator layers 1.77 mm thick. The total thickness of the module was 24.6 cm ($20.1X_0$, Molière radius 3.2 cm). Each module consists of four independent towers 6×6 cm^2 in size (a total of 12 288 towers), which ensured very high segmentation of the calorimeter ($\Delta\eta\Delta\varphi = 0.014 \times 0.014$) at $\eta = 0$. Light from each tower was collected by 36 Kuraray 1-mm-diameter WLS fibers packed into an array 6.8 mm in diameter and transmitted to the 5×5 mm^2 Hamamatsu APD S8664-55 shower photodiode. About 12000 photodiodes of this type were used in the calorimeter.

To improve light collection, the fiber ends farthest from the photodiode were aluminized while the other ends, assembled into a bundle, were polished and connected to the photodiode through a short light guide/diffuser. Tile surfaces were covered with white paper and the edges were coated with TiO_2, which allowed tiles to be light insulated from each other with an efficiency of higher than 99%.

Beam tests of the prototype at energies up to 100 GeV showed a high response uniformity of <1% for all towers and good response linearity in the energy region. The light output from the APD at the internal gain $M = 30$ was 4.3 photoelectrons/MeV. The energy and spatial resolution of the prototype met the requirements imposed on the calorimeter and were expressed by the formulas

$$\sigma_E/E, \% = (11.1 \pm 0.4)/\sqrt{E\,(\text{GeV})} \oplus (5.1 \pm 0.7)/E \oplus (1.7 \pm 0.3)$$

$$\text{and } \sigma_x, \text{ mm} = 5.3/\sqrt{E\,(\text{GeV})} \oplus 1.5.$$

Electromagnetic calorimeter ECAL0 [58]. Compact highly segmented modules of the electromagnetic calorimeter of the shashlik type were developed at JINR for the COMPASS-II spectrometer. They consist of alternating lead plates and scintillator tiles with perforated holes for setting WLS fibers. The tiles are of molded scintillator based on polystyrene with 2.0% PTP and 0.05% POPOP. The total length of the calorimeter is about $15X_0$. The design of a module is shown in Fig. 34. A module consisted of 109 layers, each comprising a $0.8 \times 119.8 \times 119.8$ mm^3 Pb plate and nine 39.95×39.95 mm^2 scintillator tiles 1.5 mm thick, thus making up nine towers light insulated from each other. Edges of the tiles and surfaces of the Pb plates were painted white to improve uniformity and increase light collection.

Each tile had 16 holes to accommodate WLS fibers for light collection and one more hole for a wire used to tighten up all the tiles. The WLS fibers were BCF-91A fibers 1.2 mm in diameter. The ends of 16 fibers led out from each tower were cut, polished, and arranged into a bundle 6 mm in diameter, and the opposite ends of the fibers were also cut, polished, and mirrored using a special paint.

The selected photodetectors were 3×3 mm^2 MAPD-3N micropixel avalanche photodiodes with a superhigh pixel density of 1.5×10^4 mm^{-2}, wide linearity range, gain of 4×10^4, and photon detection efficiency of about 25% in the blue region. Since the diameter of the fiber bundle is larger than the sensitive area of the photodiode, the Winston cone with a light collection efficiency of about 95% was used for their efficient coupling. The MAPD-3N gain and quantum efficiency strongly depend on temperature. The work-

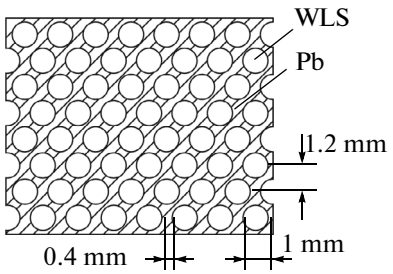

Fig. 35. Schematic view of Pb plates with perforated grooves for laying optical fibers [61].

ing temperature was stabilized at $T = 15°C$ with an accuracy of 0.05°C by the Peltier elements.

The energy resolution obtained in the tests of 3×3 calorimeter modules at e beam line T9 of the PS at CERN is described by the formula $\sigma_E/E\% = 7.8/\sqrt{E} \oplus 2.3$ (tentative result).

Note that similar modules are planned to be used in the electromagnetic calorimeter of the multipurpose detector MPD at the projected heavy-ion collider NICA at JINR [59].

Spaghetti-type lead (tungsten)–fiber calorimeters. Lead–fiber calorimeters are among the fastest, smallest-sized, and radiation hardest electromagnetic calorimeters to be in use since the 1980s [60]. In these calorimeters the passive element is lead plates (foils) with round grooves in which fibers serving as the active element are laid.

Figure 35 shows a set of plates 1.2 mm thick in which round grooves with a radius of 0.45 to 0.5 mm were made for laying WLS fibers [61]. The fibers were epoxied to the plates and the plates were epoxied to each other to make a rigid structure. These plates and fibers were used to assemble the ECAL with dimensions $10 \times 10 \times 30$ cm^3, an absorber-to-fiber volume ratio of 1.17, and an effective radiation length of 1.05 cm. Fibers with the PMMA core and the cladding of fluoroacrylate with FDs in various concentrations were manufactured at the Engineering Center of Polymeric Optical Fibers (Tver, Russia). Their measured attenuation length was about 80 cm.

The prototype was tested in the 5 GeV π^+ beam at the U-70 accelerator of IHEP and X5 at energies 5 to 70 GeV at CERN. The measured energy resolution of the prototype is expressed by the formula

$$\sigma_E/E = (11.23 \pm 0.40)\%/\sqrt{E} \oplus (0.96 \pm 0.08).$$

KLOE detector [62]. The KLOE detector is intended for investigating CP violation in decays of K_0 resulting from the decay $\varphi \to K_L K_S$ in e^+e^- collisions at DAΦNE. The uncertainly in the discrimination between the $\pi^+\pi^-$ and $\pi^0\pi^0$ channels of the K_L and K_S decays must be no higher than 3×10^{-4}.

The detector consisted of an electromagnetic calorimeter ECAL and thin-wall cylindrical drift chambers (diameter 4 m, length 3.3 m) located within the magnetic field of 0.52 T. About 30% of K_L decayed within the chamber volume. The ECAL comprised of Pb plates (foils) and WLS fibers was divided into two sections, barrel and end-cap. The barrel section consisted of 24 trapezoidal modules 4.3 m long and 23 cm thick ($\sim 15X_0$), and the end-cap section consisted of 32 vertical modules 23 cm thick and 0.7 to 3.9 m long. Each module was a stack of 200 lead foils 65 cm wide and 0.5 mm thick with depressions for 1-mm-diameter WLS fibers to be glued into them (Fig. 36).

The SCFI-81 and Pol.Hi.Tech.0046 fibers were selected. The SCFI-81 fibers with their higher light yield, attenuation length, and radiation hardness were used in the inner layers of the calorimeter where the larger part of the shower is contained, and the Pol.Hi.Tech.0046 fibers were used in the outer layers. The foil thickness was maintained to an accuracy of a few μm, and the straightness of the grooves was kept at a level of 0.1 μm over a length of 1 m. A total of 15000 km of fiber and 75 km of foil were used. The ECAL covered 90% of the total solid angle.

The modules were read out using light guides coupled to the fine-mesh Hamamatsu R5946/01 photodetectors using BC-630 optical grease.

The energy and time resolutions of the calorimeter measured with γ rays from the radiative decays of φ mesons were described by the formulas

$$\sigma_E/E = 5.7\%/\sqrt{E} \text{ and } \sigma_t = 54 \text{ ps}/\sqrt{E}) \oplus 140 \text{ ps},$$

where E is in GeV.

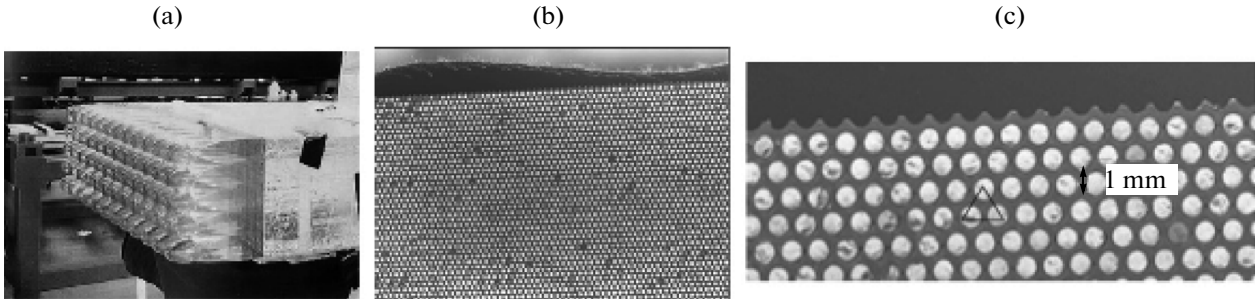

Fig. 36. (a) Photo of the KLOE barrel section module with five rows of 12 light guides each; (b) machined end of the module; (c) lead–fiber matrix [62].

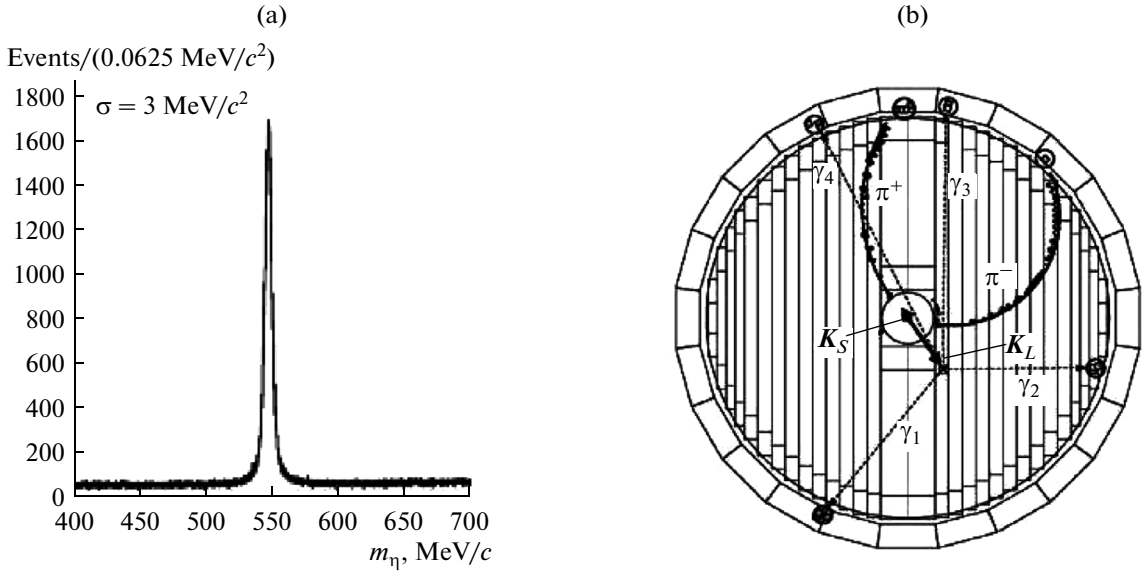

Fig. 37. (a) Effective mass distribution of $\gamma\gamma$ from the $\eta-\varphi\gamma$ decays; (b) schematic view of the decay $\varphi \to K_L K_S$ followed by the decays $K_S \to \pi^+\pi^-$ and $K_L \to 2\pi^0(4\gamma)$.

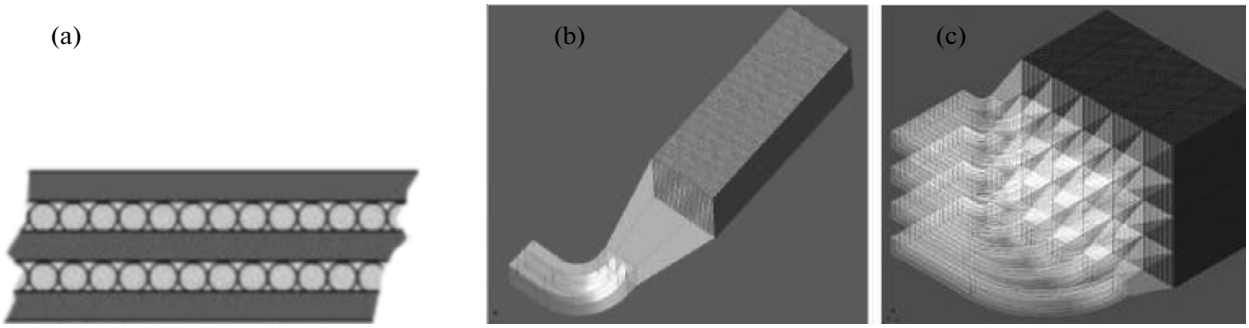

Fig. 38. (a) W plates with WLS fibers; (b) a module with a light guide; (c) an assembly of 20 modules.

The effective mass distribution of $\gamma\gamma$ from the decays $\eta \to \varphi\gamma$ in Fig. 37a has a narrow peak at 547.853 ± 0.024 MeV, which indicates reliable operation of all detector elements. The measured detection efficiency for γ rays with energy >100 MeV was 98% and higher. Figure 38 schematically shows the decay $\varphi \to K_L K_S$ followed by the decays $K_S \to \pi^+\pi^-$ and $K_L \to 2\pi^0(4\gamma)$.

Prototype ECAL for the (g-2) experiment [63]. The prototype tungsten–fiber electromagnetic spectrometer for the (g-2) experiment is quite compact, superdense, and easy to manufacture. It consists of thin W plates and BCF–10 WLS fibers arranged into a ribbon (Fig. 38a). The plate and the ribbon are only 500 μm thick. The plates and the fibers are epoxied together to make a rigid calorimeter module with dimensions $4 \times 4 \times 11$ cm (Fig. 38b).

Twenty modules make up an assembly (Fig. 38c). The calorimeter uses 24 assemblies. Signals from each module are supposed to be read out either by PMTs installed beyond the magnetic field or by silicon PM (SiPM). The calculated radiation length and Molière radius were 0.69 cm and 1.73 cm respectively. The measured value of the stochastic term in the energy resolution was $(11.8 \pm 1.1)\%/\sqrt{E}$ (GeV) in the energy range of 1.5 to 3.5 GeV.

Neutrino Detectors (MINOS, OPERA)

Scintillation counters found wide use in neutrino experiments (MINOS, OPERA, MINERvA, T2K) due to their good optical characteristics, relatively low cost, manufacturability, reliable operation, ability to cover great experimental areas (e.g., 28000 m^2 in MINOS), high segmentation, long-term stability of characteristics, and simple calibration and monitoring procedures.

MINOS detector [11]. The MINOS detector (Main Injector Neutrino Oscillation Search) that consisted of two similar detectors was developed for investigating oscillations of muon neutrinos ν_μ. The smaller

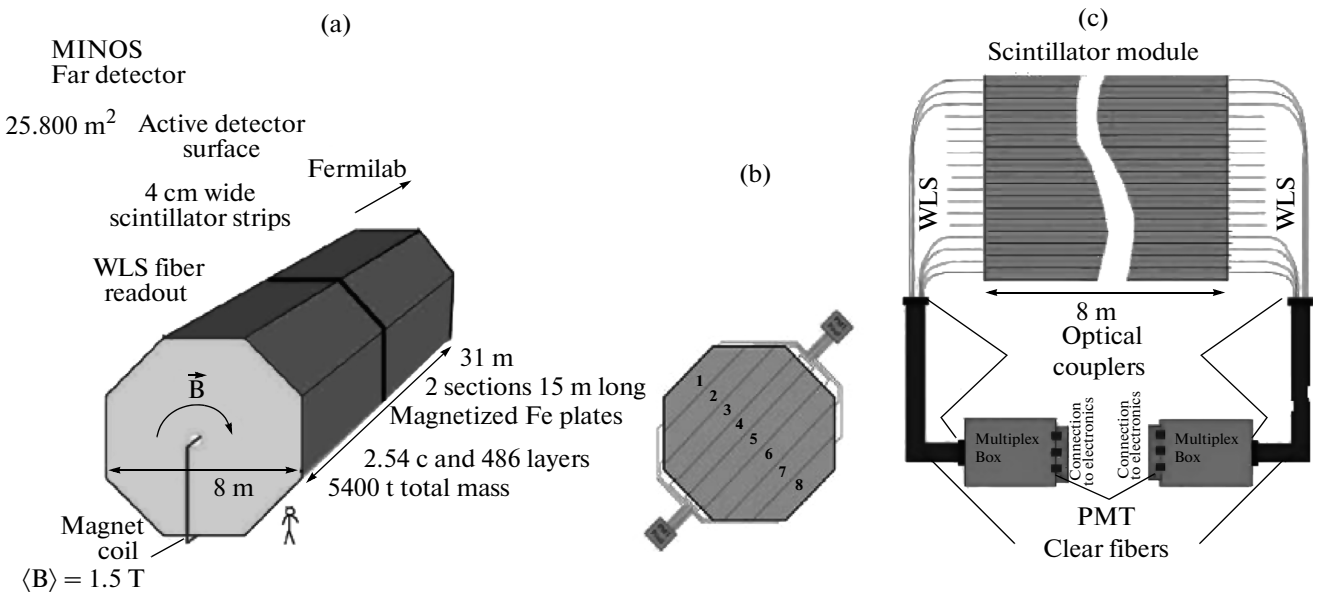

Fig. 39. (a) Schematic view of the MINOS detector; (b) schematic view of a scintillator plane with eight modules; (c) scintillator strip readout scheme.

of the two (near) is located at Fermilab, where neutrinos with an average energy of about 3 GeV were produced in the 120-GeV proton beam, and the larger one (far) is located in the 750-m-deep Soudan mine in Minnesota at a distance of 735 km from the near detector. A comparison of the number, spectra, and energies of the events in both detectors allowed oscillation parameters to be calculated. The detectors are sandwich-type calorimeters consisting of alternating planes of magnetized steel plates 2.54 cm thick and scintillator strips 1 cm thick. In the forward calorimeter section of the detector, each steel plane is followed by a scintillator strip, while in the far spectrometer sections every four steel planes are followed a scintillator strip. The detectors are hexagonal in cross section (Fig. 39a). The overall dimensions of the larger detector are $8 \times 8 \times 31$ m. There is also a third detector located at CERN and used for calibration purposes.

The sandwich version was chosen for the detector after much research. The use of liquid scintillators, Iarocci tubes, and a multigap chamber with resistive plates was investigated [11]. The strip version was preferred for the above-mentioned numerous advantages.

The strips made of polystyrene with 1% PPO and 0.03% POPOP had a rectangular cross section of 1.0×4.1 cm, a length up to 8 m, and grooves for WLS fibers (Fig. 11). Kuraray Y11(175) non-S type polystyrene-based multiclad WLS fibers 1.2 mm in diameter were chosen for their high structural uniformity, transparency, light yield, and large attenuation length. The decisive factor was higher light yield from the farthest end of the strip read out by a 9-m-long WLS fiber and the 3-m-long clear fiber connected to it.

Scintillator strips were assembled into planes of 192 strips grouped into eight modules of 20 strips in modules 4–6 and 28 strips in the rest of the modules (Fig. 39b). Both MINOS detectors had a total of 644 planes and about 105000 scintillator strips. The strips were glued with each other and with one of the Al covers, between which the plane is sandwiched, which ensured quite good rigidity, light insulation, and fire safety of the entire structure.

The planes were arranged vertically, and the strips in the adjacent planes were oriented pairwise orthogonally. Light from the strips was collected by WLS fibers connected through an optical coupler to clear fibers that carried the light to the PMT (Fig. 39c). The clear fibers were used because their attenuation length of 12 m is almost twice as large as that of the WLS fibers [13]. The total number of photoelectrons collected by two PMTs from each strip is characterized by the mean value of about 5.5 (at a required minimum of 4.7 p.e.). The photodetectors were multianode Hamamatsu R5900-00 PMTs with 16 anodes and 4×4 mm^2 pixels for the far detector and 64 anodes and 2×2 mm^2 pixels for the near detector.

The measured energy resolution for the electromagnetic and hadronic showers was $21.4\%/\sqrt{E} \oplus 4\%/\sqrt{E}$ and $56\%/\sqrt{E} \oplus 2\%$, respectively, and the time resolution of the far and near detectors was 2.3 and 5 ns, respectively [13]. The results fully met the design requirements.

OPERA detector [17]. This detector is designed for investigating neutrino oscillations $\nu_\mu \to \nu_\tau$ using the ν_μ beam from CERN. It is located in the Gran Sasso underground laboratory at a distance of 730 km from CERN. The detector consists of two supermodules

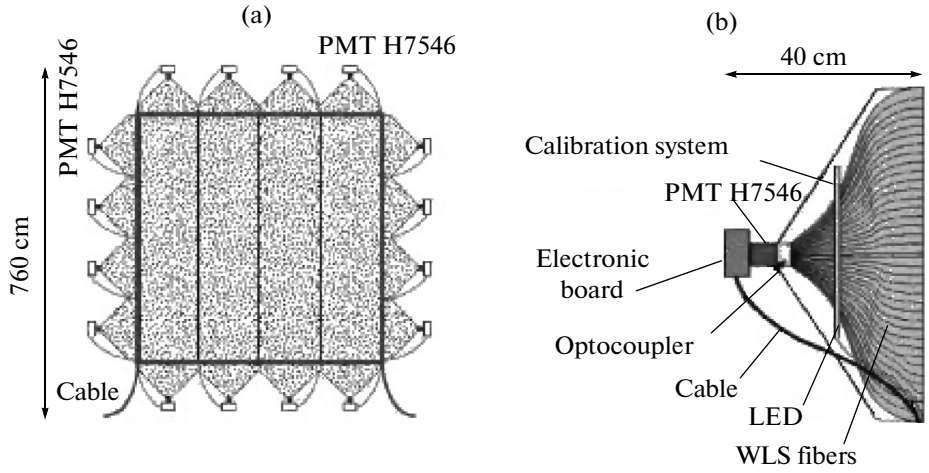

Fig. 40. Schematic view of the scintillator wall with 64-channel H7546 PMTs (a) and connection of the WLS fibers to the 64-channel H7546 PMT (b).

that comprise Pb/emulsion walls, scintillator walls, and a magnetic spectrometer.

Each scintillator wall is made up of two planes of scintillator strips arranged in the transverse geometry (Fig. 40a), which allows 2D (X and Y coordinates) measurements to be performed and the place where the event of interest occurred to be identified. The detector contains a total of 62 scintillator walls, 31 per supermodule. Each plane comprises four 6.7 × 1.66 mm^2 modules consisting of 64 strips 1 × 2.6 × 670 cm^3 in size. The strips of polystyrene with 2% p-terphenyl and 0.02% POPOP were extruded by ISMA [17]. Each strip had a reflective TiO_2 coating and a groove in the middle of the wide side in which Kuraray Y11(175)MJ non-S WLS fibers were glued. Signals from the strips at the blue region wavelengths were read out, reemitted by fiber at green region wavelengths, and transmitted by the fibers to the 64-channel H7546 PMT (Fig. 40b). The LED calibration of the strip signals allowed the condition of all channels to be verified (Fig. 40b).

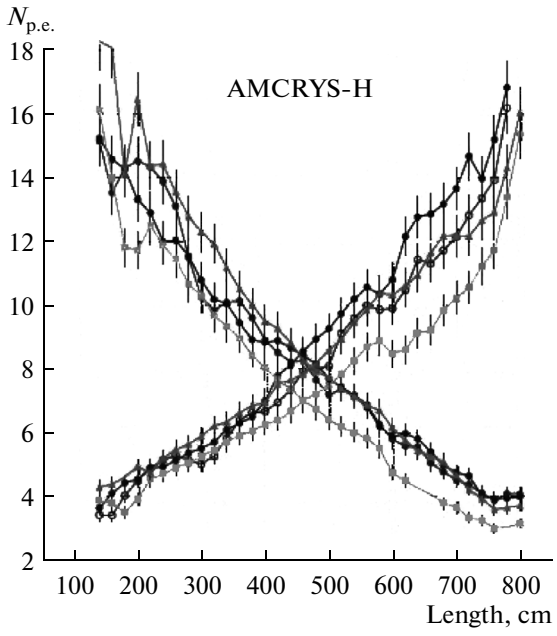

Fig. 41. Light yields from 7-m-long strips.

Signals produced by MIPs in the strips were read out from both ends of the fiber and were as high as ~8 photoelectrons at the center of a strip (Fig. 41). One wall is equipped with 16 H7546 PMTs, and their number in the detector totals 992. Each PMT pixel (2.3 × 2.3 mm^2) is read out independently, and the individual pixel gains range between 3 × 10^5 and 10^6. This large gain spread was corrected using the 32-channel ASIC readout electronics, which allowed equalizing signals from different channels [64].

Space Experiment AMS-02

The AMS-02 spectrometer is intended for investigating the composition and energy spectrum of cosmic particles and searching for antimatter and dark matter [65].

The AMS-02 (Fig. 42) uses a spaghetti-type lead–fiber electromagnetic calorimeter with an active area of 648 × 648 mm^2 and thickness of 166 mm. It consists of nine superlayers, each made of lead plates with grooves in which scintillating fibers 1 mm in diameter were glued with epoxy resin. The arrangement of the fibers in the adjacent layers was mutually orthogonal, which allowed X and Y coordinates of the passing particles to be measured.

To maximize light collection, fibers were connected to the PMT through Plexiglas light guides of truncated pyramid shape. Each light guide was wrapped in an aluminum foil. The light guides were connected to the fibers and PMTs with silicon optical grease. Photodetectors were four-anode Hamamatsu R7600-00-M4 PMTs, totaling 324 for the entire calo-

rimeter. The total thickness of the calorimeter was 17 radiation units [65].

The energy resolution measured in electron and proton beam tests at energies of 6 to 250 GeV at CERN is expressed by the formula

$$\sigma_E/E = (10.4 \pm 0.2)\%/\sqrt{E} \oplus (1.4 \pm 0.1)\%.$$

The AMS-02 spectrometer has a time-of-flight (TOF) system consisting of two upper and two lower scintillator planes spaced 1.2 m apart (Fig. 42). The scintillators were polyvinyl bars read out by fine-mesh R5948 PMTs through Plexiglas light guides. The PMTs had a high gain (10^6), good time characteristics (rise time 1.9 ns, transit time 7.7 ns), and the capability of withstanding the magnetic field of the spectrometer. The system is intended for measuring the time of flight of particles with an accuracy of ~150 ps and also serves as a trigger for discriminating between electrons (positrons) and protons (antiprotons) up to momenta of ~0.5 to 1.5 GeV/c with a proton velocity resolution up to 4% [66].

The use of the combined results of the measurements from the time-of flight system, tracking system located in the magnetic field, and Cherenkov counter allow determination of the mass of the particle that traversed the magnetic spectrometer. The calorimeter is capable of discriminating P from e^+ and antiprotons from e^- at a level of about 10^6.

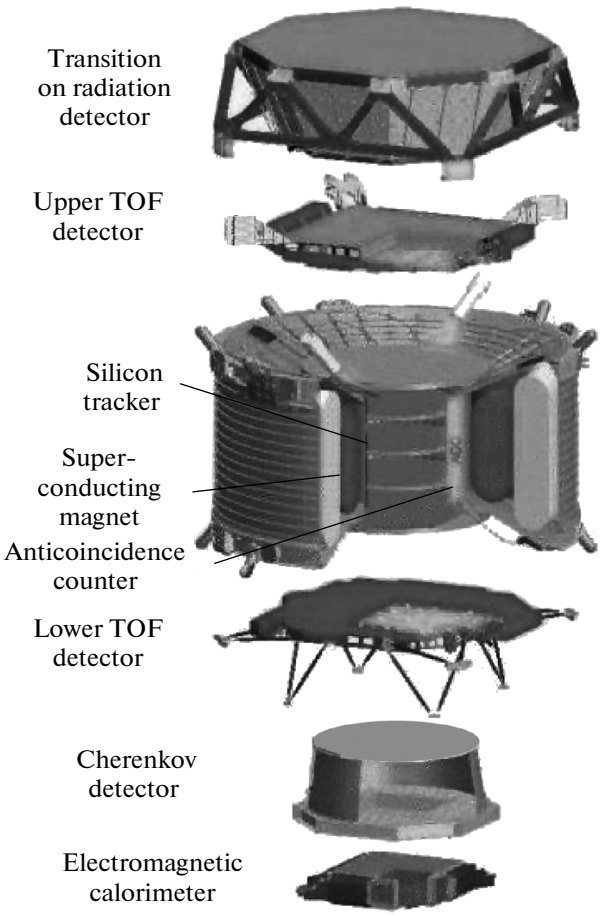

Fig. 42. Schematic view of the AMS-02 spectrometer.

PHOTODETECTORS CURRENTLY USED IN SCINTILLATION COUNTERS IN EXPERIMENTS

A photodetector (PD) is a component of a scintillation counter largely responsible for its most important characteristics, such as light collection, time resolution, energy resolution, and spatial resolution. Further development and use of scintillation counters in current and future experiments will depend to a large extent on the state and improvement of PDs. In this connection, the following requirements are imposed on PDs:

—Higher sensitivity, because light yield of scintillators (long strips and small tiles) can be only few photoelectrons.

—Higher uniformity of light collection and stability of characteristics.

—Compactness (ratio between the useful area of the cathode and its total area).

—Higher pixelization, which is necessary for fiber readout of signals from strips and tiles.

—Better ability to withstand strong magnetic fields and radiation.

—Lower cost and smaller size.

The most widely used PDs are vacuum detectors, like multianode PMTs (MA PMTS) and triodes, and semiconductor detectors, like PIN photodiodes, hybrid avalanche photodiodes (HAPDs), avalanche photodiodes (APDs), limited Geiger mode APDs (G-APDs), and visible light photon counters (VLPCs).

Multianode PMTs and Triodes

Multianode PMTs are widely used in modern scintillation counters due to their high gain (10^6–10^7), high resolution detection of single photons, and possible segmentation of their anodes. They are vacuum photodetectors, usually with a bialkali photocathode and a metal body and dynodes. The number of amplification cascades can be as large as ten and more. Their quantum efficiency in the visible light region is no higher than ~25%. Disadvantages of MA PMTs are high voltage of power supply and inability to operate in magnetic fields without special antimagnetic shielding. Another factor to be taken into account is compactness. For example, in previous MA PMT versions the active area was about 40%. In modern flat-panel PMTs like H8500 or H9500, it is as large as 89% [67, 68]. The use of lenses can also make PMTs more compact.

The R7877 PMTs were used in the ATLAS calorimeters, R7600 in the ALFA detector of ATLAS in

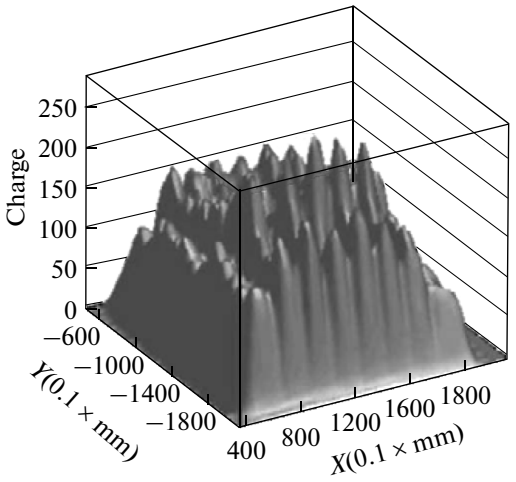

Fig. 43. Gain variations for the pixels of the 64-channel H7546 PMT.

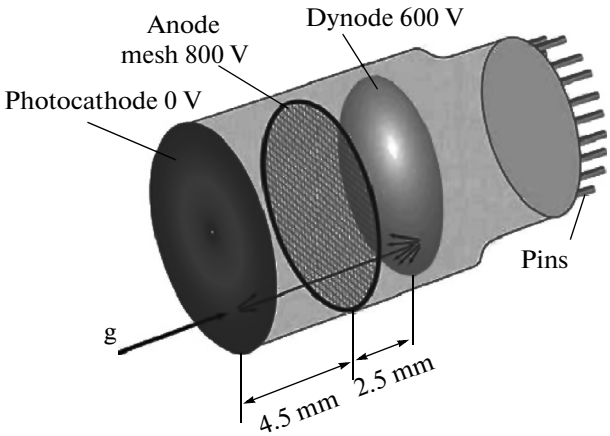

Fig. 44. Structure of a vacuum triode [69].

AMS-02, R5900-16(64) in MINOS and R5900-16 in the CDF-II preshower detector, R7546-64 in OPERA, and R7899-20 in LHCb ECAL.

Characteristics of MA PMTs can be demonstrated with Hamamatsu R5900 as a typical example: the number of channels up to 8×8, dimensions 28×28 mm^2, active area 18×18 mm^2 (41%), bialkali cathode QE = 20% at 400 nm, and gain ~10^6. Problems are sensitivity to magnetic fields, gain uniformity, and channel-to-channel crosstalk.

Gain of MA PMT pixels can vary. For example, in the 12-dynode H7546 PMT (improved version of R5900) with 2.3×2.3 mm^2 pixels the gain variations were as large as a factor of 3 (Fig. 43). However, this large difference was compensated for at a level of <1% by an adjustable preamplifier [64].

Vacuum triodes are single-cascade PMTs with a bialkali cathode, quantum efficiency of ~20% at $\lambda =$ 425 nm, and outer diameter of 25 mm. The window is made of radiation-hard ultraviolet glass, and the anode is a fine (10 μm) copper mesh (Fig. 44) [69]. They were developed and manufactured at the National Research Institute "Elektron" (St. Petersburg, Russia) and used in the CMS end-cap ECAL. Unlike avalanche diodes used in the ECAL barrel section, they proved to be radiation harder (5 kGy/yr); in addition, their gain dependence on the magnetic field (B) had a plateau in the interval $B = 3$–4 T, their cost was lower, and the their operating voltage was <1000 V.

PIN Photodiodes and Hybrid Avalanche Photodiodes

The use of semiconductor PDs in particle physics experiments began with PIN photodiodes, simple and reliable devices that found wide use in experiments in the 1980–1990s. For example, Hamamatsu S2662 PIN photodiodes were used to read out BGO crystals of the calorimeter in the L3 experiment [70]. They were remarkably suitable for that task because they had high quantum efficiency (67%) at $\lambda = 480$ nm, the peak value of the BGO crystal emission spectrum, while the light yield of BGO was as high as 8000 photons/MeV.

However, PIN diodes do not have internal amplification and thus a charge-sensitive amplifier is needed for obtaining light signals from them. Since noise pulses are about 200 electrons, the minimum detectable light flux should be more than a few hundred photons. Also, PIN diodes require high temperature stabilization (−1.55%/°C).

Hybrid avalanche photodiodes (HAPDs). HAPDs combine advantages of vacuum PDs (high sensitivity) and semiconductor PDs (high spatial and energy resolution, insensitivity to magnetic field). In addition, they are simple to manufacture because they do not use dynodes while a photodiode is easily segmented.

The operation and design of an HAPD are schematically shown in Fig. 45a [71]. Under the effect of a high electric field (about 10 kV), a photoelectron knocked out of the photocathode produces about 10^3 electron–hole pairs in the photodiode (APD), and the shower that develops inside the APD increases the number of those pairs by a factor of 50 to 200. However, an increase by a factor of 100 and more requires a high temperature and voltage stabilization. At a gain of 1000, a change in temperature by 1°C leads to a decrease in gain by 15%, and a change in voltage by 1 V leads to an even greater decrease in gain by 30% [72]. Development of the avalanche is maintained first of all by electrons, because multiplication of holes would require higher fields. The total gain ultimately amounts to ~10^4. Further increase in gain is limited by the occurrence of breakdowns.

HAPDs efficiently detect single photons as is evident from the single photon distribution in Fig. 45b.

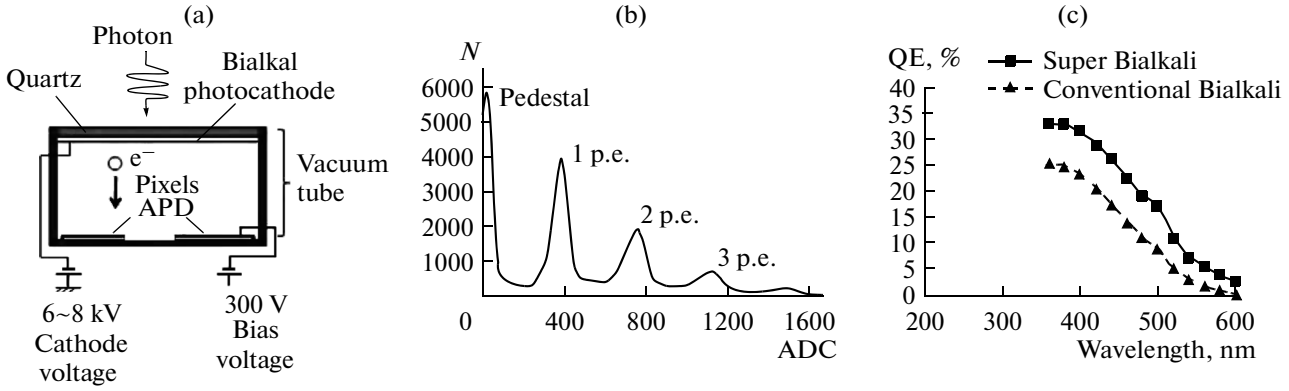

Fig. 45. (a) Design of an HAPD; (b) distribution of single photons; (c) quantum efficiency QE of bialkali photocathodes as a function of the wavelength.

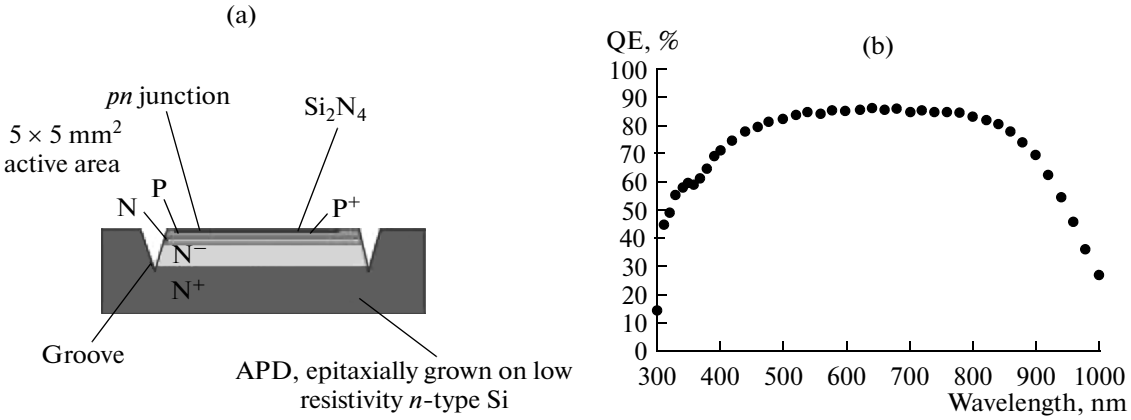

Fig. 46. (a) Structure of the Hamamatsu S8141 avalanche photodiode for the CMS ECAL; (b) quantum efficiency (QE) of the photodiode as a function of the wavelength.

Discrimination of peaks up to three photons is clearly seen. HAPDs use Super Bialkali (SBA) photocathodes with quantum efficiency (QE) as high as 32% at the wavelength 380 nm (Fig. 45c). With a GaAsP photocathode, the QE increases to 40% in the wavelength range of 400 to 600 nm [71].

A point to remember is that backscattering of photons and electrons occurs in the HAPD with a probability of about 20% and deteriorates the position resolution. In an electric field of about 10 kV with no magnetic field, the coordinate spread is about 40 mm. However, in a longitudinal magnetic field of ~1.5 T, the spread decreases to 5 mm due to the Larmor process [71]. In the HAPD used in the CMS HCAL under ~4 T this effect is even stronger. Another negative point is surface currents which are eliminated by making grooves on the photodiode face.

HAPDs were first used in a large number at the CMS HCAL. Signals from all 17 tiles of each HCAL tower are read by WLS fibers connected to clear fibers. These fibers arranged into a bundle 4.8 mm in diameter are coupled to the HAPD consisting of 19 hexagonal pixels (2 mm^2 each) and make up one of 10000 readout channels.

HAPDs are PDs with proximity focusing of electrons accelerated in a strong electric field (~10 kV) in a narrow gap (3.35 mm) along the magnetic field lines [72].

Avalanche photodiodes (APDs). APDs, like HAPDs, have internal amplification (50 to 200), and their quantum efficiency is higher than 70% in the visible region. They are insensitive to the magnetic field, and their gain is no higher than 10^4 due to breakdowns. APDs are capable of detecting low light fluxes: 20 photons are sufficient to trigger them. The APD output is proportional to the intensity of the incident light.

Figure 46a shows the structure of the Hamamatsu S8141 avalanche photodiode used in the CMS ECAL [73]. It is a reverse-type photodiode made by epitaxial growth on low resistivity n-type silicon followed by ion implantation and diffuse steps to produce a high resistivity p–n junction near the outer surface. A very high field of ~2×10^5 V/cm is generated in this junction, where an electron–hole avalanche is initiated. The upper p layer is only 7 μm thick in order to decrease

Table 8. Characteristics of APDs used in the CMS ECAL, KOPI, and ALICE. The last two rows present relative variations in the gain M as a function of the voltage and temperature variation (in percent)

APD characteristics	CMS	KOPIO	ALICE
Active area, mm^2	5×5	200	100
Capacitance, pf	75	130	270
Series resistance, Ω	3	15	<5
Dark current, nA	<10	~50	~3
Quantum efficiency, % at λ, nm	70% 420	94 500	80 476
$dM/dU \times 1/M$, %/U	3	1.4	3
$dM/dT \times 1/M$, %/°C	−2.2	−3	−4.5

the ionizing radiation effect, and grooves 30 μm deep and wide help to reduce surface currents. An antireflective Si_2N_4 coating is applied to the p layer.

The quantum efficiency of the S8141 photodiode at the peak wavelength of the $PbWO_4$ crystal radiation $\lambda = 420$ nm is ~70%, and in the wavelength range of 500 to 850 nm it is more than 80% (Fig. 46b) [73].

Table 8 presents the main characteristics of the Hamamatsu S8141 APDs used in the CMS [73] and, for comparison, of the Advanced Photonics Inc. APD 630-70-74-510 used in KOPIO [56] and Hamamatsu S8664-1010N APD, a version of which was used in ALICE [57].

Limited Geiger Mode Avalanche Photodiodes (G-APDs)

G-APDs were first created in Russia in the 1990s [74, 75] and further developed in [76, 79–86]. Now they are manufactured by CPTA and MEPhI/Pulsar (Moscow, Russia), Hamamatsu (Japan), Zecotek (Singapore, Canada), JINR (Dubna, Russia), FBK-irst (ASD) (Trento, Italy), SPM (Sensl) (Cork, Ireland), KETEK (Munich, Germany), ST Microelectronics (Catania, Italy), and others.

A G-APD is a matrix of a lot of independent APDs (pixels) with a size of 30×30 (50×50) μm^2 connected by a common bus to which a bias voltage 10 to 15% higher than the breakdown voltage is applied. When a photon hits a pixel, an avalanche develops in the pixel due to impact ionization in the high electric field of the p–n junction initiated not only by electrons but also, unlike the case in APDs, by holes and secondary photons. An analogue signal appears at the pixel output; if several pixels are fired, their charges are summed. G-APDs from different manufacturers differ in structure, avalanche quenching methods, active area size, number and size of pixels, operation mode, and characteristics. Figure 47 shows pixel structures in two G-APDs, an MRS (metal–resistor–semiconductor) [74], and an MAPD-3N (micropixel avalanche photodiode with double n–p–n–p junctions) [84], which employ different avalanche quenching methods.

The MAPD-3N is a micropixel photodiode with superhigh density of pixels (~4×10^4 mm^{-2}) on an n-type Si substrate on which two epitaxial p-type layers are grown and highly doped pixels of n^+ type conductivity are embedded with a spacing of 5 to 15 μm (Fig. 47b).

Development of an avalanche in the G-APD is stopped automatically when the p–n junction voltage drops below the breakdown voltage due to the quenching resistor (<1 MΩ) that is part of each pixel or due to directly biased p–n junctions occurring under each micropixel (Fig. 47b). The pixel recovery time ranges from a few tens of nanoseconds to a few microseconds.

Since G-APDs are highly sensitive to single photons and have a gain of 10^6 to 10^7 comparable with that of PMTs, they are often called silicon photomultipliers (SiPMs). They are unaffected by the magnetic field

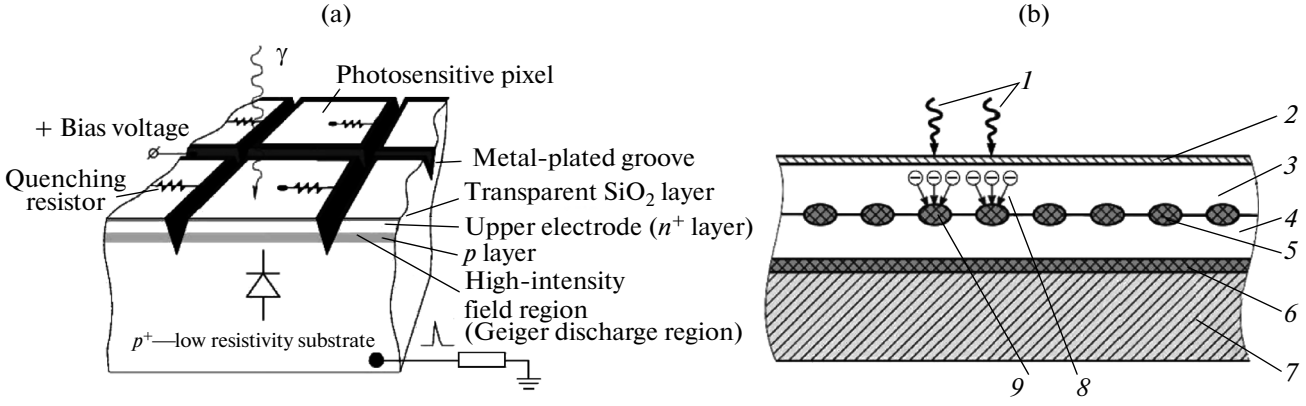

Fig. 47. (a) MRS structure; (b) MAPD-3N structure: (*1*) photons, (*2*) highly doped p^+ layer, (*3*) second epitaxial p^+ layer, (*4*) first epitaxial p^+ layer, (*5*) n^+ regions (micropixels), (*6*) highly doped n^+ layer, (*7*) n-type Si wafer, (*8*) avalanche region, (*9*) charge accumulated in the potential well form the n^+ region.

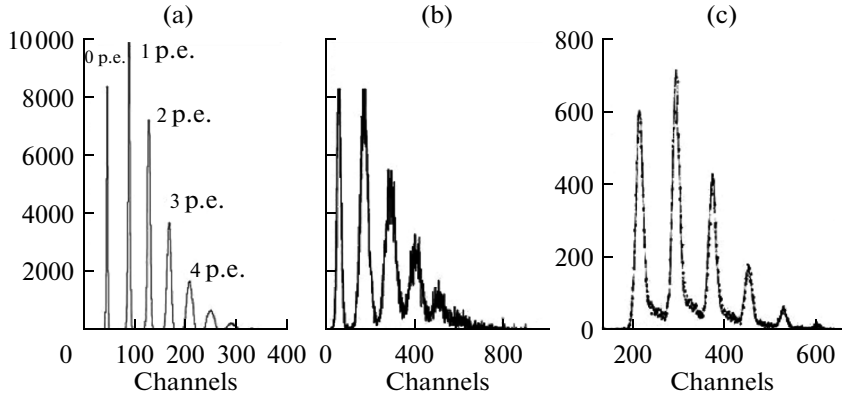

Fig. 48. Distributions of single-photon spectra obtained with a G-APD [76] (a), VLPC [77] (b), and HAPD [78] (c).

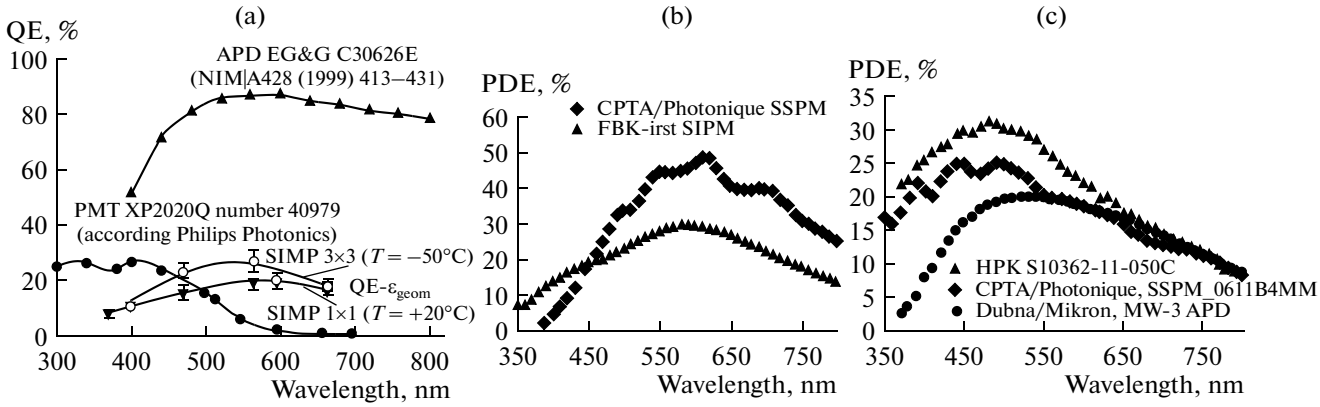

Fig. 49. (a) Comparison of the G-APD, APD, and PMT photon detection efficiencies [79]; (b) PDE as a function of the wavelength for the G-APDs from CPTA ($U = 42$ V) and FBK-irst ($U = 35.5$ V) used for the blue/green region [80]; (c) PDE as a function of the wavelength for the *n*-type G-APDs from Hamamtsu ($U = 70.3$ V, triangles), CPTA/Photonique ($U = 36$ V, diamonds), and Dubna/Mikron ($U = 119.6$ V, circles) [80].

(7 T and higher), have low power consumption (<50 μW/mm^2) and low bias voltage (<70 V), and are compact and reliable. Unlike APDs, where avalanche development fluctuates, G-APDs are characterized by uniform pixel-to-pixel gain and low electronic noise.

Figure 48 shows distributions of single-photon spectra obtained at the G-APD (a) [76], VLPC (b) [77], and HAPD (c) [78]. The distributions from the G-APD and APD are obtained at room temperature and from the VLPC at 6.5 K. Among these PDs, the G-APD is seen to have the highest resolving power for single photons.

One of the main G-APD characteristics is the photon detection efficiency (PDE), defined as a product of the p–n junction quantum efficiency QE, probability for a photoelectron to initiate the Geiger discharge QEg, and the geometrical efficiency ε (the fraction of the sensitive area of the APD in its total area). The PDE of the G-APD is much lower than the APD QE because of its low geometrical efficiency, which was about 25% in earlier G-APD versions. The QEg depends on many parameters like bias voltage (U), overvoltage, photon wavelength, temperature, and the nature of charge carriers (electrons or holes). Nevertheless, the PDE is higher than the QE of vacuum PMTs in the visible wavelength region ($\lambda > 450$ nm), which is of great interest for scintillator + WLS fiber systems (Fig. 49a) [79].

The PDE of the p-type CPTA (43 μm pixels) and FBK-irst (50 μm pixels) G-APDs with an area of 1 mm^2 and sensitivity to the blue/green region was measured at the maximum bias voltage U and room temperature and found to be 50% and 30% respectively at a wavelength of 600 nm (Fig. 49b) [80]. The geometrical factors also increased to 70% and 50% respectively.

The PDE of the *n*-type CPTA UV-sensitive G-APD with the p^+ layer <100 nm thick was measured to be as high as 25% at $\lambda = 450$–550 nm, $U = 36$ V, and room temperature (Fig. 49c). For comparison, Fig. 49c also shows the PDE measured for the n-type

Table 9. ΔT and ΔU needed to change the gain by 1%

Photodetector	ΔT, °C	$\Delta U/U$
APD EG G C30626 ($M = 100$)	0.1	0.4 V/400 V = 10^{-3}
APD Hamamatsu S5345	0.30	0.04 V/300 V = 10^{-4}
GAPD ($N = 2 \times 10^6$)	2.5	0.05 V/50 V = 10^{-3}

HPK SSPM_0611B4MM and Dubna/Mikron MW-3 APD.

Compared with APDs, G-APDs are less dependent on variations in temperature T and bias voltage U (Table 9) [76].

The problem points for G-APDs are optical crosstalk, dark current, afterpulsing, recovery time, small size, increase in photon detection efficiency, and extension of the dynamic region. In the past years extensive investigations have been carried out to solve these problems.

To decrease the effect of the optical crosstalk—which is due to the fact that some avalanche photons (1 per ~10^5 electrons) escape from a fired pixel to the neighboring ones—grooves extended to the p-region are made on the external surfaces of the pixels. The grooves decrease optical crosstalk to 1–3%. The width of grooves is about half their depth (Fig 47a) [27]. To reduce absorption of photons in external layers, these layers are made very thin. For example, in an $n(p)$-type G-APD the external layer is fractions of a micrometer (few μm) thick, and antireflective Si_2N_4 coating is applied to decrease back reflection.

The dark current is the main source of noise in a G-APD and results from random thermally generated free charge carriers capable of initiating Geiger discharge, which undesirably affects the gain. The dark current strongly depends on temperature and amounts to 1–2 MHz/mm^2 at room temperature and ~200 Hz/mm^2 at $T = 100$ K [79]. The gain is also increased by afterpulsing, which is due to the fact that some free avalanche carriers are trapped in the structure detects and released with a delay as long as a few μs [80] can initiate Geiger discharge. The dark current also depends to a large extent on the purity of the material used to manufacture G-APDs.

A small size of the APD and a small number of its pixels result in the loss of response proportionality in multielectron events due to saturation of output signals (Fig. 50a). A wide photoresponse linearity range at almost 100% geometrical efficiency was obtained in the MAPD-3N with its superhigh pixel density of $(1–4) \times 10^4$ mm^{-2}. As it is seen, the photoresponse amplitude A remains linear up to 6×10^6 photons per pulse (Fig. 50b) [84].

Most currently manufactured G-APDs have a size of 1×1 mm^2 and 3×3 mm^2. There are also low-volume manufactured pilot G-APDs with a size of 4×4 mm^2 (FBK–AdvancedSid), 5×5 mm^2 (MEPhI/Pulsar) and 6×6 mm^2 (Hamamatsu). Increasing the size to 100 mm^2 leads to high power dissipation of about 10 mW, which can increase the temperature by ~10°C and accordingly decrease the gain by a factor of 1.5–2, enhance optical crosstalk, and increase the afterpulsing and the noise pulse rate (10^5–10^6) mm^{-2} [81].

Visible Light Photon Counters (VLPCs)

Visible light photon counters are silicon shower PDs based on the impurity conduction, the width of which under the conduction band is only 50 mV. They have quantum efficiency in the visible region of the spectrum as high as ≥75% (Fig. 51), gain of $(2.2–6.4) \times 10^4$, and the ability to discriminate single photons with a

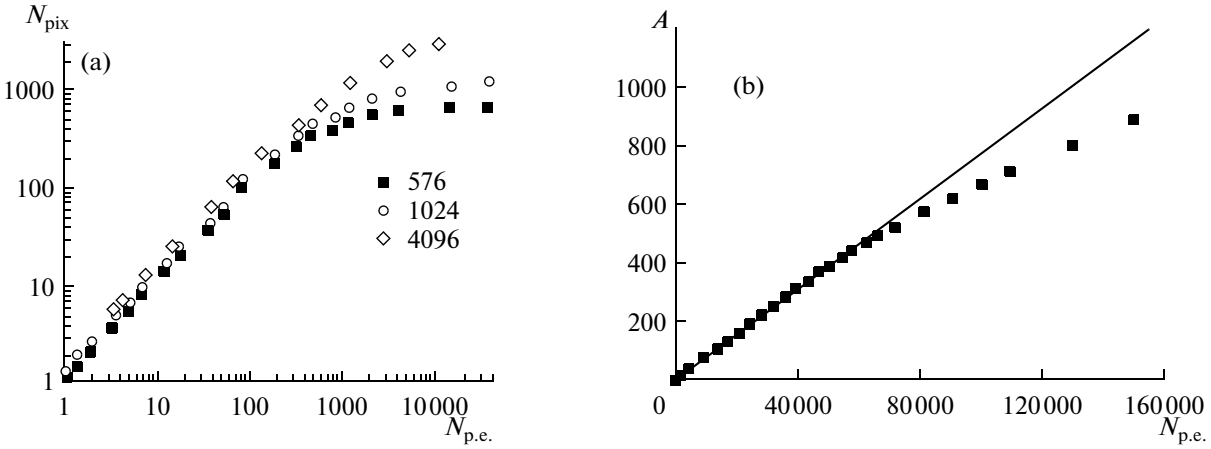

Fig. 50. (a) Response function (dependence of the number of fired pixels on the number of photoelectrons) of MEPhI/Pulsar SiPMs with a different number of pixels; (b) dependence of the MAPD-3N photoresponse amplitude A on the number of photons N. Squares are experimental data, and the straight line is the linear extrapolation.

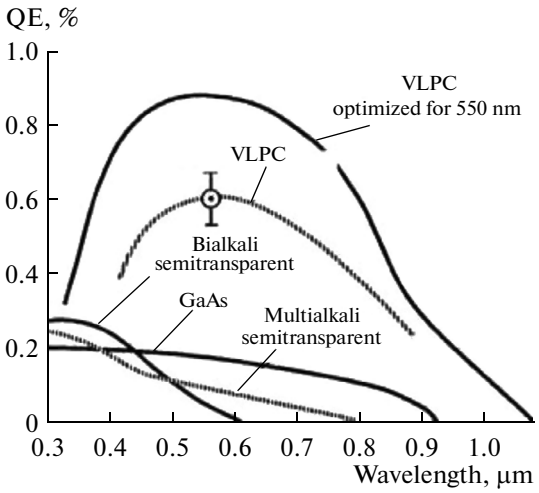

Fig. 51. Quantum efficiency QE of VLPCs, and bialkali, multialkali, and GaAs photocathodes (Ruchti [1]).

high resolution (Fig. 40c). VLPCs operate at a temperature of 9 K and bias voltage of 6 to 8 V, their dark noise is at a level of $<5 \times 10^4$ Hz, they are weakly sensitive to the magnetic field, and are capable of working in a harsh radiation environment [77]. Highly stable temperature and bias voltage are an important condition for their operation. The dark current increases by a factor of 4 when temperature increases by 1 K. The quantum efficiency and the gain also depend on the temperature though to a lesser degree. The stability of the temperature and bias voltage are maintained at a level of ±0.05 K and ±30 mV respectively.

About 86000 VLPCs successfully operated in the D0 spectrometer.

Comparative characteristics of different photodetectors widely used in high-energy physics experiments are given in Appendix C.

Prospects for Silicon Photodetectors

Further development and use of scintillation counters in current and future particle physics experiments at the ILC, GSI, and NICA is impossible without improving photodetectors, the most promising of which are limited Geiger mode silicon avalanche photodetectors (SiPMs). Over the past years, extensive investigations have been carried out with a view to increasing their photon detection efficiency and size, reducing noise pulse rate and pixel-to-pixel optical crosstalk, decreasing temperature dependence of the gain, etc. These investigations are mainly performed with small prototypes.

MEPhI group, in cooperation with the Exelites Company, developed 1 × 1 and 3 × 3 mm^2 n-type SiPMs with 50 × 50 μm^2 (50 V) and 100 × 100 μm^2 (100 V) pixels respectively. They were tested with a weak source of light, their optical crosstalk (CT) probability and excess noise factor (ENF) were measured as a function of overvoltage ΔU (Figs. 52a, 52b) and compared with similar distributions measured under identical conditions for the Hamamatsu 3 × 3 mm^2 MPPC S 10362-33-100C N354 and 1 × 1 mm^2 MPPC S 10362-33-100U N50 [82].

It is seen that the MEPhI detectors have remarkable characteristics concerning both optical cross talk and excess noise factor, which are currently record low. At $\Delta U = 4$ V their CT and ENF are no higher than 3 to 5% and 1.02 respectively, while the Hamamatsu detectors show 38 to 40% and 1.3 to 1.55 at $\Delta U = 1.6$ V.

No less remarkable are other features of the MEPhI SiPMs: photon detection efficiency in the near ultraviolet/blue region ~50–60%, time resolution ~200 ps (3 × 3 mm^2 detector), dark current 80 kHz at room temperature, and extremely low temperature dependence 0.5%/°C.

A special scintillation detector START [83] was developed for cosmic muon triggers in the TOF system

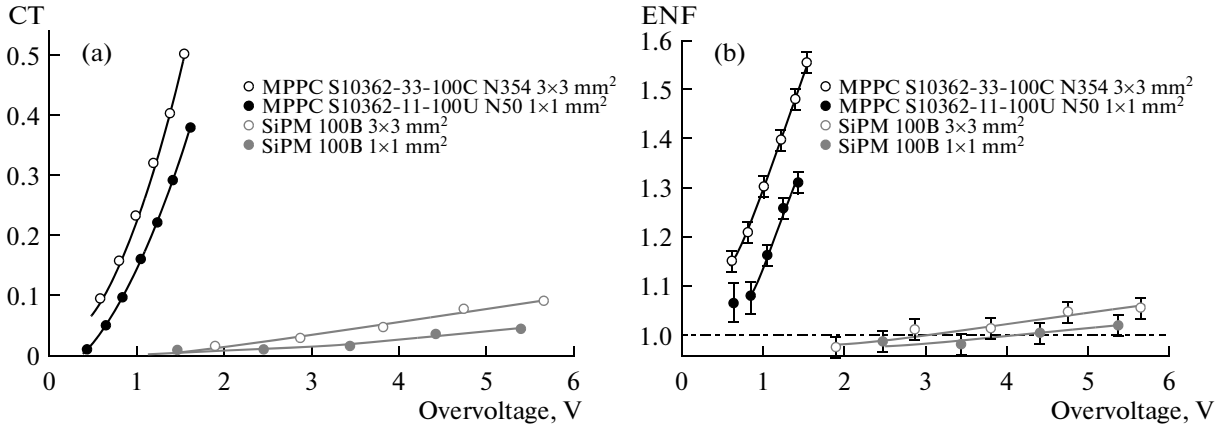

Fig. 52. Overvoltage dependence of the optical crosstalk CT (a) and excess noise factor ENF (b).

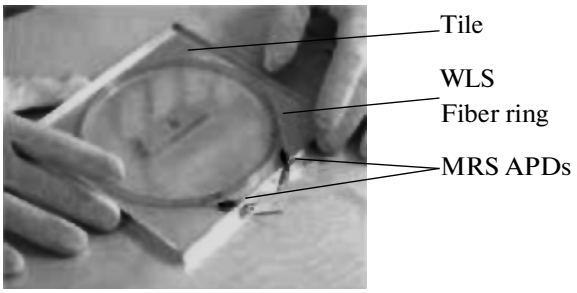

Fig. 53. START detector: a scintillator tile, WLS fibers, and two MRS APDs put together [82].

of the ALICE spectrometer. It consisted of a $150 \times 150 \times 10$ mm^3 BC-412 scintillator plate, two Kuraray Y11 1-mm-diameter WLS fibers, and two G-APDs with the MRS (metal–resistor–semiconductor) structure. Two or three fiber coils were laid into a deep circular groove made as close to the tile edges as possible. One end of the fiber was coated with a reflective material, and the other end was pressed to the MRS (Fig. 53). The achieved time resolution was ~1.2 ns.

An important feature and advantage of using MRS in START was that the PDs were mounted directly on the plate, which considerably simplified construction of larger-scale trigger systems. In addition, they were connected in coincidence, which decreased noise pulse rate by several orders of magnitude at a gate width of 20 to 80 ns.

A lot of SiPMs are supposed to be used in the prototype of the hadronic calorimeter for the CALICE detector of the ILC [86]. It is a 38-layer sandwich calorimeter consisting of 7620 steel plates and scintillator tiles with a thickness of 1.6 cm and 0.5 cm, respectively. The area of each layer is 1×1 m^2.

The requirements imposed on the ILC detectors are very stringent. Particles will be identified using a new method, PFA (Particle Flow Algorithms), which involves individual identification of all shower particles, both neutral and charged, with an energy resolution not worse than $30\%/\sqrt{E}$. This requires high segmentation of the calorimeter. Monte Carlo calculations show that the optimum size of the tiles in the highest-intensity parts should be on the order of 3×3 cm^2 and smaller. The chosen tile sizes are 3×3 cm^2 for the central section of the calorimeter (30 layers), 6×6 cm^2 for the intermediate section, and 12×12 cm^2 for the outer section (8 layers) (Fig. 54a).

Tiles will be read by Kuraray 1-mm-diameter WLS fibers laid in the grooves 2 mm deep, which occupy a quarter of a circle in the smallest tiles and a full circle in the rest of the tiles. One fiber end was mirrored and the other end was connected to the PMT through an air gap. Signals from the WLS fibers will be read by more than 10000 MEPhI/Pulsar 1.1×1.1 mm^2 PMTs. The number of pixels is 1156, and their size is 32×32 μm^2. The gain at a bias voltage of 50 V is ~10^6 [86].

A prototype of the hadronic calorimeter for the CALICE detector was also developed. In this calorimeter tiles ($3 \times 3 \times 0.3$ cm^3) were read through WLS fibers by CPTA/Photonique silicon PMTs (796 pixels) [87]. Figure 55a shows one of the tiles with a groove for the WLS fiber with one end mirrored and the other connected to the SiPM, and at the bottom of figure there is a module of the prototype consisting of 36×36 tiles mounted at the back side of the readout electronics, which is a 36-channel ASIC system. The minimum ionizing particle detection efficiency is 95%.

To choose the optimum tile, another light collection method was tested, in which the tile is directly coupled to the SiPM (Kuraray MPPC25-P mounted in a special depression) without a WLS fiber (Fig. 55b, left). This light collection method resulted in high uniform signal collection from the tile surface (Fig. 55b, right) [87].

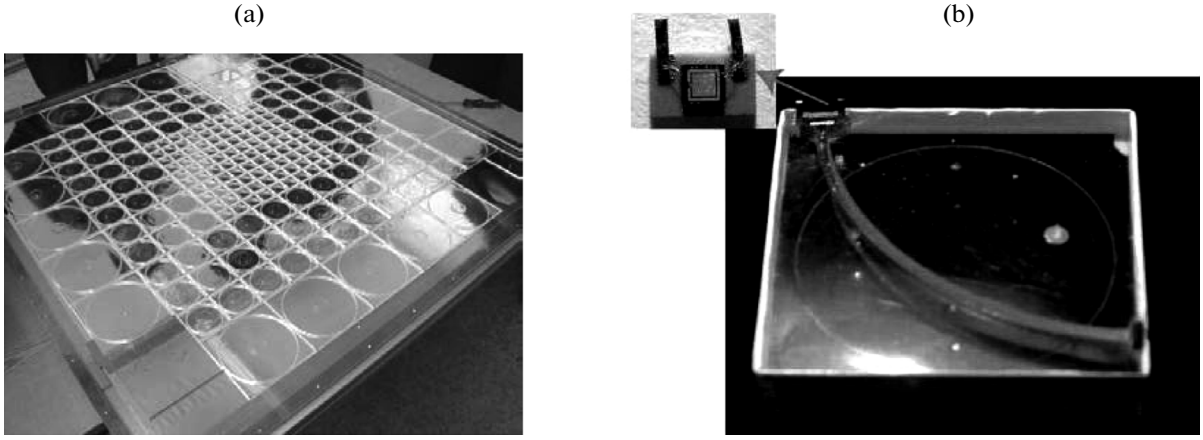

Fig. 54. (a) One of the layers (planes) of the CALICE HCAL; (b) a 3×3 cm^2 tile with the built-in MRS [86].

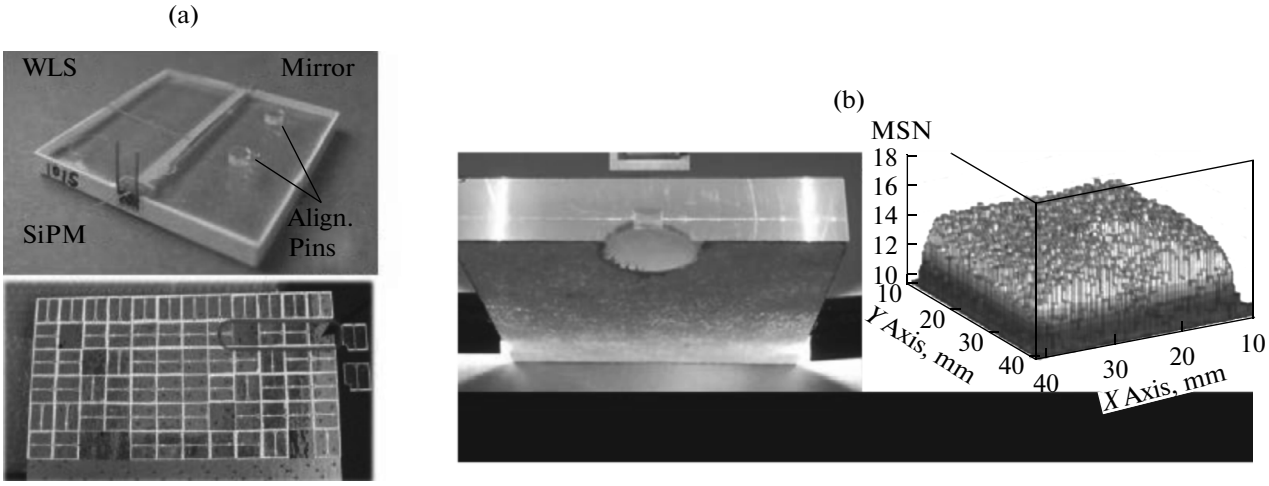

Fig. 55. (a) Single calorimeter tile (top) and a calorimeter module comprising 36 × 36 tiles mounted on the back side of the readout electronics (bottom); (b) a single tile with a special depression for mounting the Kuraray MPPC25-P (left) and the distribution of the signal amplitudes measured over the tile surface (right) [87].

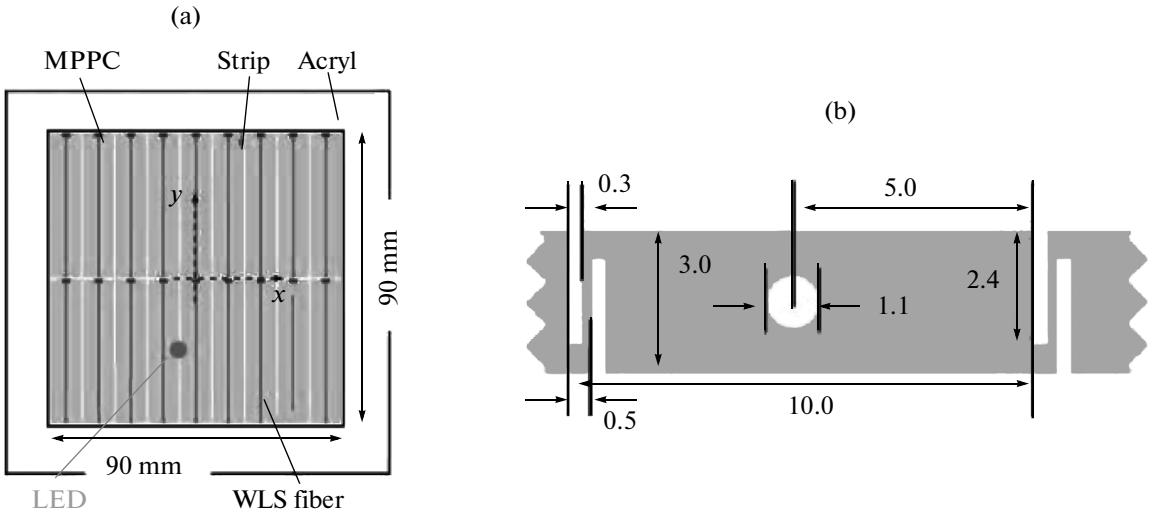

Fig. 56. (a) Structure of a scintillator layer of the CALICE electromagnetic calorimeter prototype; (b) cross section of a type-F strip (dimensions are in mm, the type-D is the same except that it has no holes).

A prototype of the CALICE ECAl is developed, which is a segmented sandwich calorimeter that consists of 26 layers of 3-mm Kuraray SCSN38 scintillator strips and a 3.5-mm absorber [88]. The scintillator layer consisted of two 45 × 90 mm^2 megastrips, each made up of nine 45 × 10 mm^2 strips (Fig. 56a), and the absorber consisted of 82% W, 13% Co, and 5% C, with a radiation length of 5.3 mm and a Molière radius of 22 mm.

The W absorber with this small R_M allows spatial discrimination of shower particles and identification of the particles using the PFA method. Strips in the neighboring layers were arranged orthogonally, thus providing high segmentation (10 × 10 mm^2) in measurement of (X, Y) coordinates. A film of white polyethylene terephthalate was used to reduce optical crosstalk between strips, megastrips, and layers. To increase the amount of light collected from the strips, their ends farthest from PMTs were covered with a mirror reflector film.

Two readout methods, type-F and type-D, were used (Fig. 56b). In type-F signals were transmitted to the PD through the 1-mm-diameter Kuraray Y11 WLS fiber held in place without the use of any glue, and in type-D signals were transmitted directly to the PD (strips had no holes and WLS fiber was not used). In both cases the PD was the 1 × 1 mm^2 Kuraray MPPC. A total of 468 MPPCs were used in the prototype. Tests of the prototype in positron beams with momentum of 1 to 6 GeV/c revealed their good energy

Table 10. Main characteristics of SiPMs from different manufacturers

Characteristics	MPPC Hamamatsu PhotonicsKK [90]	CPTA Photonics [80]	SiPM MEPhI/Pulsar [86]	SiPM MEPhI [81]	SiPM MEPhI EXELITES [82]	MAPD-3N Zecotec [58]
Active area, mm^2	1.3×1.3	1.28 (diameter)	1.1×1.1	3×3	3×3, 1×1	3×3
Pixel size, μm^2	50×50	43×43	32×32	30×30	100×100	
Number of pixels	667	796	1156	5625		$1.5 \times 10^4/mm^2$
Working voltage, V	68–71	~36	50	20–28	~37.5	~89
PDE, %	26–30 $\lambda = 550$ nm	~25 $\lambda = 525$ nm	<15 $\lambda = 550$ nm $T = 20°C$	23 $\lambda = 470$ nm $T = -50°C$	50–60 $\lambda \sim 400$ nm $T = 15°C$	~25 Green $T = 15°C$
Dark current, MHz	<1.35 (>0.5 Np.e.) $T = 25°C$	~2 T room	~1 T room	~20 T room	0.8 T room	$9 \times (0.1–1)$ $T = 25°C$
Gain	$\sim 10^6$	10^6	10^6	$(1–2) \times 10^6$	$\sim 2 \times 10^6$	$\sim 4 \times 10^4$

resolution: the stochastic term was between 13 and 14%, and the constant term between 3 and 4.5%, which well meets the requirements for shower energy reconstruction by the PFA method.

A large detector that used a great number (60000) of multipixel photon counters (MPPC, Hamamatsu) [89] was the NS280 detector [90] of the T2K neutrino spectrometer designed for investigating oscillations of muon neutrinos. The ND280 electromagnetic calorimeter used scintillator strips as an active material. They were produced by the extrusion technique at Fermilab from the same material and with the same cross section as the strips of the MINOS detector with a central hole in the strip for an optical fiber, and Kuraray Y11(200) 1-mm-thick WLS fibers were used to read out the strip signals.

Vacuum multianode PMTs and Hamamatsu silicon MPPCs were considered for the use in the ND280. The latter were chosen because they were insensitive to the magnetic field, more compact, stable, and economical (in mass production), while their photon detection efficiency (PDE) was higher than or identical to that of vacuum PMTs. With optical crosstalk, afterpulsing, and dark current contributions excluded, the measured PDE turned out to be 31% at a wavelength of 440 nm.

Table 10 presents the main characteristics of the MPPC S10362-11-050C, CPTA/Photonics and MEPhI SiPMs, and MAPD-3N.

A large experiment with as many as 3120 scintillator strips in Mu2e to be performed at Fermilab for investigating very rare processes of conversion of a μ meson to an electron in the presence of a nucleus [91]. In this experiment it is necessary to eliminate background events with very high reliability. One such event is cosmic μ mesons that can produce background electrons. It is planned to eliminate these events using scintillation veto counters covering large areas (about 500 m^2).

Scintillation counters made up of $1 \times 10 \times 460$ cm^3 strips will be used to assemble 3(4)-layer walls for the veto systems. These multilayer walls are needed to ensure the required 99.99% efficiency of the system. Light will be collected by three 1.4-mm-diameter WLS fibers inserted in the holes of the strips and transmitted to 16-pixel PDs; each PD pixel will read signals from all three WLS fibers of each strip. Now the Mu2e Collaboration, in which JINR participates, performs extensive investigations aimed at increasing light collection by selecting WLS fibers and the shape and size of strips and replacing vacuum PMTs with silicon PMTs.

The time resolution (TR) of SiPMs manufactured by Hamamatsu (MPPC S10262-11-25, S10262-11-50, S10262-11-100, 10-50S-BK-4S, 10-100-Fs), AdvanSiD FBK (ASD), and Sensl (SPM) as a function of the overvoltage ΔU, temperature T, wavelength, active area S, and pixel size was investigated in [92]. Out of five above-mentioned Hamamatsu SiPMs, the latter two were specially made with improved time characteristics as compared with standard Hamamatsu MPPCs. Pixels were square shaped with dimensions 25×25, 50×50, and 100×100 μm^2, and the active area of the PMTs was 1 and 9 mm^2.

Figure 57a shows the dependence of the full width at half-maximum Γ on the overvoltage ΔU. It is seen that the TR of all SiPMs improves with increasing ΔU. These data were obtained at $T = 20°C$ and $\lambda = 467$ nm for the SiPM with $S = 1$ mm^2. The upper ΔU values are limited by breakdowns and an appreciable increase in dark current. The best Γ was in the ASD (~120 ps). The Hamamatsu MPPC 10-50S-BK-4S and 10-100-F-Fs and the Sensl SPM showed approximately identical values of ~150 ps. The Hamamatsu SiPM shows

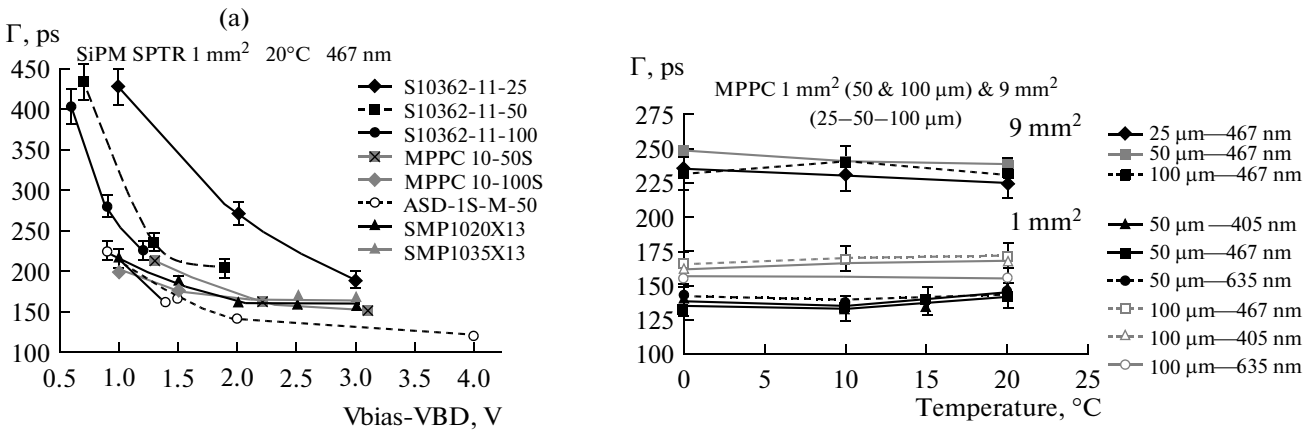

Fig. 57. (a) Dependence of Γ on overvoltage $\Delta U = V_{bias} - VBD$ measured at SiPMs of three manufacturers with different sizes of pixels (their linear dimensions are given in μm on the right in the lines with the SiPM name, except for the SPM with pixels of 20 and 35 μm); (b) dependence of Γ on the temperature T for the Hamamatsu SiPMs with $S = 1$ mm^2 and 9 mm^2 at wavelengths of 405, 476, and 635 nm and with pixels of 25, 50, and 100 μm.

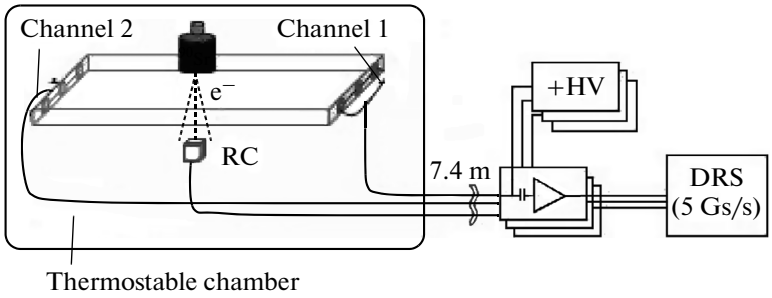

Fig. 58. Schematic view of a setup for measurements of the counter time resolution [94].

dependence of the TR on the size of pixels (three upper curves): Γ decreases with increasing pixel size. In the Sensl SiPM, Γ does not depend on the size of pixels.

The temperature dependence of Γ for the Hamamatsu SiPMs measured in the interval of 0 to 20°C turned out to be rather weak, but the TR tends to be noticeably dependent on the active area of the PD. For example, the PD with $S = 9$ mm^2 shows the TR about 50% worse than that of the PD with $S = 1$ mm^2 (Fig. 56b). In the other PDs the temperature dependence was not measured because their dark currents turned out to be too high.

Dependence of the TR on the wavelength and the size of the pixels requires further detailed investigations.

A very high single-photon TR σ (standard deviation) of 18 ps/$\sqrt{E}$ MeV$^{0.5}$ was obtained for small counters ($3 \times 3 \times 2$ cm^2) made of an ultrafast BC-422 scintillator and a SiPM like the Hamamatsu MPPC S10362-33-050 [93], which are efficient in the near ultraviolet region. In [93], the efficiency of the SiPMs in high magnetic fields up to 9.5 T was also noted.

Large-sized counters are often needed in HEP experiments. Counters made of ultrafast BC418, BC420, BC422, and BC422Q with dimensions of $60 \times 30 \times 5$ mm^3 and $120 \times 40 \times 5$ mm^3 were investigated in [94]. The main characteristics of these scintillators are presented in Appendix A. Hamamatsu, KETEK, AdvanSiD, and Sensl 3×3 mm^2 SiPMs with a high photon detection efficiency in the near ultraviolet region were used for readout. Three SiPMs placed in series were connected with optical grease to each end of the scintillator (Fig. 58). This connection increases the active area of the PDs and at the same time decreases their total capacitance, which considerably narrows the time spectrum in comparison with the results obtained with one SiPM or three SiPMs placed in parallel.

The time resolution of the counters was investigated using electrons from ^{90}Sr and a small reference counter RC ($5 \times 5 \times 5$ mm^3), which was located under the investigated counter and determined the irradiation region. The RC was made of the same material as the investigated counter, and signals were read out by the HPK S10362-33-050C.

Table 11. Large-sized SiPMs

Manufacturer	Designation	Area, mm^2	PDE, % at (λ_{max}, nm), $T = 25°C$	Dark current $\times 10^6$, Hz, $T = 25°C$	Gain $\times 10^6$
ZECOTEC	MAPD-3N	3 × 3	30 (480 nm)	9 × (0.1–1)	0.5
FBK-AdvanSiD	ASD-SiPM4S	4 × 4	30 (480 nm)	55–95	4.8
HAMAMATSU	S10985-50C	6 × 6	50* (440 nm)	6–10	0.75
KETEK	PM3350	3 × 3	40 (420 nm)	4	2
ST Microelectronics	SPM35A N	3.5 × 3.5	16 (420 nm)	7.5	3.2

* The Hamamatsu PDE involves optical crosstalk and afterpulsing contributions.

The best single-photon TR ($\sigma = 42 \pm 2$ ps per 1 MeV energy loss) was obtained for the scintillation counters made up of the BC-422 scintillator and a Hamamatsu SiPM (Fig. 59).

Thus, SiPMs with a similar time resolution can well be used in time-of-flight systems instead of microchannel plate PMTs with their time resolution of ~14 ps [95], the best among vacuum PMTs. However, these PMTs have low radiation hardness and limited service life and require very high working voltage (>2 kV). In addition, they are more sensitive to the magnetic field.

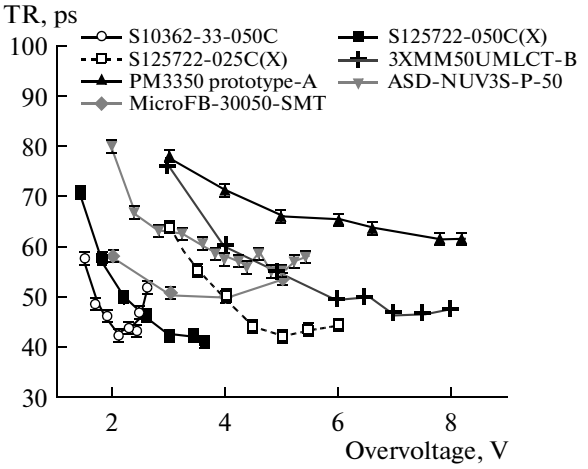

Fig. 59. TR of counters with different SiPMs as a function of the overvoltage. Designations beginning with S and 3X are for Hamamatsu, with PM for Ketek, with ASD for AdvanSiD, and with Micro for Sensl.

Now many research centers carry out extensive investigation into production and characteristics of silicon PMs with large active areas (Fig. 60) and those assembled into linear arrays and matrices of 4 × 4 (Hamamatsu, FBK, Sensl) and 8 × 8 (Zecotek). Table 11 presents characteristics of large-sized SiPMs from different manufacturers [96].

Scintillation counters with SiPM readout are planned to be used in many large detectors under construction, such as the MPD (multipurpose detector) for the heavy-ion collider NICA at JINR [59], Mu2e for investigations of conversion of μ mesons to electrons at FNAL [91], and PANDA at the accelerator for investigations of antiproton–ion interactions (FAIR) at GSI [97], and in currently operating detectors (CMS hadronic calorimeter).

CONCLUSIONS

The highly developed technology for production of plastic scintillators (injection molding, extrusion) allows scintillator tiles and strips of any shape to be produced in large amounts at a relatively low cost. Their optical characteristics (light yield, long-term stability, radiation hardness) meet the requirements on modern scintillators.

Fig. 60. Photos of large-sized SiPMs [96].

The importance of scintillation counters for modern HEP experiments can hardly be overestimated. They are widely used and will be used in calorimeters, triggers, tracking, and TOF and veto systems.

The prospects for the use of scintillators in future experiments are closely connected with a possibility for their high segmentation and the use of fibers for collection and transmission of signals to be read out by photodetectors with a multipixel structure similar to multianode vacuum and silicon PMs.

Compared with vacuum multianode PMTs, silicon photomultipliers have a similar gain and higher photon detection efficiency. They are compact and capable of operating in high magnetic fields. In addition, their cost will be lower during mass production.

Compactness of silicon photomultipliers allows them to be connected to the scintillator end for light collection either directly or through WLS fibers and also to be integrated into standard multichannel readout electronics.

Scintillation counters with *n*-type silicon PMs sensitive to near ultraviolet have a high time resolution (<20 ps) and can compete with vacuum PMTs and microchannel plate PMTs while having higher radiation hardness and long-term stability.

In the past years silicon photomultipliers have been rapidly developing, which permits hope for solving their current problems, namely, high dark currents and small size.

In conclusion, there are Appendices that present the main properties of some organic plastic scintillators (Appendix A) [98], optical and time characteristics of fibers manufactured by Kuraray [33] and Saint Gobain Crystals [34] (Appendix B), comparative characteristics of photodetectors widely used in high-energy physics experiments (Appendix C) [98], characteristics of scintillators used in the reviewed scintillation counters (Appendix D), and detectors and accelerators mentioned in this review (Appendix E).

APPENDICES

Appendix A. Properties of Some Organic Scintillators

The scintillation signal amplitude is given with respect to the anthracene signal; H/C is the ratio between the number of hydrogen atoms and the number of carbon atoms; NE stands for Nuclear Enterprises (UK) and BC stands for Bicron Corporation (United States); the wavelength is given at the emission spectrum maximum [98].

Scintillator	Density	*n*	Wavelength, nm	Decay time constant, ns	Scintillation signal amplitude	H/C	Light yield relative to NaI
Monocrystals							
naphthalene	1.15	1.58	348	11	11	0.800	
antracene	1.25	1.59	448	30–32	100	0.714	0.5
trans-aiilbene	1.16	1.58	384	3–8	46	0.857	
p-terphenyl	1.23		391	6–12	30	0.778	
Plastics[3)]							
NE 102 A	1.032	1.58	425	2.5	65	1.105	
NE 104	1.032	1.58	405	1.8	68	1.100	
NE 110	1.032	1.58	437	3.3	60	1.105	
NE 111	1.032	1.58	370	1.7	55	1.096	
Plastics[4)]							
BC-400	1.032	1.581	423	2.4	65	1.103	
BC-404	1.032	1.58	408	1.8	68	1.107	
BC-408	1.032	1.58	425	2.1	64	1.104	
BC-412	1.032	1.58	434	3.3	60	1.104	
BC-414	1.032	1.58	392	1.8	68	1.110	
BC-416	1032	1.58	434	4.0	50	1.110	
BC-418	1.032	1.58	391	1.4	67	1.100	
BC-420	1.032	1.58	391	1.5	64	1.100	
BC-422	1.032	1.58	370	1.6	55	1.102	
BC-422Q	1.032	1.58	370	0.7	11	1.102	
BC-428	1.032	1.58	480	12.5	50	1.103	
BC-430	1.032	1.58	580	16.8	45	1.108	
BC-434	1.049	1.58	425	2.2	60	0.995	

Appendix B. Optical, Time, and Mechanical Characteristics of Kuraray and Saint Gobain Crystals Fibers

Optical characteristics of Kuraray scintillating fibers[+] [33]

Fiber	Colour	Emission peak, nm	Decay time, ns	Attenuation length, m*	Characteristics
SCSF-81(81M)	Blue	437	2.4	>3.5	Long attenuation length
SCSF-78(78M)	Blue	450	2.8	>4.0	Long attenuation length and high light yield
SCSF-3HF(1500) -3HF(1500)M	Green	530	7	>4.5	Higher radiation hardness

[+] Measured using a bialkali PMT and ultraviolet light ($\lambda = 254$ nm).
* Fibers are non-S type, 1 mm in diameter.

Optical and time characteristics of Kuraray WLS fibers [33]

Fiber	Colour	Emission peak, nm	Attenuation length, m	Characteristics
Y-7(100) and Y-7(100)M	Green	490	>3.0	Green WLS fiber
Y-8(100) and Y-8(100)M	Green	511	>2.8	Green WLS fiber
Y-11(200) Y-11(200)M	Green	476	>3.5	Green WLS fiber
O-2(100) O-2(100)M	Orange	538	>1.5	Green to orange shifter
Clear-PS fiber			>10	Depends on wavelength

* Fibers are non-S type, 1 mm in diameter.
[+] Measured using a bialkali PMT and a LED (437 nm).

Optical and time characteristics of Saint Gobain Crystals WLS fibers [34]

Fiber	Colour	Emission peak, nm	Decay time, ns	L, m*	Number of photons per MeV**	Characteristics
BCF-10	Blue	432	2.7	2.2	~8000	General purpose[+]
BCF-12	Blue	435	3.2	2.7	~8000	For use in long lengths
BCF-20	Green	492	2.7	>3.5	~8000	Fast green scintillator
BCF-60	Green	530	7	3.5	~7100	3HF formulation for increased radiation hardness
BCF-91A	Green	494	12	>3.5	–	Blue to green shifter
BCF-92	Green	492	2.7	>3.5	–	Fast blue to green shifter
BSF-98						Clear light guide

* L is the attenuation length measured for a 1-mm-diameter fiber using a bialkali PMT.
** For minimum ionizing particles.
[+] Optimized for fibers with a diameter >250 μm.

Minimum bending diameters for Kuraray fibers of different type and diameter [33]

Fiber	Minimum bending diameter, mm		
Fiber diameter, mm	∅2.0	∅1.0	∅0.5
S	200	100	50
non-S	400	200	100

Appendix C [99]

PMT is a vacuum PD, MCP is a PD with microchannel holes, HPD is a hybrid photodiode, GPM is a gaseous PD, APD is an avalanche photodiode, PPD is an avalanche photodiode operating in a limited Geiger mode, VLPC is a visible light photon counter; ε_Q is the quantum efficiency, and ε_C is the collection efficiency.

Representative characteristics of some photodetectors commonly used in particle physics. The time resolution of the devices listed here varies in the 10–2000 ps range

Type	λ, nm	$\varepsilon_Q\varepsilon_C$	Gain	Rise time, ns	Area, mm^2	1-p.e. noise, Hz	*HV*, V	Cost, $
PMT*	115–1100	0.15–0.25	10^3–10^7	0.7–10	10^2–10^5	10–10^4	500–3000	100–5000
MCP*	100–650	0.01–0.10	10^3–10^7	0.15–0.3	10^2–10^4	0.1–200	500–3500	10–6000
HPD*	115–850	0.1–0.3	10^3–10^4	7	10^2–10^5	10–10^3	-2×10^4	~600
GPM*	115–500	0.15–0.3	10^3–10^6	$O(0.1)$	$O(10)$	10–10^3	300–2000	$O(10)$
APD	300–1700	~0.7	10–10^8	$O(1)$	10–10^3	1–10^3	400–1400	$O(100)$
PPD	400–550	0.15–0.3	10^5–10^6	~1	1–10	$O(10^6)$	30–60	$O(10)$
VLPC	500–600	~0.9	~5–10^4	~10	1	$O(10^4)$	~7	~1

* These devices often come in multianode configurations. In these cases, area, noise, and cost are to be considered on a "per readout channel" basis.

Appendix D. Characteristics of Scintillation Counters Mentioned in the Review

Detector	Scintillator	Strip (tile), mm	Light guide, ∅ = diameter, mm	PD (pixels, mm^2)	$N_{p.e.}$ (σ_t, ps)
MINOS [14]	PS + 1%PPO + 0.03%POPOP	10 × 41 × 8000	Kuraray non-S Y11(175), ∅1.2*	R5900-16 (16.4 × 4)	5.5
MINERvA [15]	PS + 1%PPO + 0.03%POPOP	17 × 33 × 3000	Kuraray Y11, S-35, ∅1.2	H8801MOD-2 (64.2 × 2)	5.2
OPERA[64]	PS + 2%PTP + 0.02%POPOP	10 × 26 × 6700	Kuraray non-S Y11(175)*	H7546 (2.3 × 2.3)	6
KLM Prototype [27]	PS + 2%PTP + 0.01%POPOP	7 × 40 × 2800	Kuraray Y11 ∅1.2*	G-APD	14
D0 (CPreSwD, FPreSwD) [36]	PS + 1%PTP + DFS(150)	17 × 33 × 2412 CPS 17 × 33 × (1040–2930) FPS	Kuraray Y11(250) ∅0.835	VLPC (128)	12–14
CDF-II(TOF) [42]	BICRON-408 (PVT)	40 × 40 × 2790	Plexiglas	H7761	(100)
CDF-II (μ-trigger.) [46]	PS + 2%PTP + 0.03%POPOP	20 × 300 × 3200	Kuraray S-type Y11(200) ∅1.0*	H5783	25
CDF(PreSw) [47]	PS + 1.5%PTP + 0.02%POPOP	(20 × 125 × 125)	Kuraray S-type Y11(200) ∅1.0	R5900-16	30
ATLAS (TileCal) [52]	PS + 1.5%PTP + 0.044%POPOP	(200–400) × (97 × 187)	Kuraray Y11(200)	R7877	1.2
AMS-02(TOF) [65]	PVT	10 × 120 × (~1300)	Plexiglas	R5946	(150)
LHCb (PreSw) [29]	PS + 2%PTP + 0.02%POPOP	(15 × (40 × 40, 60 × 60, 120 × 120))	Kuraray Y11(250) S-type, ∅1.0*	R5900 (64.2 × 2)	20–30
LHCb (ECAL) [29]	PS + 2%PTP+ 0.02%POPOP	(4 × (40 × 40, 60 × 60, 120 × 120))	Kuraray Y11(250) ∅1.2	R7899-20	3.1, 3.5, 2.6
ALICE ECAL [57]	BASF143E + 1.5%PTP + 0.04%POPOP	1.76 × 60 × 60	Kuraray Y11(200) ∅1.0	APD (5 × 5 mm^2) S 8664-55	4.3/MeV at $M = 30$
KOPIO [56]	BASF143E + 1.5%PTP + 0.04%POPOP	(1.5 × 109.7 × 109.7)	Kuraray Y11(200) ∅1.0	APD (200 mm^2) API 630-70-74-510	$N_\gamma \sim 60$ at APD input
T2K [89]	PS + 1%PPO + 0.03%POPOP	10 × 41 × 3000	Kuraray Y11(200) CS-35J, ∅1.0	MPPC (1.3 × 1.3 mm^2)	
CALICE ECAL [88]	SCSN38	10 × 45 × 90	Kuraray Y11 ∅1.0	MPPC (1 × 1 mm^2)	
ECAL0 COMPASS-II [58]	PS + 2%PTP + 0.05%POPOP	(1.5 × 39.95 × 39.95)	BASF-91A ∅1.2	MAPD-3N (3 × 3 mm^2)	

Fibers have double clad structure.

* Fibers have optical contact with strip.

Appendix E. Detectors and Accelerators Mentioned in the Review

CERN: European Organization for Nuclear Research.

LHC: Large Hadron Collider at CERN, cms energy of colliding PP beams 14 TeV, luminosity 10^{34} cm^2 s^{-1}, crossing rate 40 MHz.

ATLAS (A Toroidal Large ApparatuS) and CMS (Compact Muon Solenoid): multipurpose detectors at the LHC for the search for and investigation of Higgs bosons and supersymmetric and other particles.

ALFA: one of the ATLAS detectors for the high-precision measurement of the LHC luminosity using small-angle proton–proton scattering.

LHCb (Large Hadron Collider beauty): the single-arm spectrometer at the LHC for the investigation of CP asymmetry and rare B meson decays.

ALICE (A Large Ion Collider Experiment): the spectrometer at the LHC for the investigation of new states of matter, quark–gluon plasma, in heavy-ion interactions.

START detector of ALICE serves as a trigger of cosmic muons in its time-of-flight system.

ECAL is the shashlik-type electromagnetic calorimeter serving as a trigger of high-energy e/γ showers.

COMPASS (Common Muon and Proton Apparatus for Structure and Spectroscopy): the spectrometer at the SPS for the investigation of the nucleon structure and hadron spectroscopy in interactions of 160-GeV/c polarized muon and hadron beams with a polarized deuteron target.

ECAL0: a module of the highly segmented shashlik-type electromagnetic calorimeter for COMPASS-II.

OPERA: the neutrino detector for the investigation of oscillations of neutrinos produced at CERN. It is located in Gran Sasso (Italy) at a distance of 730 km from CERN.

FNAL: Fermi National Laboratory (Batavia, United States) with the Tevatron proton–antiproton collider, cms energy 1.96 TeV, luminosity $\sim 3 \times 10^{32}$ cm^{-2} s^{-1}.

D0 and CDF: two main spectrometers at the Tevatron for the investigation of heavy quark production and search for new particles and phenomena.

FPD: the forward proton detector of D0-II for the measurement of small-angle (about 1 mrad) proton and antiproton scattering.

MINOS (Main Injector Neutrino OScillation detector): the FNAL detector for the investigation of muon neutrino oscillations; it consists of two similar detectors located underground at a distance of 735 km from each other.

MINERvA: the detector for the investigation of neutrino–nucleus interactions.

Mu2e: an experiment at FNAL on the search for conversion of μ mesons to electrons.

KOPIO: a detector at the Brookhaven National Laboratory (United States) for the investigation of CP violations in very rare decays $K_L - \pi^0 \nu \nu$.

KLOE (K-Long Experiment): the detector for the investigation of CP violations in decays of K_L^0 mesons resulting from the decays $\varphi \to K_L K_S$.

KEKB (at the High Energy Accelerator Research Organization, Japan): an electron–positron collider, beam energies 8 and 3.5 GeV.

Belle-2: the spectrometer at the KEKB for the investigation of CP asymmetry in B meson decays.

KLM: a detector of the Belle-2 spectrometer for the detection of muons and K mesons.

T2K (Tokai to Kamioka, Japan): the underground detector for the investigation of ν oscillations; it consists of two detectors located at a distance of 295 km from each other.

AMS-02 (Alpha Magnetic Spectrometer): the spectrometer for the investigation of the composition and energy spectrum of cosmic particles and search for antimatter and dark matter in space.

ILC (International Linear Collider): the projected international linear electron–positron collider with the energy of colliding particles up to 2 TeV and luminosity up to 10^{34} cm^{-2} s^{-1}.

CALICE: projected hadronic and electromagnetic calorimeters at the ILC.

NICA (Nuclotron-based heavy Ion Collider fAcility): a heavy-ion collider under construction at JINR.

MPD: the multipurpose detector at NICA.

FAIR (Facility of Antiproton and Ion Research): a 30-GeV accelerator complex for the investigations with antiprotons and ions under construction at GSI (Darmstadt, Germany).

PANDA (antiProton ANnihilation at Darmstadt): the spectrometer at FAIR for the precision investigation of charmed quarks using beams of antiprotons with momenta of 1 to 15 GeV/c and luminosity of 2×10^{32} cm^{-2} s^{-1}.

ACKNOWLEDGMENTS

The author is grateful to Prof. Yu.N. Budagov, Dr. V.V. Glagolev, Dr. A.M. Artikov, and Dr. Yu.I. Davydov for the attention and support given to this work.

REFERENCES

1. J. B. Birks, *The Theory and Practice of Scintillation Counting* (Pergamon Press, London, 1964); R. C. Ruchti, "The use of scintillating fibers for charged-particle tracking," Ann. Rev. Nucl. Part. Sci. **46**, 281–319 (1996); G. F. Knoll, *Radiation Detection and Measurement* (New York, 1989).
2. Yu. K. Akimov, *Photon Methods of Radiation Detection* (Dubna, 2014) [in Russian].

3. Yu. N. Kharzheev, "Modern trends in methods of charged particle identification at high energies," Phys. Part. Nucl. **44** (1), 115–157 (2013).

4. T. O. White, "Scintillating fibers," Nucl. Instrum. Meth. A **273**, 820 (1988).

5. V. G. Senchishin et al., "Manufacture and study of new polysterene scintillators," Semicond. Phys., Quantum Electron. Optoelectron. **3** (2), 223–226 (2000); V. G. Senchishin, "Modern technologies for production of plastic scintillators," in *Cutting and Machining Tools in Technological Systems* (KhGPU, Kharkov, 2000), Vol. 57, pp. 205–816 [in Russian].

6. B. V. Grinev and V. G. Senchishin, *Plastic Scintillators* (Akta, Kharkov, 2003) [in Russian].

7. M. G. Kadykov, V. K. Semenov, and V. I. Suzdal'tsov, "Molded polystyrene plastic scintillator of the hadronic calorimeter of the "tagged neutrino facility", Prib. Tekh. Eksp. **6**, 95 (1992); Preprint OIYaI 13-90-16 (Joint Institute for Nuclear Research, Dubna, 1990).

8. S. P. Denisov, *Beams of Tagged Neutrinos: New Step in Neutrino Investigation Methodology* (MIFI, Moscow, 1987) [in Russian].

9. V. Semenov, *Proceedings of IX Conf. on Scintillators* (Kharkov, 1986), p. 86

10. IHEP, Protvino. http://www.ihep.ru/scint/bulk/product.htm; http://www.ihep.ru/scint/mold/product.htm.

11. P. Adamson (The MINOS Collab.), "The MINOS Detectors: Technical Design Report," NuMI-L-337 (1998).

12. A. Pla-Dalmau, A. D. Bross, and K. L. Mellott, "Low cost extruded plastic scintillator," Nucl. Instrum. Meth. A **405**, 422–431 (2001);

A. Pla-Dalmau, A. D. Bross, and V. V. Rykalin, "Extruding Plastic Scintillator at Fermilab," Fermilab-conf-03-318-E.

13. D. G. Michael et al. (The MINOS Collab.), "The magnetized steel and scintillator calorimeters of the MINOS experiment," Nucl. Instrum. Meth. A **596**, 190–228 (2008).

14. L. Aliaga et al. (The MINERvA Collab.), "Design, calibration and performance of the MINERvA detector," arXiv:13055199v1.

15. S. H. Chang, D. H. Kim, M. A. Khan, D. J. Kong, and J. S. Suh, "Production of extruded fine scintillator strips," J. Korean Phys. Soc. **53** (6), 3178–3181 (2008).

16. V. B. Grinev, S. V. Mel'nichuk, V. G. Senchishin, A. F. Adadurov, V. N. Lebedev, and N. P. Khlapova, "Extruded scintillator strips for the OPERA experiment," Vopr. At. Nauki Tekh., No. 4, 231–234 (2006).

17. R. Acquafredda et al. (The OPERA Collab.), "OPERA Proposal," CERN/SPSC **038**, 318 (2000).

18. N. Khlapova, Ya. Shpilevoy, V. Senchishyn, A. Gavrik, and V. Lebedev, "Light scattering in the plastic scintillator," Funct. Mater. **14** (2) (2007).

19. L. C. Renschler and L. A. Harrath, "Reduction of reabsorption effects in scintillators by employing solutes with large Stokes shifts," Nucl. Instrum. Meth. A **235**, 41–45 (1985).

20. Ph. Rebourgeard et al., "Fabrication and measurements of plastic scintillating fibers," Nucl. Instrum. Meth. A **427**, 543–567 (1999).

21. G. Kettenring, "Measurement of the reflectivities and absorption lengths at different wavelengths of plastic scintillator and acrylglass," Nucl. Instrum. Meth. A **131**, 451–456 (1975).

22. E. N. Bellamy, G. Bellettini, J. Budagov, F. Cervelli, I. Chirikov-Zorin, V. Kovtun, V. Senchishin, M. Incagh, D. Lucchesi, C. Pagliarone, O. Pukhovc, V. Seminozhenko, S. Tokar, N. Verezub, I. Zaljubovsky, and F. Zettia, "Test of long scintillation counters for large supercollider detectors," Nucl. Instrum. Meth. A **343**, 484–488 (1994).

E. N. Bellamy, G. Bellettini, J. Budagov, F. Cervelli, I. Chirikov-Zorin, M. Incagh, D. Lucchesi, C. Pagliarone, O. Pukhovc, V. Seminozhenko, S. Tokar, N. Verezub, I. Zaljubovsky, and F. Zettia "Calibration and monitoring of a spectrometric channel using a photomultiplier," Nucl. Instrum. Meth. A **339**, 468–476 (1994).

23. A. Artikov, J. Budagov, I. Chirikov-Zorin, D. Chokheli, M. Lyablin, G. Bellettini, A. Menzione, S. Tokar, N. Giokaris, and A. Manousakis-Katsikakis, "Properties of the Ukraine polystyrene-based plastic scintillator UPS 923A," Nucl. Instrum. Meth. A **555**, 125–131 (2005).

24. V. G. Senchishin, V. N. Lebedev, N. P. Khlapova, and A. F. Adadurov, "New radiation-hard plastic scintillator UPS–98H for hadronic calorimeters," Vopr. At. Nauki Tekh., No. 3, 160–163 (2005).

25. S. Aota, T. Asakawa, K. Hara, et al., "A scintillating tile/fiber system for the CDF plug upgrade EM calorimeter," Nucl. Instrum. Meth. A **352**, 557–568 (1995).

26. S. V. Melnichuk, "Dependence of light yield of scintillation strips on the reflective coating material kind," Funct. Mater. **11** (4) (2004).

27. E. Tarkovsky, "Performance of a scintillating strip detector with G-APD readout," Nucl. Instrum. Meth. A **628**, 372–375 (2011). Yu. V. Musienko, E. V. Akhromeev, A. Yu. Afanas'ev, G. B. Bondarenko, V. M. Golovin, E. N. Gushchin, N. V. Ershov, A. O. Izmailov, Yu. G. Kudenko, B. K. Lubsandorzhiev, V. A. Mayatskii, M. M. Khabibullin, A. N. Khotyantsev, and A. T. Shaikhiev, "Higly sensitive micropixel avalanche photodiodes for scintillation counters of near T2K experiment, " www.itep.ru.

28. A. Artikov, Yu. A. Budagov, V. B. Grinev, et al., "Scintillator plates of a new detector: development, production, and quality control", Preprint OIYaI R13-2005-27 (Joint Institute for Nuclear Research, Dubna, 2005).

29. A. Schopper, "Overview of the LHCb calorimeter system," Nucl. Instrum. Meth. A **623**, 219–221 (2010).

30. A. Artikov, J. Budagov, I. Chirikov-Zorin, et al., "New-generation large-area muon scintillation counters with wavelength shifter readout for CDF II," Phys. Part. Nucl. Lett. **3** (3), P. 188–200 (2006).

31. Ju. Budagov, I. Chirikov-Zorin, M. Incagli, et al., Preprint OIYaI E13–2000–127 (Joint Institute for Nuclear Research, Dubna, 2000).
32. V. I. Kolomoets, L. K. Lytkin, S. I. Merzlyakov, O. V. Mineev, Yu. N. Kharzheev, and G. A. Chlachidze, "Investigation of the time characteristics of the thin large sized scintillation counter", Preprint OIYaI 13-88-216 (Joint Institute for Nuclear Research, Dubna, 1988) [in Russian].
33. Plastic Scintillating Fibers. http://kuraraypsf.jp.
34. Organic Scintillation Materials. http://www.crystals.saint-gobain.com.
35. B. M. Abazov et al. (D0 Collab.), "Upgraded D0 detector," Nucl. Instrum. Meth. A **565**, 463–532 (2006).
36. B. M. Abazov et al. (D0 Collab.), "The muon system of the Run II D0 detector," Nucl. Instrum. Meth. A **552**, 372–398 (2005).
37. M. D. Petroff and M. Atic, IEEE Trans. Nucl. Sci. NS-36, 158–163 (1986).
38. V. Abramov (D0 Collab.), "Technical Design Report for D0 forward trigger scintillation counters," D0 Note 3237 (1997).
39. V. Bezzubov, D. Denisov, S. Denisov, H. T. Diehl, A. Dyshkant, V. Evdokimov, A. Galyaev, P. Goncharov, S. Gurzhiev, A. S. Ito, K. Johns, A. Kostritsky, A. Kozelov, and D. Stoianova, FERMILAB-Conf-98/020.
40. MELZ, Electrozavodskaya str., 23, Moscow, Russia, 105023.
41. S. Belikov et al., Instrum. Exp. Tech. **36**, 390 (1993).
42. S. J. Cabrera et al. (CDF-II Collab.), "CDF-II Time-of-flight detector," Nucl. Instrum. Meth. A **494**, 416–423 (2002).
43. S. V. Afanas'ev, L. Ya. Zhil'tsova, V. I. Kolesnikov, A. I. Malakhov, G. L. Melkumov, and A. Yu. Semenov, "Scintillation detectors for precise time measurements," Kratk. Soobshch. OIYaI, No. 1[81]-97 (Joint Institute for Nuclear Research, Dubna, 1981).
44. NA-49 Collab., CERN SPSLC91-31 SPSLC/P264 (1991).
45. Yu. S. Anisimov et al. Kratk. Soobshch. OIYaI, No. 5[91]-98 (Joint Institute for Nuclear Research, Dubna, 1991) [in Russian].
46. A. Artikov et al. (CDF-II Collab.), "Design and construction of new central and forward muon counters for CDF-II," Nucl. Instrum. Meth. A **538**, 358–371 (2005).
47. A. Artikov, O. E. Pukhov, G. A. Chlachidze, and D. Chokheli, "Scintillation counters of the muon system at CDF-II," Phys. Part. Nucl. **39** (3), 410–423 (2008).
48. M. Callinara and A. Artikov, "A new scintillator tile/fiber preshower detector for the CDF central calorimeter," IEEE Trans. Nucl. Sci. **52**, 879–883 (2005).
49. S. Amsler et al. (Particle Data Group), Phys. Lett. B **667**, 1 (2008).
50. R. Wigmans, "Calorimetry," Scientifica Acta **2** (1), 18–55 (2008).
51. N. Akchurin and R. Wigmans, "Hadron calorimeters," Nucl. Instrum. Meth. A **666**, 80–97 (2012).
52. ATLAS Collab., "The ATLAS experiment at the CERN Large Hadron Collider," J. Instrum. **3**, P. S08003 (2008); Eur. Phys. J. C **70**, 1193–1236 (2010).
53. S. Ask et al. (ATLAS Collab.), "Luminosity measurement at ATLAS – development, construction and test of scintillating fiber prototype detectors," Nucl. Instrum. Meth. A **568**, 588–600 (2006).
54. CMS Collab., "The CMS experiment at the CERN Large Hadron Collider," J. Instrum. **3**, S08004 (2008).
55. LHCb Collab., "The Large Hadron Collider beauty experiment at the CERN Large Hadron Collider," J. Instrum. **3**, S08005 (2008); R. I. Dzhelyadin, "The LHCb hadron calorimeter," Nucl. Instrum. Meth. A **494**, 332–339 (2002).
56. G. S. Atoian, G. I. Britvich, S. K. Chernichenko, S. Dhawanc, V. V. Issakova, O. V. Karavicheva, T. L. Karavicheva, V. N. Marin, A. A. Poblaguev, I. V. Shein, A. P. Soldatov, and M. E. Zeller, "An improved shashlik calorimeter," Nucl. Instrum. Meth. A **584**, 291–303 (2008).
57. J. Allen et al. (ALICE ECAL Collab.), "Performance of prototype for ALICE electromagnetic calorimeter," Nucl. Instrum. Meth. A **615**, 6–13 (2010).
58. I. E. Chirikov-Zorin, Z. Krumstein, A. Olshevsky, V. Utkin, and P. Zhmurin, Preprint OIYaI E13–2013–82 (Joint Institute for Nuclear Research, Dubna, 2013); N. Anfimov, I. Chirikov-Zorin, A. Dovlatov, O. Gavrishchuk, A. Guskov, N. Khovanskiy, Z. Krumshtein, R. Leitner, G. Meshcheryakov, A. Nagaytsev, A. Olchevski, T. Rezinko, A. Sadovskiy, Z. Sadygov, I. Savin, V. Tchalyshev, I. Tyapkin, G. Yarygin, and F. Zerrouk, Beam test of Shashlik EM calorimeter prototypes readout by Novel MAPD with superhigh linearity," Nucl. Instrum. Meth. A **617**, 78–80 (2010): N. Anfimov, V. Anosov, I. Chirikov-Zorin, D. Fedoseev, O. Gavrishyk, N. Khovanskiy, Z. Krumshtein, R. Leitner, G. Meshcheryakov, A. Nagaitsev, A. Olshevski, T. Rezinko, A. Selyunin, A. Rybnikov, Z. Sadygov, I. Savin, V. Tchalyshev, P. Zhmurin, "Shashlik EM calorimeter prototype readout by MAPD with superhigh pixel density for COMPASS II," Nucl. Instrum. Meth. A **718**, 75–77 (2013).
59. Kh. U. Abraamyan et al. (NICA Collab.), "MPD detector at the NICA heavy-ion collider at JINR," Nucl. Instrum. Meth. A **628**, 99–102 (2011).
60. P. Sonderegger, "Fibre calorimeters: dense, fast, radiation," Nucl. Instrum. Meth. A **257**, 523–527 (1987); D. W. Hertzog, P. T. Debevec, R. A. Eisenstein, M. A. Graham, S. A. Hughes, P. E. Reimer, and R. L. Tayloe, "A high-resolution lead /scintillating fiber electromagnetic calorimeter" Nucl. Instrum. Meth. A **294**, 446–458 (1990); S. A. Sedykh, et al. (BNL (g-2) Collab.), "Electromagnetic calorimeters for the BNL muon (g-2) experiment," Nucl. Instrum. Meth. A **455**, 346 (2000).
61. J. Budagov, I. Chirikov-Zorin, V. Glagolev, A. Jordanov, Yu. Kharzheev, et al. "Energy resolution of a lead scin-

tillating fiber electromagnetic calorimeter," Nucl. Instrum. Meth. A **343**, 476–483 (1994).

62. M. Adinolfi et al. (KLOE Collab.), "The KLOE electromagnetic calorimeter," Nucl. Instrum. Meth. A **482**, 364 (2002).
63. R. McNabb et al., "A tungsten/scintillating fiber electromagnetic calorimeter prototype for a high-rate muon (g-2) experiment," Nucl. Instrum. Methods **602**, 396–402 (2009).
64. A. Lucottea, S. Bondila, K. Borer, et al., "A front-end read out chip for the OPERA scintillator tracker," Nucl. Instrum. Meth. A **521**, 378–392 (2004).
65. D. Casadei et al. (AMS-02 Collab.), "The AMS-02 time of flight system," Nucl. Phys. B. (Proc. Suppl.) **113**, 133–138 (2002); V. Bindi, A. Contin, N. Masi, A. Oliva, F. Palmonari, L. Quadrani, and A. Tiseni, "The time of flight detector of the AMS-02 experiment on the International Space Station," Nucl. Instrum. Meth. A **718**, 478–480 (2013).
66. C. Aldloff et al. (AMS-02 Collab.), "The AMS-02 lead-scintillating fibers electromagnetic calorimeter," Nucl. Instrum. Meth. A **714**, 147–154 (2013).
67. R. A. Montgomery, E. N. Cowie, M. Hoek, T. Keri, and B. Seitz, "Multianode photomultiplier tube studies for imaging applications," Nucl. Instrum. Meth. A **695**, 326–329 (2012).
68. K. K. Hamamatsu, Photonics. http://www.hamamatsu.com/index.html.
69. N. A. Bajanov, Yu. S. Blinnikov, Yu. I. Gusev, et al., "Fine-mesh photodetectors for CMS endcap electromagnetic calorimeter," Nucl. Instrum. Meth. A **442**, 146–149 (2000).
70. B. Adeva et al. (L3 Collab.), "The construction of the L3 experiment," Nucl. Instrum. Meth. A **289**, 35 (1990).
71. Shiizuka Susumu, Adachi Ichiro, Dolenec Rok, et al. "Study of 144-channel hybrid avalanche photo detector for Belle II RICH counter," Nucl. Instrum. Meth. A. **628**, 315–318 (2011).
72. P. Cushman, A. Heering, and A. Ronzhin, "Custom HPD readout for the CMS HCAL," Nucl. Instrum. Meth. A **442**, 289 (2000).
73. D. Renker, "Properties of avalanche photodiodes for applications in high energy physics, astrophysics and medical imaging," Nucl. Instrum. Meth. A **486**, 164–169 (2002); K. Deiters, Q. Ingram, Y. Musienko, et al., "Properties of the avalanche photodiodes for the CMS electromagnetic calorimeter," Nucl. Instrum. Meth. A **453**, 223 (2000).
74. V. Golovin, M. Tarasov, and G. Bondarenko, Patent No. RU 2142175 (1998).
75. Z. Sadygov, Patent No. RU 2102820 (1998).
76. P. Buzhan, B. Dolgoshein, L. Filatov, A. Ilyin, V. Kantzerov, V. Kaplin, A. Karakash, F. Kayumov, S. Klemin, E. Popova, and S. Smirnov, "Silicon photomultiplier and its possible applications," Nucl. Instrum. Meth. A **504**, 48–52 (2003).
77. A. Bross, E. Flattum, D. Lincoln, S. Grunendahl, J. Warchol, M. Wayne, and P. Padley, "Characterization and performance of visible light photon counters (VLPCs) for the upgraded D0 detector at the Fermilab Tevatron," Nucl. Instrum. Meth. A **477**, 172 (2002).
78. E. Albrecht, M. Alemi, G. Barber, J. Bibby, M. Campbell, A. Duane, T. Gys, J. Montenegro, D. Piedigrossi, R. Schomaker, W. Snoeys, S. Wotton, and K. Wyllie, "Performance of hybrid photon detector prototypes with 80% active area for the RICH counters of LHCb," Nucl. Instrum. Meth. A **442**, 164 (2000).
79. B. Dolgoshein et al. (Calice/SiPM Collab.), "Status report on silicon photomultiplier development and its applications," Nucl. Instrum. Meth. A **563**, 368–378 (2006).
80. Y. Musienko, "Advances in multipixel geiger-mode avalanche photodiodes (silicon photomultiples)," Nucl. Instrum. Meth. A **598**, 213–216 (2009).
81. P. Bushan, B. Dolgoshein, L. Filatov, A. Ilyin, V. Kaplin, A. Karakash, S. Klemin, R. Mirzoyan, A. N. Otte, E. Popova, V. Sosnovtsev, and M. Teshima, "Large area silicon photomultipliers: performance and applications," Nucl. Instrum. Meth. A **567**, 78–82 (2006).
82. B. Dolgoshein, R. Mirzoyan, E. Popova, P. Buzhan, A. Ilyin, V. Kaplin, A. Stifutkin, M. Teshima, and A. Zhukov, "Large area UV SiPM with extremely low crosstalk," Nucl. Instrum. Meth. A **695**, 40–43 (2012).
83. A. Akindinov, G. Bondarenko, V. Golovin, E. Grigoriev, Yu. Grishuk, D. Mal'kevich, A. Martemiyanov, M. Ryabinin, A. Smirnitskiy, K. and K. Voloshin, "Scintillator counter with MRS APD light readout," Nucl. Instrum. Meth. A **539**, 172–176 (2005).
84. Z. Sadygov, A. Olshevski, I. Chirikov, I. Zheleznykh, and A. Novikov, "Three advanced designs of micropixel avalanche photodiodes: their present status, maximum possibilities and limitations," Nucl. Instrum. Meth. A **567**, 70–73 (2006); Z. Sadygov, A. Ol'shevskii, N. Anfimov, T. Bokova, A. Dovlatov, V. Zhezher, Z. Krumshtein, R. Mekhtieva, R. Mukhtarov, M. Troitskaya, V. Chalyshev, I. Chirikov-Zorin, and V. Shukurova, "Microchannel avalanche photodiode with a wide linearity range," Pis'ma Zh. Tekh. Fiz. **36** (1), 83–89 (2010).
85. D. Renker and E. Lorentz, "Advances in solid state photon detectors," J. Instrum. **4**, 04004 (2009).
86. M. Danilov (CALICE Collab.), "Scintillator tile hadron calorimeter with novel SiPM readout," Nucl. Instrum. Meth. A **581**, 451 (2007).
87. E. Garutti, "Silicon photomultipliers for high energy physics detectors," arXiv:1108.3166v2.
88. K. Francis, "Performance of the first prototype of the CALICE scintillator strip electromagnetic calorimeter," Nucl. Instrum. Meth. A **763**, 278 (2014).
89. M. Yokoyama, T. Nakaya, S. Gomi, et al., "Application of Hamamatsu MPPCs to T2K neutrino detectors," Nucl. Instrum. Meth. A **610**, 128–130 (2009).
90. D. Allan et al. (T2K ND280 Collab.), "The electromagnetic calorimeter for the T2K near detector ND280," arXive:1308.3445v2.
91. R. M. Carey et al. (Mu2e Collab.), Fermilab Proposal 0973 (2008); Craig Group and Yuri Okgruzian (Mu2e Collab.), "Design consideration for the cosmic-ray-

veto system of the Mu2e experiment at Fermilab," arXiv:1377v1.

92. V. Puill, C. Bazin, D. Breton, L. Burmistrov, V. Chaumat, N. Dinu, J. Maalmi, J. F. Vagnucci, and A. Stocchi, "Single photoelectron timing resolution of SiPM as a function of the bias voltage, the wavelength and the temperature," Nucl. Instrum. Meth. A **685**, 354–358 (2012).
93. A. Stoykov, R. Scheuermann, and K. Sedlak, "A time resolution study with a plastic scintillator read out by a Geiger-mode avalanche photodiode," Nucl. Instrum. Meth. A **695**, 202–205 (2012).
94. P. W. Cattaneo, M. De Gerone, F. Gatti, M. Nishimura, W. Ootani, M. Rossella, and Y. Uchiyama, "Development of high precision timing counter based on plastic scintillator with SiPM readout," arXiv:1402.1404v2.
95. J. Va'vra, D. W. G. S. Leith, B. Ratcliff, E. Ramberg, M. Albrow, A. Ronzhin, C. Ertley, T. Natoli, E. May, and K. Byrum, Nucl. Instrum. Meth. A **606**, 404 (2009).
96. V. Puill, *Proceedings of the IEEEN55 Conference, Anaheim, 2012.*
97. B. Lewandowski, "Fast and compact ECAL for the PANDA detector at GSI," Nucl. Instrum. Meth. A **537**, 349 (2005).
98. J. Beringer et al. (Particle Data Group), Phys. Rev. D **86**, 010001 (2012).
99. D. Chakraborty and T. Sumiyoshi, "Review of Particle Physics. 31.2. Photon detectors;" Phys. Rev. D **86**, 010001 (2012).

Translated by M. Potapov